Universitätsklinikum Hamburg Eppendorf

Zentrum für Experimentelle Medizin,
Institut für Experimentelle Herz-Kreislaufforschung

Prof. Dr. rer. nat. Viacheslav Nikolaev

Dominant Negative Gα_s mutant to block detrimental β-AR induced pathological hypertrophy in the heart

Dissertation

zur Erlangung des Grades eines Doktors der Medizin
an der Medizinischen Fakultät der Universität Hamburg.

vorgelegt von:

Robert Peter Wiegmann
aus Stuttgart

Hamburg 2021

Angenommen von der
Medizinischen Fakultät der Universität Hamburg am: 22.10.2021

Veröffentlicht mit Genehmigung der
Medizinischen Fakultät der Universität Hamburg.

Prüfungsausschuss, die Vorsitzende: Prof. Dr. rer. nat. Friederike Cuello

Prüfungsausschuss, zweiter Gutachter: Prof. Dr. rer. nat. Viacheslav Nikolaev

Kurzfassung

Die Herzinsuffizienz (HI) ist eine der führenden kardiovaskulären Todesursachen in westlichen Nationen. Für ihre Entstehung stellt die Herzhypertrophie einen maßgeblichen Risikofaktor dar. Eine Verhinderung der Entstehung oder sogar Regress der Herzhypertrophie wirkt sich positiv auf die Morbidität und Mortalität aus. Zur Entstehung von sowohl der kardialen Hypertrophie als auch HI tragen wesentlich neuroendokrine Systeme bei. Eine Reduktion der Pumpfunktion aufgrund von ventrikulärer Beeinträchtigung führt zu einer kompensatorischen Aktivierung neuroendokriner Systeme. Die Stimulation des sympathischen Nervensystems führt über die Aktivierung des heterotrimeren Gα_s gekoppelten β-Adrenorezeptors (β-AR) zu einer Zunahme der Pumpfunktion des Herzens. Allerdings wirkt sich eine chronische Stimulation dieses Signalweges direkt toxisch auf den Herzmuskel aus. Sie bewirkt unter anderem pathologisches hypertrophes Wachstum von Herzmuskelzellen und ventrikuläres Remodeling. β-Blocker schützen das Herz vor Überstimulation, zeigen jedoch nicht-kardiale Nebenwirkungen. Eine vollständige kardiomyozyten-spezifische Blockade des β-AR-Signalwegs könnte sich in der HI-Therapie als vorteilhaft erweisen.

Das Ziel dieser Arbeit ist es, ein dominant negatives Gα_s-Protein (DNG), das spezifisch in Kardiomyozyten exprimiert wird, auf die Hemmung der β-AR-Signalkaskade zu untersuchen. Daneben soll weiterhin die Hemmung des hypertrophen Wachstums, induziert durch chronische β-AR-Stimulation, analysiert werden. Hierzu wurde DNG mittels adenoviralen Gentransfers in isolierten adulten ventrikulären Kardiomyozyten der Ratte (ARVCM) exprimiert, um die Funktionalität von DNG zu untersuchen. Die Co-Expression des cAMP-FRET-Biosensors Epac1-camps ermöglichte cAMP-Messungen in vitalen ARVCM. Hier konnte eine Hemmung der β-AR-Agonisten-induzierten cAMP-Antwort gezeigt werden. Dies wurde durch eine reduzierte Phosphorylierung des Phospholamban untermauert. Weiterhin konnte ein abgeschwächtes hypertrophes Wachstum als Reaktion auf eine chronische β-AR-Stimulation durch halb-automatisierte Messungen der ARVCM Zellmorphologie nachgewiesen werden. *In vivo* wurde die Kardiomyozyten-spezifische Expression von DNG durch Troponin T gerichteten Gentransfer mittels Adeno-assoziierter Viren (AAV) erzielt. Echokardiographische Untersuchungen von AAV-DNG injizierten Mäusen zeigten eine normale Herzfunktion. Die kardiale Hypertrophie wurde durch chronische β-AR-Stimulation mit im-

plantierten osmotischen Minipumpen induziert. Hier zeigten AAV-DNG-injizierte Mäuse in der Echokardiographie eine reduzierte Hypertrophie und eine abgeschwächte Expression von pathologischen Hypertrophie-assoziierten *fetal*- und pro-fibrotischen Genen. Signifikante Unterschiede in der Hypertrophie des gesamten Herzens und der Kardiomyozyten-Querschnittsfläche in Gewebeschnitten wurden jedoch nicht beobachtet. Es zeigt sich eine partiell protektive Wirkung durch DNG auf die Hemmung der β-AR-Signalkaskade.

Abstract

Heart failure (HF) is a major contributor to mortality and health care expenses in developed countries for which cardiac hypertrophy is an important risk factor. Neuroendocrine systems are critically involved in the development of cardiac hypertrophy and subsequent heart failure. Adrenergic stress, a compensatory response to decreased cardiac function, has a positive short-term effect on cardiac output via activation of the Gα_s coupled β-adrenoreceptor (β-AR) pathway. However, chronic stimulation of this pathway causes pathological hypertrophy and ventricular remodeling and thereby contributes to the worsening of HF. β-blockers protect the heart from overstimulation but have non-cardiac side effects. Furthermore, a complete cardiomyocyte specific blockage of β-AR signalling might be beneficial in the treatment of HF.

The aim of this thesis is to investigate a dominant negative Gα_s protein (DNG) specifically expressed in cardiomyocytes for inhibition of the β-AR signaling cascade and subsequent inhibition of hypertrophic growth to chronic β-AR stimulation. To this end, an adenoviral gene transfer of DNG in isolated adult rat ventricular cardiomyocytes (ARVCM) was pursued to investigate the functionality of DNG. Co-expression of cAMP-FRET biosensor Epac1-camps enabled live cAMP measurements and revealed inhibition of β-AR agonist induced cAMP response. This was substantiated by inhibited phosphorylation of β-AR downstream target phospholamban. Furthermore, attenuated hypertrophic growth in response to chronic β-AR stimulation was shown by semi-automated cell morphology measurements. An *in vivo* cardiomyocyte-specific expression of DNG was achieved by troponin T directed gene transfer using adeno-associated viruses (AAV). Echocardiographic examination of AAV-DNG injected mice revealed normal heart function. Cardiac hypertrophy was induced by chronic β-AR stimulation with implanted osmotic minipumps. AAV-DNG-injected mice exhibited reduced hypertrophy on echocardiography and attenuated expression of pathological hypertrophy-associated *fetal* and pro-fibrotic genes. However, significant differences in hypertrophy of the whole heart and of cardiomyocyte cross-sectional area in tissue sections were not observed. A partial protective effect of DNG on the inhibition of the β-AR signaling cascade is evident.

Contents

List of Abbreviations

a.u.	arbitrary units
AAV	adeno associated virus
AC	adenylyl cyclase
ANP	natriuretic peptide A
AR	adrenergic receptor
ARVCM	adult rat ventricular cardiomyocyte
ATP	adenosine triphosphate
BNP	natriuretic peptide B
CaMKII	Ca^{2+}/calmodulin-dependent protein kinase II
cAMP	cyclic adenosine monophosphate
cGMP	cyclic guanosine monophosphate
CMV	cytomegalovirus
Col1a1	collagen type I alpha 1 chain
Col3a1	collagen type III alpha 1 chain
CSQ	calsequestrin
ct	cycle threshold
DNA	deoxyribonucleic acid
DNG	dominant negative $G\alpha_s$ protein
EF	ejection fraction
EPAC	exchange protein directly activated by cAMP
Fhl1	four and a half LIM domain protein 1
Fhl2	four and a half LIM domain protein 2
FS	fractional shortening

G-protein heterotrimeric guanine- nucleotide-binding regulatory protein

GAPDH glyceraldehyde 3-phosphate dehydrogenase

GDP guanosine diphosphate

GPCR G-protein-coupled receptor

GRK G-protein-coupled receptor kinase

GTP guanosine triphosphate

HF heart failure

HFmrEF heart failure with mid range ejection fraction

HFpEF heart failure with preserved ejection fraction

HFrEF heart failure with reduced ejection fraction

I-1 phosphatase-1 inhibitor-1

IBMX 3-isobutyl-1-methylxanthine

IHC immunohistochemistry

ISO isoproterenol

IVSd interventricular septum in diastole

IVSs interventricular septum in systole

LTCC L-type calcium channel

LV left ventricular

LVEF left ventricular ejection fraction

LVIDd left ventricular internal diameter in diastole

LVIDs left ventricular internal diameter in systole

LVPWd left ventricular posterior wall in diastole

LVPWs left ventricular posterior wall in systole

MAPK mitogen-activated protein kinase

MOI multiplicity of infection

Myh6 α-myosin heavy chain

Myh7 β-myosin heavy chain

NYHA New York Heart Association

PCR polymerase chain Reaction

PDE phosphodiesterase

PKA protein kinase A

PKG protein kinase G

PLN phospholamban

PNS parasympathetic nervous system

PP-1 phosphatase type 1

PPI-1 protein phosphatase inhibitor-1

PSR picrosirius red

RAAS renin-angiotensin-aldosterone-system

RNA ribonucleic acid

RNase ribonuclease

rt-qPCR real-time quantitative PCR

scAAV self-complementary AAV

SEM standard error of the mean

SNS sympathetic nervous system

ssAAV single-stranded AAV

TnT troponin T

vg vector genomes

WGA wheat germ agglutinin

1 Introduction

Heart failure (HF) is a leading cause of death in western nations and of increasing significance in an aging population. It contributes to significant morbidity and health care expenditures. Although major accomplishments have been achieved in the treatment of HF, life expectancy and quality of life is severely reduced (Roger, 2013; Ambrosy et al., 2014). Left ventricular (LV) hypertrophy is a major risk factor for heart failure development and other cardiovascular complications. The prevention or regression of LV hypertrophy reduces cardiac morbidity and mortality (Levy, 1991; Mathew et al., 2001; Larstorp et al., 2012).

In the context of cardiac disease an initial *index event*, which impairs cardiac function, triggers the activation of neurohormonal systems to maintain adequate cardiac output. Here, the sympathetic nervous system (SNS) plays a pivotal role in HF pathogenesis: Short term SNS activity improves cardiac function by increased β-adrenergic receptor (AR)- heterotrimeric G-protein signaling which augments inotropy and chronotropy. However, chronic stimulation of the β-AR system exerts a direct toxic effect and induces cardiomyocyte hypertrophy, apoptosis and myocardial fibrosis (Hartupee and Mann, 2016; Engelhardt, Hein, et al., 1999). In HF patients the β-AR system is downregulated and uncoupled from downstream signaling while other cardiac disease related proteins are upregulated (Lohse et al., 2003; Agüero et al., 2012; Neumann, Schmitz, et al., 1988). Although pharmaceutical β-AR blockage improves cardiac function and restores β-AR signaling (Triposkiadis et al., 2009), complete cardiac specific blockage of the β-AR system might be beneficial in a context dependent use. This would cause an anticipated elimination of positive inotropic reserve but carries the potential to block detrimental chronic β-AR signaling and stabilize cardiac function at a sustainable level.

The research objective of this thesis is to explore a mutated heterotrimeric G-protein α subunit (dominant negative Gα_s protein (DNG) created by Berlot (2002)) which inhibits Gα_s signaling to block β-AR specifically in cardiomyocytes *in vitro* and *in vivo*. For the latter, adeno associated virus (AAV) mediated gene transfer was aspired to achieve cardiomyocyte specific DNG expression in the murine heart. DNG expressing mice were analyzed for baseline cardiac function and subsequently the inhibitory properties of DNG challenged in a model of chronic β-AR stimulation induced cardiac hypertrophy.

1.1 Heart failure

This section provides an outline of heart failure including the definition, classification, epidemiology, aetiology and pathophysiology. Furthermore, the concept and clinical relevance of pathological hypertrophy and remodeling are described. The significance of the SNS in the pathogenesis of HF is highlighted by an outline of basic SNS physiology in controlling cardiac function including the involved signaling cascade in cardiomyocytes. This is followed by an insight into the pathological aspects of sustained β-AR stimulation in the context of cardiac disease including the involved subcellular signalling cascades that drive hypertrophic signalling. Finally, the DNG construct is introduced and functional mutations that inhibit $G\alpha_s$ signaling presented.

1.1.1 Definition and classification

HF is a complex clinical syndrome with an underlying malfunctioning heart not able to pump sufficiently to meet the metabolic demands of the body. A variety of pathologies, both cardiac and non-cardiac, can cause structural and functional abnormalities to the heart, ultimately leading to the common end stage, the clinical syndrome of heart failure.

Typical symptoms of HF originate from systolic and or diastolic failure and are fatigue, breathlessness, orthopnoea, paroxysmal nocturnal dyspnoea, bilateral peripheral oedema and ascites. Clinical signs more specific to HF are elevated jugular venous pressure, hepatojugular reflux, third heart sound or displaced apical impulse of the heart. The diagnosis of heart failure in the 2016 European Society of Cardiology (ESC) consensus includes typical clinical symptoms and signs of HF, detection of structural heart disease or diastolic dysfunction and elevated levels of natriuretic peptides. HF is further classified according to the left ventricular ejection fraction (LVEF). The ESC consensus distinguishes three types of HF entities according to the LVEF: Heart failure with preserved ejection fraction (HFpEF) with EF $\geqslant$ 50 %, heart failure with reduced ejection fraction (HFrEF) with EF $<$ 40 %, and heart failure with mid range ejection fraction (HFmrEF) with EF of 40$-$49 % (Ponikowski, Voors, et al., 2016).

1.1.2 Epidemiology

Among other cardiovascular diseases HF is one of the leading causes of death in developed countries, as exemplary shown for Germany in in Figure 1.1. HF is a global health care burden of increasing significance in an aging population. Currently an estimated 26 million people are affected worldwide. In comparison, 32 million people are suffering from cancer

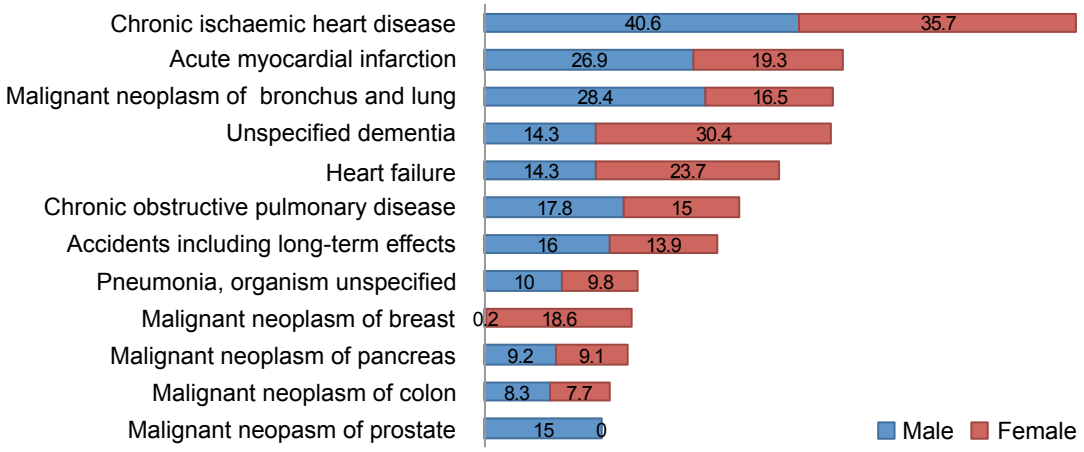

Figure 1.1: Leading causes of death female and male. No. of deaths (in thousands) based on data from the Federal Statistical Office Germany 2018.

(Ponikowski, Anker, et al., 2014; Ambrosy et al., 2014). The overall prevalence of HF is estimated to be 2-3 % of the general population in developed countries (Bui et al., 2011). The crude prevalence of HF in Germany was estimated at 3.4 % in 2017 (Holstiege et al., 2018). The prevalence of HF is increasing in an aging population. In Germany, the estimated crude prevalence increased by 17 % from 2009 to 2017 which is in accordance with the demographic shift towards an aging population as HF disproportionally affects the elderly with 74 % of affected being older than 70 years (Holstiege et al., 2018). The high and also increasing crude prevalence is not attributed to an increasing incidence but rather reflects that more patients live with chronic HF due to improvements in the treatment of underlying heart disease and cardiovascular and non-cardiovascular comorbidities (Roger, 2013).

The incidence of HF in 2017 was estimated at 655 new cases per 100.000 persons at risk in Germany (Holstiege et al., 2018). The age-adjusted incidence of HF in the United States, as well as in Sweden showed a steady to slight declining trend for both sexes (Khera et al., 2017; Zarrinkoub et al., 2013). Observational data from the Framingham heart study from 1990-2009 showed a steady incidence of HF over two decades while the incidence for HFrEF declined, more for men than women, and the incidence of HFpEF increased for both men and women (Tsao et al., 2018). Currently, approximately 50 % of HF patients have HFpEF (Dunlay et al., 2017). Furthermore, the prevalence of HF is predicted to increase by 46 % from 2012 to 2030 in the United States (Heidenreich et al., 2013).

Beyond the increasing prevalence of HF, the mortality is high. On a global perspective, heart failure has a devastating one-year mortality rate of 17–45 % (Ponikowski, Anker, et al., 2014). In Germany during 2009-2013 the two-year mortality rate of newly diagnosed HF was 23 % and increased with age and New York Heart Association (NYHA) classification

reaching 53 % for NYHA IV (Störk et al., 2017). Over the last two decades no significant differences in the mortality of patients with HF including all-cause mortality, cardiovascular and non-cardiovascular mortality was observed for the different HF phenotypes in patience from the Framingham cohort (Tsao et al., 2018). In an observational cohort study in the United Kingdom, average one-year survival after HF diagnosis improved only modestly by 6.6 % from 2000-2016 (Taylor et al., 2019).

Apart from the individual suffering, HF significantly contributes to hospitalizations and health care expenditures. In Germany, HF was, with 2.1 %, the leading cause of hospitalizations and accounted for 8.8 % of in-hospital deaths in 2013 (Christ et al., 2016). The burden that HF poses on hospitalizations is evident as 44 % of hospitalized patients for the treatment of HF had to be readmitted to the hospital in the following year, with a cardiovascular cause in 37 % of cases (Maggioni et al., 2013). The costs for the treatment of HF in Germany amounted to 2.9 billion euro of 249 billion euro total health expenditures in 2006 (Federal Office of Statistics Germany) whereby 45 % of total costs accounted for the in-hospital treatment (Neumann, Biermann, et al., 2009).

1.1.3 Heart failure aetiologies and pathophysiology

Heart failure aetiologies are diverse and difficult to identify as patients often have multiple pathologies with significant overlap, both cardiac- and non-cardiac, that contribute to the development of HF (Ponikowski, Voors, et al., 2016). Three main categories are differentiated: (i) diseased myocardium due to ischaemic heart disease, toxic damage *e.g.* cardiotoxic chemotherapeutic regimens, inflammatory processes both sterile and septic, infiltration both malignant and non-malignant e.g. sarcoidosis, nutritional or hormonal metabolic derangement or genetic abnormalities; (ii) abnormal loading conditions as it is the case for hypertension, valvular or myocardial structural defects, peri- and myocardial processes, high output states or volume overload; (iii) tachy- and bradyarrythmias (Ponikowski, Voors, et al., 2016).

The three phenotypes of HF have common risk factors but differ in the preceding underlying pathologies. Large longitudinal community-based cohort studies have identified risk factors that are associated with the new onset of HF. The Framingham Heart Study identified age, diabetes and a history of valvular disease as a risk predictor for all HF entities while for HFrEF, a history of cardiovascular disease, male sex, elevated total cholesterol, elevated heart rate, hypertension and left ventricular hypertrophy were identified. Risk predictors for the development of HFpEF were obesity, smoking, and atrial fibrillation (Ho et al., 2013). Recent observational data from the European Society of Cardiology Heart Failure Long-Term

Registry found patients with HFrEF in comparison to patients with HFpEF to be younger, more often with a history of ischaemic heart disease, while hypertension or atrial fibrillation was less common. HFmrEF shares more group similarities with HFrEF such as age, gender and previous history of ischaemic heart disease with less dilation of the atria and ventricles (Chioncel et al., 2017). Also, non-cardiac comorbidities are common in patients with HF and significantly contribute to HF mortality (Ergatoudes et al., 2019).

It has been postulated that chronic comorbidities such as hypertension, obesity, type 2 diabetes mellitus, renal insufficiency, pulmonary hypertension, atrial fibrillation as well as advanced age and smoking precede and be the cause of HFpEF whereas HFrEF is more often the result of acute or chronic direct ventricular damage such as due to chronic ischaemic heart disease, myocardial infarction, myocarditis and genetic mutations as illustrated in Figure 1.2 (Simmonds et al., 2020; Vedin et al., 2017).

There are several known different and overlapping pathomechanisms that drive the development of the distinct HF entities. In HFpEF one of the hallmarks is diastolic ventricular dysfunction with increased LV end-diastolic pressure. The underlying pathology that leads to the rise in LV end-diastolic pressure is complex but involves diastolic dysfunction due to impaired energy consuming relaxation and increased passive stiffness of the ventricles. These impairments decrease cardiac output reserve and, in combination with the above listed cardiac and non-cardiac comorbidities that contribute to systemic and ventricular impairments, cause HFpEF symptoms (Gevaert et al., 2019; Zile et al., 2004). Endothelial dysfunction is a major contributor to HFpEF pathophysiology. It was postulated in a paradigm shift by Paulus and Tschöpe (2013) that a chronic pro-inflammatory state induced by comorbidities has the potential to cause coronary microvascular endothelial inflammation. Here, endothelial production of nitric oxide would be impaired which reduces the bioavailability of nitric oxide in cardiomyocytes and disrupt nitric oxide mediated cyclic guanosine monophosphate (cGMP) dependent protein kinase G (PKG) activity leading to hypophosphorylation of PKG target proteins. The effect was postulated to induced hypertrophic signalling and increased cardiomyocyte stiffness which, in synergism with interstitial fibrosis would cause high left ventricular rigidity, concentric hypertrophy and diastolic dysfunction (Paulus and Tschöpe, 2013).

The pathophysiology in HFrEF is fundamentally different but shares overlapping elements with HFpEF. HFrEF is often preceded by an *index event*, chronic or acute, that causes ventricular impairment, substantial cardiomyocyte loss, reduced systolic function and cardiac output (Hartupee and Mann, 2016). Several compensatory mechanisms are involved to maintain adequate cardiac function and tissue perfusion. These compensatory mechanisms include the utilization of the Frank-Starling mechanism, reducing wall-stress by means of ventricular

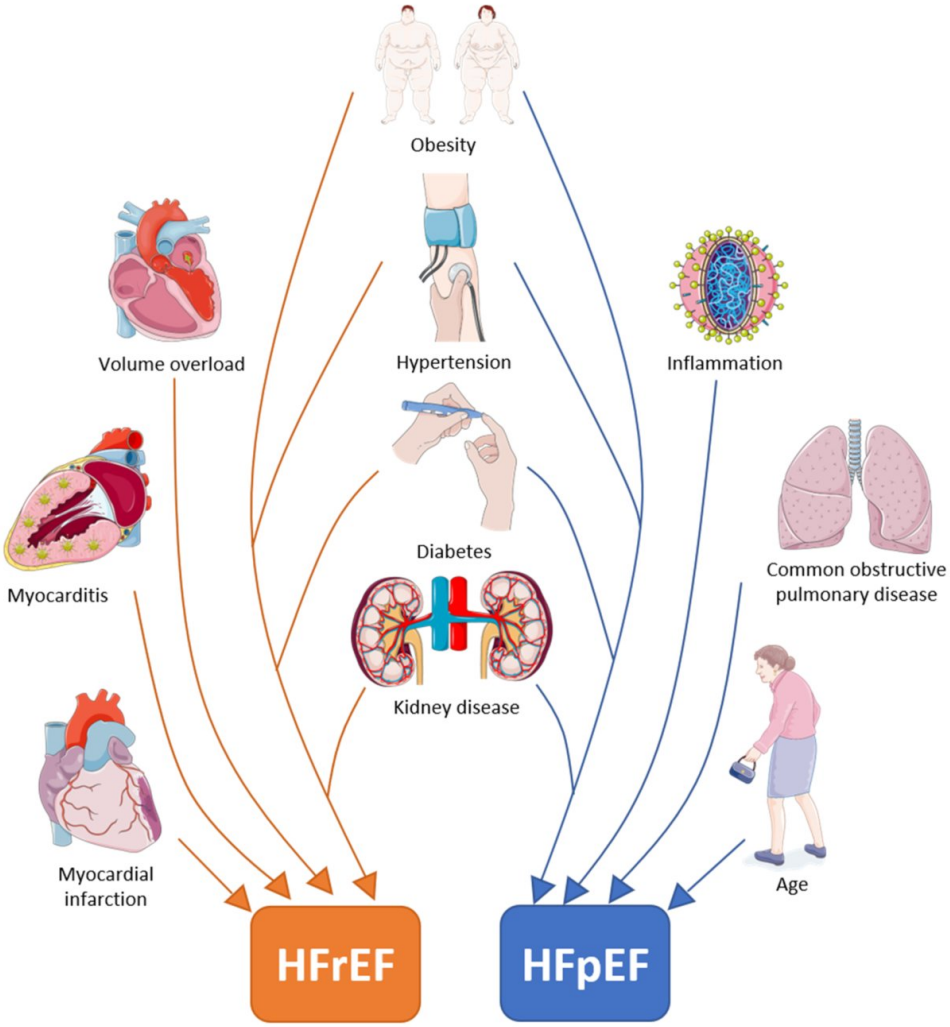

Figure 1.2: Risk factors and comorbidities involved in the aetiology and pathogenesis of heart failure with reduced ejection fraction (HFrEF) and heart failure with preserved ejection fraction (HFpEF). Figure adapted from Simmonds et al. (2020).

remodeling and maintaining tissue perfusion by augmenting neurohormonal and cytokine systems with the effect of increasing heart rate and contractility, retention of salt and water and vascular constriction (Kemp and Conte, 2012; Hartupee and Mann, 2016). Although initially beneficial these chronically activated systems further inflict deleterious effects on cardiac function and significantly contribute to worsening of HF (Hartupee and Mann, 2016).

The pivotal role of the augmented neurohormonal systems, especially the sympathetic nervous system, in HF pathophysiology will be outlined in depth in a following section.

1.2 Pathological hypertrophy and ventricular remodeling in heart failure

The heart is a highly plastic organ that is capable of remodeling in response to altered environmental demand (Hill and Olson, 2008). The enlargement of ventricular mass, termed hypertrophy, due to either physiological or pathological stimuli is accompanied by alterations that chronically influence haemodynamics, chamber shape and myocardial mechanics in an attempt to adapt to the altered demands (Saucerman et al., 2019). Two distinct types of cardiac hypertrophy are: The physiological hypertrophy as a response to physiological stimuli, such as exercise and pregnancy and the pathological hypertrophy which is related to cardiac disease. As illustrated in Figure 1.3, cardiac hypertrophy can further be classified according to the change in ventricular geometry in:

Eccentric hypertrophy which can occur in: (i) physiological hypertrophy characterized by increased ventricular volume with a balanced increase in wall thickness whereby cardiomyocytes increase similarly in width and length; (ii) pathological hypertrophy characterized by ventricular chamber dilatation, wall thinning and lengthening of individual cardiomyocytes by longitudinal addition of sarcomeres where the latter resembles the HFrEF phenotype.

Concentric hypertrophy which is observed in pathological hypertrophy characterized by an initial reduction in ventricular chamber dimensions with increased wall thickness whereby cardiomyocytes increase in thickness more than in length by parallel addition of sarcomeres. It is observed in patients with the HFpEF phenotype but also in earlier stages of HFrEF where ventricular dilation occurs with disease progression (Nakamura and Sadoshima, 2018).

The initial phase of hypertrophic growth is triggered by neurohormonal activation and cell- mediated mechanotransduction (Saucerman et al., 2019). An increased wall-stress, *e.g.* in the case of pressure overload, can be compensated in accordance to the law of LaPlace (1.1) where an increase in ventricular wall tension T due to increased workload and elevated transmural pressure p times radius r can be compensated by an increased wall thickness h (Grossman et al., 1975; Beller and Zaret, 2000; Saucerman et al., 2019).

$$T = \frac{p \cdot r}{2h} \tag{1.1}$$

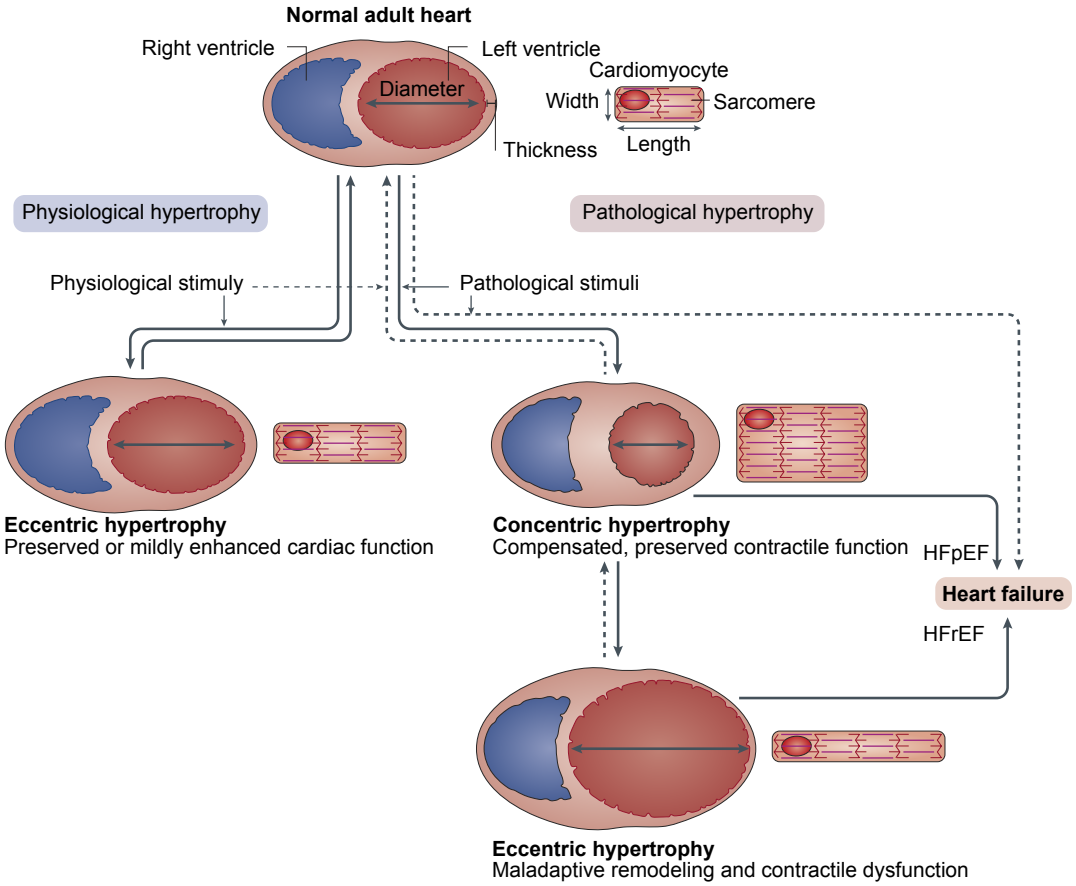

Figure 1.3: Characteristics of pathological and physiological cardiac hypertrophy. Figure adapted from Nakamura and Sadoshima (2018).

In the context of cardiac disease the above outlined principle of hypertrophic growth was first seen as a compensatory mechanism to reduce wall-stress and oxygen consumption and thus thought to be a beneficial response (Hill and Olson, 2008). With advanced knowledge acquired in large community based studies, such as the Framingham Heart Study, it became evident that increased LV mass and hypertrophy is pathologic as it is associated with an increased risk of HF, sudden cardiac death and a major predictor of cardiovascular morbidity and mortality (Haider et al., 1998; Levy, 1991; Ho et al., 2013). Furthermore, LV hypertrophy is accompanied with worse prognosis in patients with HF (Mazza et al., 2005). Treatments that prevent the development or cause regression of LV hypertrophy improve cardiac function and are associated with a reduced risk of cardiovascular complications like new onset of HF, stroke, myocardial infarction and overall risk of death (Larstorp et al., 2012; Mathew et al., 2001; Schmieder et al., 1989)

Pathological hypertrophy, contrary to physiological hypertrophy, is accompanied by pathological LV remodeling, which is a complex cardiac disease related maladaptive transformative

process. It involves cardiomyocyte hypertrophy, cell death, vascular rarefication, fibrosis, reactivation of fetal gene expression, inflammation and electrophysiological alterations. Collectively, these effects significantly contribute to disease progression. (Hartupee and Mann, 2016; Burchfield et al., 2013; Nakamura and Sadoshima, 2018).

There are multiple signaling pathways which are associated with and cause pathological hypertrophy in cardiomyocytes. These include G-protein-coupled receptor (GPCR) signaling, derived from neurohormonal activation, mechanical force, metabolic alterations and mitochondrial dysfunction. Pathological stimuli act via calcium dependant and independent mechanisms, various protein kinases, reactive oxygen species and altered metabolic- and mitochondrial pathways. Ultimately, transcriptional factors are impacted that promote typical maladaptive expression of genes, which are silenced in the adult heart, and thus termed *fetal gene* expression. Typical genes that are affected are sarcomeric proteins such as *Myh6* which is downregulated while *Myh7* is upregulated. Also affected are genes that encode for the transcription of the natriuretic peptides ANP and BNP and, furthermore, proteins that are involved in calcium handling. (Nakamura and Sadoshima, 2018; Samak et al., 2016; Lowes et al., 1997).

A deeper insight into the signalling cascade and transcriptional factors that are involved in β-AR induced pathological hypertrophy in cardiomyocytes will be outlined in a following section.

1.3 Dawn of the neurohormonal hypothesis

In the wake of HF research and treatment, HF was thought to be a condition mainly caused by haemodynamic alterations with increased pre- and afterload and persistent ventricular wall-stress (Packer, 1992). Following ventricular damage the working ventricle was thought to be exposed to an increased wall-stress which chronically would cause deterioration of the healthy myocardium. Attempts to reduce wall-stress by the chronic systemic administration of vasodilating and positive-inotropic drugs in patients with congestive HF failed to halt the progression of HF and did not reduce mortality, even caused accelerated cardiac deterioration and increased mortality (Abrams, 1985; Franciosa et al., 1984; Cohn, Archibald, et al., 1986; Packer, Carver, et al., 1991).

Due to the failure to improve HF survival with drugs applied solely in accordance to the haemodynamic hypothesis and emerging knowledge about the neurohormonal systems in

cardiac disease an alternative hypothesis was pursued. Consequently, it was termed neurohormonal hypothesis which was first conceptualized by Packer (1992). At the core of the neurohormonal hypothesis is that in a state of cardiac impairment neurohormonal systems mainly the SNS and renin-angiotensin-aldosterone-system (RAAS) are activated as a compensatory measure to improve cardiac output. But, when chronically active, these systems exert direct adverse effects on the myocardium independently of their haemodynamic effects (Packer, 1992).

1.4 Sympathetic nervous system in heart failure

1.4.1 Overview of the autonomic nervous system in the heart

The autonomic nervous system with the two opponents the sympathetic and the parasympathetic nervous systems are critically involved in the regulation of various physiologic processes such as cardiovascular homeostasis, digestion, respiration and sexual function. The SNS is predominantly active in response to *fight or flight* challenges and has profound effects on the cardiovascular system. The effects on the heart are: Increasing heart rate (positive chronotropy), increased contractility (positive inotropy), enhanced electrical conductance (positive dromotropy) and enhanced relaxation (positive lusitropy). The effects on the vascular system are: Increased constriction of resistance and cutaneous vessels and decrease in venous capacitance. Collectively these effects increase cardiac output and ensure sufficient end organ perfusion. On the contrary, the parasympathetic nervous system (PNS) promotes *rest and digest* processes in depressing chronotropy and dronotropy with little effect on inotropy or lusitropy and minor effects on the vascular system (Thomas, 2011).

The autonomic nervous system activity is tightly regulated in an interconnected cardio–neural hierarchy which is comprised of three levels: (i) A higher central level including the cortex, medulla and spinal cord, (ii) the intrathoracic extracardiac neurons and ganglia and (iii) the intrinsic cardiac neurons (Herring et al., 2019; Janes et al., 1986). Efferent sympathetic nerve fibers are connected in serial and are comprised of preganglionic neurons that originate from level (i) and integrate in level (ii) and postganglionic neurons with their origin in level (ii) that innervate peripheral target organs. Fibers that innervate the heart follow the main coronary arteries thus innervating the myocardium at the subepicardial level while parasympathetic efferent fibers follow the vagus nerve and are mainly present in the atrium and less abundant in the ventricular myocardium (Triposkiadis et al., 2009).

The efferent signal activity of both the SNS and the PNS are regulated in complex auto-

nomic cardiovascular reflexes with afferent sensory input from arterial baroreceptors located in the aortic arch and carotid sinuses (SNS inhibition), cardiopulmonary baroreceptors (SNS inhibition), cardiovascular-low threshold polymodal receptors (SNS activation) also central and peripheral chemoreceptors (SNS activation) (Floras, 2009; Zhang and Anderson, 2014).

The effect of SNS activation is mediated by several pathways that release the endogenous neurotransmitters norepinephrine or epinephrine: Norepinephrine release from postganglionic fibers in the atria and ventricle, systemic release of epinephrine from the adrenal cortex, local release of norepinephrine and epinephrine in peripheral vessels and circulating norepinephrine as spillover from locally released norepinephrine (Triposkiadis et al., 2009). The vast majority of released norepinephrine is removed from the synaptic cleft by re-uptake into sympathetic nerve terminals by the neuronal uptake1 transporter while the remaining is spilled into the circulation (Leineweber et al., 2002)

1.4.2 Adrenergic receptors and β-AR signaling in the healthy heart

The endogenous catecholamines norepinephrine and epinephrine exert their biological action trough the activation of adrenergic receptors (ARs) which are part of the GPCR family.

There are three known AR subtype families each comprised of three subtypes: three α_1-, three α_2- and three β-AR (Lucia et al., 2018). β-ARs are the predominant AR subtypes that regulate cardiac function (Rockman et al., 2002).

The GPCRs are composed of seven-transmembrane-spanning α-helices and are coupled to heterotrimeric guanine- nucleotide-binding regulatory proteins (G-proteins). Upon ligand binding conformational change occurs in the intracellular domain of the GPCR which activates G-proteins and subsequently transmits the signal into the cell (Rockman et al., 2002).

G-proteins are composed of three subunits: α, β and γ. The α subunit is either bound to nucleotide guanosine triphosphate (GTP) when active or guanosine diphosphate (GDP) when inactive. Upon GPCR stimulation, the receptor is stabilized in an active form and recruits G-proteins in which, GDP is exchanged to GTP. Activated G-protein dissociates into the GTP bound α and the $\beta\gamma$ subunit which triggers diverging cellular responses. G-protein activity is terminated by the hydrolysis of α subunit bound GTP to GDP by the endogenous catalytic subunit (Wang, Gareri, et al., 2018; Rockman et al., 2002). Four distinct G-proteins are divided into four classes and named by their Gα subunit: Gα_{s} (stimulatory), Gα_{i} (inhibitory) Gα_{q} and G$\alpha_{12/13}$ (Wang, Gareri, et al., 2018). All β-AR can bind to and activate Gα_{s} while the β_2- and β_3-AR can additionally couple and activate Gα_{i} (Rockman et al., 2002).

Activated Gα_{s} stimulates adenylyl cyclase (AC) to synthesise the ubiquitous second mes-

senger cyclic adenosine monophosphate (cAMP). cAMP binds and activates effector proteins which impact a plethora of signaling pathways and physiological effects. A key effector is protein kinase A (PKA) which is a major regulator of cardiac function. PKA phosphorylates target proteins that control the excitation-contraction coupling machinery in cardiomyocytes such as phospholamban (PLN), the ryanodine receptor and L-type Ca^{2+} channels as shown in Figure 1.4. $G\alpha_i$ opposes the $G\alpha_s$ effect and inhibits AC (Lohse et al., 2003).

The three β-AR are differently expressed in the healthy human heart: β_1-AR and β_2-AR are roughly expressed in a 7:3 ratio while the β_3-AR is the least abundant AR (Lohse et al., 2003; Woo and Xiao, 2012).

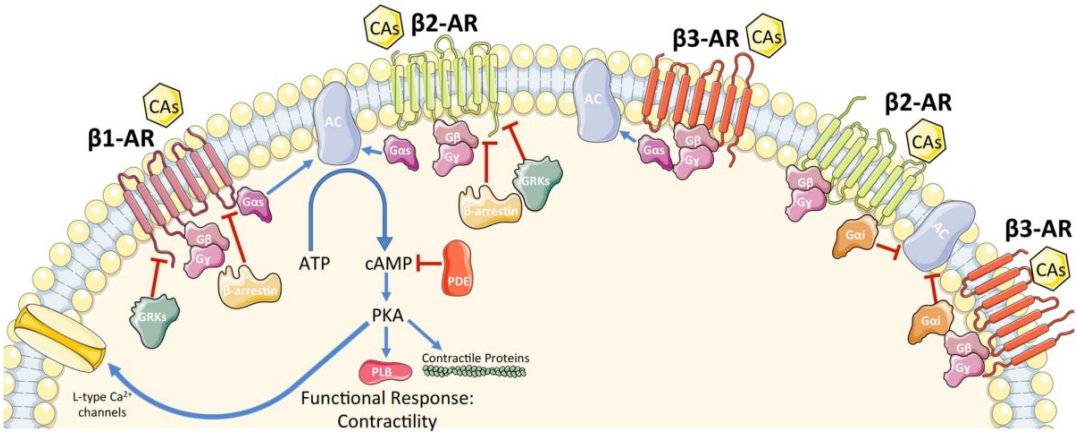

Figure 1.4: Schematic depiction of β-AR signaling in cardiomyocytes. The endogenous catecholamines (CAs) norepinephrine and epinephrine activate β-ARs. Activated $G\alpha_s$ induces adenylyl cyclase (AC) to produce cyclic adenosine monophosphate (cAMP) which activates protein kinase A (PKA) signaling. β_2- and β_3-AR can additionally couple to and activate $G\alpha_i$. cAMP is degraded by phosphodiesterases (PDEs) and receptor signaling negatively regulated by the action of G-protein-coupled receptor kinases (GRKs) and β-arrestin. Figure adapted from Lucia et al. (2018)

In healthy cardiomyocytes cAMP signaling is highly compartmentalized. The β_1-AR are dispersed over the entire surface while functional β_2-AR are confined to the deep transverse tubules (Nikolaev, Moshkov, et al., 2010). Stimulation of the β_1-AR generates far-reaching cAMP gradients while cAMP generated by β_2-AR stimulation is locally confined (Nikolaev, Bünemann, Schmitteckert, et al., 2006). Furthermore, cAMP pools are restricted to subcellular microdomains which are comprised of A-kinase anchoring proteins (AKAPs) that scaffold PKA, PKA substrates and cAMP degrading PDEs to form *signalosomes* around key calcium regulatory proteins (Froese and Nikolaev, 2015). Signaling from activated GPCR is terminated by the action of GRKs. GRKs catalyze the phosphorylation of activated receptor which

enables β-arrestin binding and receptor endocytosis resulting in either receptor degradation or receptor recycling (Sato et al., 2015).

1.4.3 Sympathetic nervous system in heart failure development

Impaired cardiac function due to an *index event* either chronic or acute can activate the SNS. The effect of increased SNS activity are manifold and initially of compensatory nature but chronically significantly contributes to HF deterioration as illustrated in Figure 1.5.

A reduction of the *effective* blood volume causes a decrease of inhibitory sensory input provided by the baro- and mechanoreceptors with the effect of disinhibition of central sympathetic outflow and withdrawl of parasympathetic tone with causes increased chronotropy, inotropy and peripheral vasoconstriction (Hartupee and Mann, 2016). Furthermore, in HFrEF patients, there is a profound sympathetic/parasympathetic disequilibrium with sustained SNS overactivity in part due to altered autonomic reflexes such as suppressed inhibitory cardiopulmonary reflexes and augmented sympatho-excitatory reflexes such as the peripheral chemoreceptor reflex (Floras and Ponikowski, 2015). The depicted concept of mere SNS overactivity in response to reduced *effective* blood volume and or cardiac output in HF development is over-simplistic. There are many neuro-cardiac feedback mechanisms, many shared cardiac and neurologic comorbidities that impact the heart as well as cause perfusion deficits to the brain. These impairments elicit a bi-directional effect that gave rise to the concept of the *cardio-cerebral* syndrome in HF (Doehner et al., 2018).

Augmented SNS activity results in increased norepinephrine and epinephrine release with significant spillover into the circulation resulting in increased vasoconstriction and elevated vascular systemic resistance. Vasoconstriction reduces the blood flow to the kidney which additionally to increased direct β_1-AR stimulation in the juxtaglomerular apparatus triggers the release of renin and the activation of the RAAS. The effect of activated RAAS is increased salt and water retention and thus expansion of the extracellular fluid volume (Aoi and Weinberger, 1976; Hartupee and Mann, 2016). RAAS activation in HF patients furthermore triggers the angiotensin II mediated nonosmotic release of arginine vasopressin which contributes to the development of volume overload and hyponatraemia, peripheral vasoconstriction and endothelin release (Bekheirnia and Schrier, 2006). The natriuretic peptide system counterbalances RAAS activity. Volume overload triggers the release of natriuretic peptides which reduces the volume overload and preload to the heart by cGMP dependent vasodilation, increased sodium / water excretion and inhibited renin release. In HF patients the natriuretic peptide system is impaired due to peripheral natriuretic peptide resistance (Volpe et al., 2016; Bekheirnia and Schrier, 2006). The activation of the SNS increases vascular re-

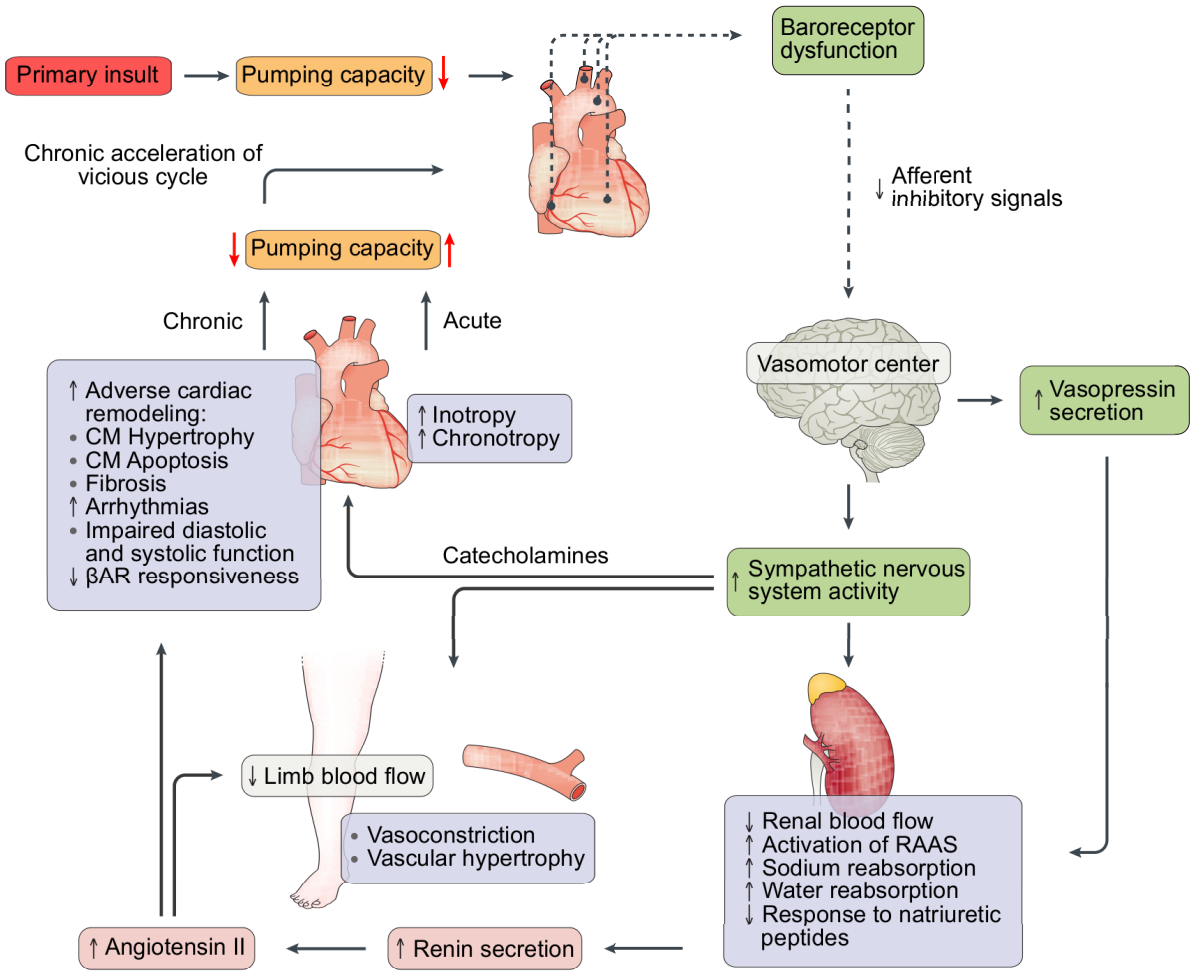

Figure 1.5: Vicious cycle of elevated sypathetic nervous system activity in the pathogenesis of HF. Figure adapted from Hartupee and Mann (2016) and Eschenhagen (2008).

sistance and elevates venous tone trough peripheral vasoconstriction directly trough SNS innervation but also by the action of circulating catecholamines and other vasoconstrictive mediators such as angiotensin II, vasopressin and endothelin (Hartupee and Mann, 2016).

In healthy individuals short term demand specific elevated venous tone is beneficial as it increases cardiac output by augmenting preload to the heart and utilizing the Frank-Starling mechanism. In cardiac impairment although this rise in LV filling pressure, together with increased afterload in a state of increased vascular resistance, exerts mechanical maladaptive strain to the heart and promotes accelerated neurohormonal activation. Besides the increased haemodynamic load the SNS and RAAS inflict hormonal and metabolic derangements that elicit a direct toxic effect to the myocardium which further promotes adverse ventricular remodeling and worsening of HF (Hartupee and Mann, 2016).

In patients with advanced congestive HF urine excretion of norepinephrine is increased while atrial and ventricular norepinephrine concentrations are markedly reduced (Chidsey et al., 1965). Furthermore, plasma norepinephine levels are significantly elevated in patients with congestive HF and were found to be an independent risk factor for mortality (Cohn, Levine, et al., 1984). Sustained SNS stimulation in HF has profound effects on β-AR signaling in the heart.

In patients with advanced HF, β-AR are reduced and functionally impaired. Here, cardiac β-AR density as well as β-AR-AC mediated contractility is markedly reduced in ventricular preparations as well as the positive inotropic reserve *in vivo* (Bristow, Ginsburg, Minobe, et al., 1982; Colucci et al., 1988). Also, the ventricular β_1-AR density is significantly reduced while β_2-AR density remains unaltered, changing the β_1 to β_2-AR ratio to roughly 6:4 (Bristow, Ginsburg, Umans, et al., 1986; Engelhardt, Böhm, et al., 1996). In terminal HF patients, the β-AR signaling cascade is further impaired by an in increase in the expression of GRKs which uncouple the receptors from downstream G-protein signaling (Ungerer et al., 1993; Agüero et al., 2012; Rockman et al., 2002) and an increase in the expression of $G\alpha_i$ (Neumann, Schmitz, et al., 1988; Eschenhagen et al., 1990). Furthermore, the protein phosphatase-1 inhibitor-1 (I-1), which is a PKA substrate and an internal amplifier of β-AR signaling, is significantly reduced (El-Armouche, Pamminger, et al., 2004).

The downregulation and desensitization of the β-AR signaling cascade protects the heart from sustained chronic β-AR stimulation which affects cell viability and induces pathological hypertrophy.

1.5 Effects of chronic β-AR signaling on cardiomyocyte viability and induction of hypertrophy

Chronic SNS stimulation of cardiomyocytes exerts a direct toxic affect and induces cardiomycyte hypertorphy. Norepinephrine at concentrations found in patients with heart failure can reduce the *in vitro* viability of isolated ventricular cardiomyocytes and induce apoptosis (Mann et al., 1992; Communal et al., 1999; Chesley et al., 2000). The hypertrophic effects of chronic SNS stimulation in cardiomyocytes are predominantly mediated via the $G\alpha_s$ coupled β_1-AR (Rockman et al., 2002). There are multiple pathways involved in β_1-AR induced pathological hypertrophy:

One pathway involves the action of GRKs which also terminate β_1-AR signaling by desen-

sitization. GRK2 and GRK5 are significanty upregulated in the failing human heart (Agüero et al., 2012). In mice, GRK5 contributes to pathological hypertrophy in a GPCR independent mechanism by calmodulin dependent nuclear translocation where it acts as a class II histone deacetylase and induces hypertrophic gene transcription by de-repressing transcription factor MEF2 (Martini et al., 2008; Sato et al., 2015). Furthermore, exchange protein directly activated by cAMP (EPAC) 1 is upregulated in HF and upon β-AR inflicted cAMP stimulation. It is critically involved in the development of pathological hypertrophy by activating Ca^{2+}/calmodulin-dependent protein kinase II (CaMKII) pathway promoting NFAT and MEF2A dependent transcription of hypertrophic genes (Métrich et al., 2008). Finaly, β-AR stimulation can phosphorylate ERK1/2 via activated AC and $G\alpha_s$ derived $\beta\gamma$ subunit that enables an additional ERK autophosporylation at the ERK^{Thr188} motif and subsequent nuclear accumulation and transcription of hypertrophic genes in mice (Vidal et al., 2012).

The above outlined findings of an inverted relationship between elevated SNS activity and HF survival, detrimental β-AR *in vitro* effect on cardiomyocytes, downregulation and desensitization of β-AR signaling cascade in HF patients and, furthermore, the successful clinical use of β-AR blockers in the treatment of HF patients have highlighted the significance of β-AR signaling in HF development (Lohse et al., 2003). The challenging question of β_1-AR downregulation and impaired signaling as a cause or consequence, protective or maladaptive mechanism in cardiac disease is a matter of debate. The pending question was further elucidated in transgenic mice by manipulating crucial components of the downstream signaling cascade (Eschenhagen, 2008).

1.6 Targeting cardiac β_1-AR downstream signaling in the mouse

The effect of enhanced β_1-AR signaling on cardiomyocytes was shown by overexpression of key signaling cascade components. Engelhardt, Hein, et al. (1999) generated transgenic mice with cardiac specific overexpression of the human β_1-AR. These mice exhibited increased contractility at a young age but with advanced age developed cardiomyocyte hypertrophy and heart failure with reduced ejection fraction (EF) and interstitial fibrosis. Similar results were obtained in mice with cardiac specific $G\alpha_s$ overexpression which exhibited normal heart function at rest with augmented inotropic and chronotropic responses to sympathetic stimulation. But, similar to the β_1-AR overexpressing mice, developed cardiomyocyte hypertrophy and interstitial fibrosis with advanced age (Iwase, Bishop, et al., 1996). Also, cardiac specific

overexpression of the catalytic subunit of PKA resulted in cardiomyocyte hypertrophy, dilated cardiomyopathy, reduced contractility and increased susceptibility to sudden cardiac death (Antos et al., 2001). Another stimulatory component is the phosphatase-1 inhibitor-1 (I-1) which is a PKA substrate and activated by phoyphorylation. I-1 phosphorylates and deactivates phosphatase type 1 (PP-1) which amplifies β-AR signaling (Wittköpper, Dobrev, et al., 2011). Mice with cardiac specific overexpression of I-1 or a consitutively active I-1 develop cardiac hypertrophy and cardiac deterioration with aging (El-Armouche, Wittköpper, et al., 2008; Wittköpper, Fabritz, et al., 2010). Highlighting the significance of enhanced β_1-AR signaling was that the deleterious effects of cardiac specific Gα_s overexpression could be averted by the chronic administration of the β-AR blocker propranolol (Asai et al., 1999).

There are only a few mouse models with disruption of stimulatory components of the β-AR signaling cascade. Complete deletion of the β_1-AR in mice resulted in increased embryonic lethality but mice that reached adulthood exhibited normal resting heart function and exhibited lost chronotropic and inotropic response to β-AR stimulation (Rohrer et al., 1996). Complete deletion of *GNAS1*, the gene encoding Gα_s, is embryonically lethal and heterozygotes exhibited significant early postnatal lethality and distinct phenotypes such as a square shaped body, edema and neurological abnormalities (Yu et al., 1998). Also a model targeting a stimulatory component of the β-AR signaling cascade was the disruption of AC type 5 by Okumura et al. (2003). In a pressure overload heart failure model the AC5$^{-/-}$ mice were protected from functional cardiac deterioration most likely due to the observed reduction in cardiomyocyte apoptosis but in comparison to to their wild type littermates, they developed comparable cardiomyocyte hypertrophy. Cardiomyocyte specific knockout of I-1 resulted in normal cardiac structure and normal maximal response to β-AR stimulation while also being protected from cardiac hypertrophy inflicted by chronic β-AR stimulation (El-Armouche, Wittköpper, et al., 2008).

To further shed light on the role of β-AR signaling cascade in the pathogenesis of HF the so far unsuccessful inhibition of Gα_s by *GNAS1* deletion was pursued by Streit et al. (2016) with the cardiomyocyte specific overexpression of a dominant negative Gα_s mutant. These transgenic mice exhibited mild bradycardia and decreased myocardial contractility at rest but otherwise had normal cardiac physiology. In response to chronic β-AR stimulation, these mice were protected from cardiac hypertrophy and fibrosis.

1.7 Dominant Negative Gα_s mutant

The potential of blocking detrimental β_1-AR signaling directly in cardiomyocytes in a state of SNS overactivity and cardiac disease utilizing a dominant negative Gα_s mutant warrants further exploration. Transgenic mouse models pose the drawback that expression of the target gene is time consuming and difficult to implement *e.g.* in the context of post intervention expression. Thus a gene therapeutic approach to achieve cardiomyocyte specific expression of a dominant negative Gα_s mutant utilizing AAV for *in vivo* gene transfer is more versatile and was pursued in this thesis. The dominant negative Gα_s mutant (DNG) used in this thesis was generated by Berlot (2002). This mutant was created from the rat Gα_s complementary DNA and contained three functionally mutated sites which impact Gα_s signaling as shown in Table 1.1.

Table 1.1: DNG mutations and effects

Gα_s Mutation sites	Effect
	Increased receptor affinity
α3β5	Decrease receptor-mediated activation
	Impaired activation of adenylyl cyclase
G226A	Increased affinity for $\beta\gamma$
A366S	Decreased affinity for GDP

In *in vitro* experiments DNG inhibited signaling from the Gα_s coupled luteinizing hormone receptor by 97% and calcitonin receptor by 100% in HEK-293 cells (Berlot, 2002).

1.8 Aim of thesis

The β-AR Gα_s cAMP signaling cascade is critically involved in cardiac function but also a major driver of pathological hypertrophy and remodeling which significantly contributes to morbidity and mortality in patients with HF. Blocking Gα_s mediated signaling using a dominant negative Gα_s protein (DNG) is a promising approach to block detrimental chronic β-AR stimulation that is present in a state of sympathetic hyperactivation observed in patients with HF. DNG has so far not been expressed in the cardiomyocyte system.

Aims of this thesis are:

- Generation of DNG expression vectors for the *in vitro* and *in vivo* gene transfer in cardiomyocytes
- Test DNG functionality to block β-AR signaling in HEK cells and adult rat ventricular cardiomyocytes (ARVCMs)
- Test DNG ability to block chronic β-AR stimulation induced hypertrophic growth *in vitro*
- Analyze AAV-DNG injected mice for DNG expression
- Assess AAV-DNG effect on cardiac function at rest and in an model of chronic β-AR stimulation induced cardiac hypertrophy

2 Materials and Methods

2.1 Materials

2.1.1 Animals

Table 2.1: Animals used.

Kind	Strain	Source
Mouse	57Bl6/J	Charles River
Mouse	C57Bl6/N	O. Müller
Rat	Wistar	Janvier

2.1.2 Eukaryotic and prokaryotic cells

Table 2.2: Eukaryotic and prokaryotic cells.

Cell line	Manufacturer	Catalogue number
HEK293A	Invitrogen	R705-07
OneShot™Top10 *E.coli*	Invitrogen	C404010

2.1.3 DNA templates, plasmids and vectors

Table 2.3: DNA templates, plasmids and vectors.

Denotation	Manufacturer / Source	Reference / Catalogue no.
DNG	Gift from K. Movahedi	(Berlot, 2002; Movahedi et al., 2018)
MHC-Cherry2AHydro	V. Nikolaev	
pcDNA™3	Invitrogen	V79020

Table 2.3: DNA templates, plasmids and vectors.

Denotation	Manufacturer / Source	Reference / Catalogue no.
pds-TnT-Fluc (dsAAV9)	O. Müller	
pSSV-TnT-Fluc (ssAAV9)	O. Müller	(Werfel et al., 2014)
pDONR™221	Invitrogen	12536-017
pAd-CMV-V5-DEST™	Invitrogen	V493-20
dsAAV9-TnT-mCherry	O. Müller	
Adv-GFP (Type 5)	Gift from K. Stathopoulou	(Stathopoulou et al., 2014)

2.1.4 DNA oligonucleotides

DNA oligonucleotides were purchased from Eurofins Genomics (Ebersberg), dissolved in Ampuwa H_2O as indicated in the instructions and stored at -20 °C.

Table 2.4: Oligonucleotides used for cloning.

Denotation	Sequenze (5'-3')
DNGNcoIfor	AACCATGGGCTGCCTC
DNGNotIrev	AAAGCGGCCGCTTAGAGCAGCTCGTATTGGC
DNGRsrIIfor	AAACGGACCGATGGGCTGCCTCGG
DNGFseIrev	AAAGGCCGGCCTTAGAGCAGCTCGTATTGGC
CherryHindfor	AAAAAGCTTACCATGGTGAGCAAGGG
CherryRsrIIrev	CATCGGTCCGGGATTGC
pcDNA3aatBfor	GGGGACAAGTTTGTACAAAAAAGCAGGCTGACTCACTATAGGGA GACCC
pcDNA3aatBrev	AAAGCTGGGTGATGGCTGGCAACTAGAAG

Table 2.5: Oligonucleotides used for rt-qPCR.

Denotation	Sequenze (5'-3')
GAPDHfor	CGTCCCGTAGACAAA
GAPDHrev	GAATTTGCCGTGAGT
DNGfor	ACAACAAATGGCTGCGTGAC
DNGrev	AGCGAACTCTGGAAAGTAGTCC

Table 2.5: Oligonucleotides used for rt-qPCR.

Denotation	Sequenze (5'-3')
GNASfor	ACGTGCCGAACTTTGACTTC
GNASrev	CACGCACTCCCTCATCCTC

2.1.5 NanoString®hypertrophy panel

The NanoString® panel was composed by the NanoString® core facility at the institute of Experimental Pharmacology and Toxicology at the UKE. Target and housekeeping genes used are displayed in Table 2.6.

Table 2.6: Nanostring®hypertrophy panel.

Gene alias	Protein Name	Use
Ppp1r1a	Protein phosphatase inhibitor-1	β-AR signaling
Fhl1	Four-and-a-half-LIM-domains 1	Hypertrophy
Fhl2	Four-and-a-half-LIM-domains 2	Hypertrophy
Myh6	Myosin heavy chain 6	*Fetal* gene program
Myh7	Myosin heavy chain 7	*Fetal* gene program
Nppa	Natriuretic peptide A	*Fetal* gene program
Nppb	Natriuretic peptide B	*Fetal* gene program
Postn	Periostin	Fibroblasts-specific
Col1a1	Collagen type I alpha 1	Fibrosis
Col3a1	Collagen type III alpha 1	Fibrosis
Gapdh	Glyceraldehyde-3-phosphate dehydrogenase	Housekeeping
Actb	Actin beta	Housekeeping
Pgk1	Phosphoglycerate kinase 1	Housekeeping
Tubb5	Tubulin, beta 5 class I	Housekeeping
Cltc	Clathrin heavy chain	Housekeeping
Abcf1	ATP binding cassette subfamily F member 1	Housekeeping

2.1.6 Antibodies

Antibody solvents were prepared from TBS-T for western blot and antibody-diulent for IHC as stated in Table 2.7.

Table 2.7: Primary antibodies.

Denotation	Species	Use	Dilution	Solvent	Source, Catalog. no.
Anti-GAPDH	mouse	WB	1:160.000	5 % milk	Bio Trend, 5G4
Anti-Calsequestrin	rabbit	WB	1:5.000	3 % BSA	Thermo Sci., PA1-913
Anti-mCherry	goat	IHC	1:750	5 % donkey s.	SICGEN, AB0040-200
		WB	1:500	5 % milk	
anti-Gα_s	rabbit	WB	1:2000	5 % milk	Laurinda Jaffe
anti-PLN	rabbit	WB	1:2500	5 % milk	Badrilla, ab126174
anti-p-PLN^{Ser16}	rabbit	WB	1:5000	5 % milk	Badrilla, A010-12

Table 2.8: Secondary antibodies.

Denotation	Species	Use	Dilution	Solvent	Source, Catalog. no.
anti-mouse-HRP	goat	WB	1:5.000	5 % milk	Biorad, 170-5047
anti-rabbit-HRP	goat	WB	1:5.000	5 % milk	Biorad, 170-5046
anti-goat-HRP	donkey	WB	1:5.000	5 % milk	Santa Cruz, sc-2020
anti-goat Alexa Fluor®647	donkey	IHC	1:500	AB-diulent	Invitrogen, A32849

2.1.7 Chemicals and cell culture supplements

Table 2.9: Chemicals and cell culture supplements.

Chemical	Manufacturer, Catalogue no.
(-)-Isoproterenol hydrochloride	Sigma Aldrich, I6504
β-Mercaptoethanol	Sigma Aldrich, M6250-100ML
2-Propanol	Chemsolute, 1136.1000
2,3-Butandione monoxime (BDM)	Sigma Aldrich, B0753-25G
3-Isobutyl-1-Methylxanthine (IBMX)	AppliChem, A0695-0001
3M Natriumacetat ph 5.2	AppliChem, 3947-0100
4-(2-hydroxyethyl)-1- piperazineethanesulfonic acid (HEPES)	AppliChem, A1069,0500
Acrylamide (Rotiphorese Gel 40)	Carl Roth, 3029.1
Agarose universal peqGold	VWR, 35-1010

Table 2.9: Chemicals and cell culture supplements.

Chemical	Manufacturer, Catalogue no.
Agarose, Plaque GP	Biozym, 840101
Ammonium persulfate (APS)	Sigma Aldrich, A3678-25G
Ampicillin	Roth, K029.1
Ampuwa water	Fresenius, 40 676.00.00
Antibiotic-Antimycotic, 100 x	Gibco, 15240062
Bovine serum albumin (BSA)	Sigma Aldrich, A6003-25G
Bromphenolblue	Carl Roth, A512.1
$CaCl_2$ x 2 H_2O	Sigma Aldrich, C8108-500G
Citrate pH 6 (10x)	Dako, S2369
Creatine	Sigma Aldrich, C360-100G
CsCl	Sigma Aldrich, C3032-100G
Custodiol	VK Siemens, 31268.00.00
D-(+)-Glucose	Sigma Aldrich, G7528-250G
Developer concentrate	Adefodur, 00176
Dimethyl sulfoxide (DMSO)	Sigma Aldrich, 00176
Donkey serum	Sigma Aldrich, D9663-10ML
Dulbecco's Modified Eagle's Medium (DMEM)	Biochrom, F0445
Ethanol, 70 % denatured	Chemsolute, 2202.5
Ethanol, Rotipuran, >99.8 % p.a.	Carl Roth, 9065.2
Ethylenediaminetetraacetic acid (EDTA)	AppliChem, A1104,0500
Ethyleneglycoltetraacetic acid (EGTA)	Sigma Aldrich, E4378
Fetal calf serum (FCS)	Merck, S0615
Fixer concentrate	Adefodur, 01176
Forskolin	Sigma Aldrich, F6886
Glycerol	Sigma Aldrich, G5516-100ML
Glycine	Carl Roth, 3908.2
HCl, 37 %	Carl Roth, 9277.1
Heparin-Natrium, 5.000 I.E./mL	Leo Pharma AS, 050618
Immersion liquid type F	Leica, 11515859
Insulin-Transferrin-Selenium (ITS) 100x	Gibco, 51500-056
Iscove Basal Medium	Biochrom, FG 0465
Isoflurane (Forene)	Abbvie, B506

Table 2.9: Chemicals and cell culture supplements.

Chemical	Manufacturer, Catalogue no.
Kanamycin	Roth, T832.1
KCl	Merck, 1.04933.0500
KH_2PO_4	Merck, 1.04873.0250
$KHCO_3$	Merck, 1.04854.0500
L-Carnitine	Sigma Aldrich, C0283-100G
L-Glutamine	Merck, K0282
Laminin	Sigma Aldrich, L2020
LB-Agar	AppliChem, A0927
LB-medium	AppliChem, A0954
Lipofectamine 2000	Invitrogen, 11668-027
M199 Medium	Invitrogen, 11150-059
Methanol	Carl Roth, 4627.24
$MgCl_2$ x 6 H_2O	Sigma Aldrich, M2670
$MgSO_4$ x 7 H_2O	Merck, 1.05886.0500
Midori Green	Nippon Genetic, MG04
Milk powder	Carl Roth, T145.1
Na-Pyruvate	Sigma Aldrich, P8574
Na_2HPO_4 x $2H_2O$	Merck, 1.06580.0500
NaCl	Merck, 3957.1
$NaHCO_3$	Merck, 1.06329.0500
NaN_3	Sigma Aldrich, S2002-25G
NaOH	Chemsolute, 1340.1
Penicillin-Streptomycin (P/S) 100x	Merck, A2212
Phosphate buffered saline (PBS)	Merck, L182-01
Polyethylene Glycol 8000 (PEG 8000)	Th.Geyer, RO/00002632/001000
Ponceau S solution	Sigma Aldrich, P7170
RNase ERASE	MP Biomedicals, 821682
RNase-free water	GE Healthcare, B-003000-WB-100
SDS-Solution, 20 %	AppliChem, A0675,0500
Sodium dodecyl sulfate (SDS)	Sigma Aldrich, 05030
Sucrose	Sigma Aldrich, S0389
Sudan Black B	Roth, 0292.1

Table 2.9: Chemicals and cell culture supplements.

Chemical	Manufacturer, Catalogue no.
Taurine	AppliChem, A1141,1000
Tetramethylethylenediamine (TEMED)	Sigma Aldrich, T9281-100ML
Tris-(hydroxymethyl)-aminomethan (TRIS)	Carl Roth, 4855.2
Tris-acetate-EDTA (TAE) buffer 10x	AppliChem, A1691
Triton X-100	Sigma Aldrich, X100-100ML
Triton X-100 Solution, 10 %	AppliChem, A1287,0100
Tween 20	Sigma Aldrich, P1379-500ML
Xylol	Chemsolute, 326.2500

2.1.8 Enzymes and kits

Table 2.10: Enzymes and kits.

Denotation	Manufacturer, Catalogue no.
10x Ligase buffer	NEB, B0202S
10x Pfu buffer	Promega, M774A
6x DNA loading dye	NEB, B7024S
Antibody diulent	DCS, ALI20R500
Collagenase type II (ACT 245U/mg)	Worthington, LS0004174
cOmplete tablets	Roche, 04 693 116 001
CutSmart buffer	NEB, B7204S
DAPI fluoromount-G	Southern Biotech, 0100-20
DNase I	Roche, 11284932001
dNTPs	Promega, U1240
Gatewac Clonase II enzyme mix	Invitrogen, 11791020
HindIII-HF	NEB, R3104S
Iscript cDNA synthesis kit	BioRad, 170-8890
KpnI-HF	NEB, R3142S
Midipräp	Qiagen, 12945
NcoI-HF	NEB, R3193S
NotI-HF	NEB, R3189S
PacI	NEB, R0547S

Table 2.10: Enzymes and kits.

Denotation	Manufacturer, Catalogue no.
PCR purification kit Qiaquick	Qiagen, 28104
Pfu polymerase	Promega, M7741
PhosphoSTOP	Roche, 4906837001
Pierce BCA protein assay kit	Thermo Scientific, 23227
Pierce Coomassie protein assay kit	Thermo Scientific, 23200
Proteinase K	Appli Chem, A3830,0500
QIAprep spin miniprep kit	Qiagen, 27106
QiaQuick gel extraction	Qiagen, 28706
RNeasy fibrous tissue mini kit	Qiagen, 74704
Rotor-Gene SYBR green PCR kit	Qiagen, 204074
RsrII-HF	NEB, R0501S
SuperSignal West Pico PLUS	Thermo Fisher, 34580
T4 DNA ligase	NEB, Mo2026
Trypsin, 2.5 %	Gibco, 15090-046
Trypsin/EDTA-Solution (0.05/0.02 %)	Biochrom, L2143
XmaI-HF	NEB, R0180S
DNA ladder, 100 bp	NEB, N3231S
Protein Marker V peqGold	Peqlab, 27-2210

2.1.9 Buffers

If not specified, buffers and solutions were prepared with ultra pure water produced in RiOs™3 water purification system.

Buffers and solutions used for ARVCM isolation and culture

Table 2.11: BSA stock solution, 10 %. Dissolved in H_2O Ampuwa, sterile filtered. Aliquots of 500 µl stored at -20 °C.

Compound	Concentration
BSA	10 %

Table 2.12: Calcium chloride solution, 100 mM. Dissolved in H_2O Ampuwa, sterile filtered. Stored at 4 °C.

Compound	Concentration
$CaCl_2$ x 2 H_2O	100 mM

Table 2.13: Perfusion buffer, 10x. Dissolved in H_2O Ampuwa, sterile filtered. Stored at 4 °C.

Compound	Concentration
NaCl	120.4 mM
KCL	14.7 mM
KH_2PO_4	0.6 mM
Na_2HPO_4 x $2H_2O$	0.6 mM
$MgSO_4$ x 7 H_2O	1.2 mM
Na-HEPES	10 mM

Table 2.14: Perfusion buffer, 1x. Dissolved in H_2O Ampuwa, Freshly prepared before use.

Compound	Concentration
Perfusion buffer 10 x	1x
$NaHCO_3$	4.6 mM
Taurin	30 mM
BDM	10 mM
Glucose	5.5 mM

Table 2.15: Digestion buffer. Freshly prepared before use.

Compound	Mass/Volume
Collagenase Type II	100 mg
$CaCl_2$ 100 mM	20 µl
Perfusion buffer 1x	50 ml

Table 2.16: Stop buffer. Freshly prepared before use.

Compound	Mass/Volume
BSA 10 %	13 ml
$CaCl_2$ 100 mM	16.25 µl
Perfusion buffer 1x	ad 130 ml

Table 2.17: Ca Stop buffer I. Freshly prepared before use.

Compound	Mass/Volume
$CaCl_2$ 100 mM	25 µl
Stop buffer	25 ml

Table 2.18: Ca Stop buffer II. Freshly prepared before use.

Compound	Mass/Volume
$CaCl_2$ 100 mM	100 µl
Stop buffer	25 ml

Table 2.19: Ca Stop buffer III. Freshly prepared before use.

Compound	Mass/Volume
$CaCl_2$ 100 mM	225 µl
Stop buffer	25 ml

Table 2.20: ACCT culture and hypertrophy medium. Dissolved in M199 Medium. Freshly prepared before use, stored at 4 °C.

Compound	Concentration
Creatine	5 mM
L-Carnitine	2 mM
Taurin	5 mM
HEPES	25 mM
BDM	10 mM
BSA	0.2 % (v/v)
ITS	1 % (v/v)
P/S	1 % (v/v)
L-Glutamine	1 % (v/v)

Buffers and solutions used for HEK293A cell culture, adenovirus amplification, purification and plaque assay

Table 2.21: HEK293A culture medium. Dissolved in DMEM medium, stored at 4 °C.

Compound	Concentration
FCS	10 %
Glutamine	1 %
Penicillin/Streptomycin	1 %

Table 2.22: Adenovirus amplification medium. Dissolved in DMEM medium, stored at 4 °C.

Compound	Concentration
FCS	5 %
Glutamine	1 %
Penicillin/Streptomycin	1 %

Table 2.23: 20 % Triton/PBS. Sterile filtered, stored at 4 °C.

Compound	Volume
Triton X 100	10 ml
PBS	40 ml

Table 2.24: 20 % PEG 8000/2.5 M NaCl. Sterile filtered, stored at 4 °C.

Compound	Mass/Volume
NaCl	292.6 g
$20H_2O$	Ad 2 l

Table 2.25: PBS, pH 8.0. Adjusted to pH 8.0, sterile filtered, stored at 4 °C.

Compound	Volume
PBS	500 ml

Table 2.26: 10x Sucrose-buffer, pH 8.0. Adjusted to pH 8.0, sterile filtered, stored at 4 °C.

Compound	Mass/Volume
Tris	24.22 g
$MgCl_2$ x 6 H_2O	8.13 g
D-(+)-Sucrose	800 g
H_2O	Ad 2 l

Table 2.27: 2x IMDM. Sterile filtered, aliquots of 26 ml stored at -20 °C.

Compound	Mass/Volume
IMDM	Powder of two bottles
$NaHCO_3$	6.05 g
H_2O	Ad 1 l

Table 2.28: 1.5 % Agarose. Autoclaved, stored at 4 °C.

Compound	Mass/Volume
Agarose	1.5 g
H_2O	Ad 100 ml

Table 2.29: Plaque assay medium. Dissolved in Iscove basal medium, stored at 4 °C.

Compound	Concentration
FCS	5 %
Antibiotic/Antimycotic	1 %

Buffers and solutions used for cloning

Table 2.30: 5-KCM buffer. Dissolved in H_2O Ampuwa, sterile filtered, stored at 4 °C.

Compound	Concentration
KCL	500 mM
$CaCl_2$	150 mM
$MgCl_2$	250 mM

Table 2.31: Ampicilin stock. Dissolved in H_2O Ampuwa, sterile filtered, stored at -20 °C.

Compound	Concentration
Ampicilin	5 % (m/v)

Table 2.32: Kanamycin stock. Dissolved in H_2O Ampuwa, sterile filtered, stored at -20 °C.

Compound	Concentration
Kanamycin	5 % (m/v)

Table 2.33: LB-medium. Autoclaved, stored at 4 °C.

Compound	Mass/Volume
LB-medium powder	25 g/l

Table 2.34: LB agar plates. Autoclaved, cooled to approx. 60 °C prior to mixing with antibiotic. Plated, stored at 4 °C.

Compound	Mass/Volume
LB-Agar powder	40 g/l
Antibiotic stock	1:1000 (v/v)

FRET Buffer

Table 2.35: FRET buffer. Adjusted to pH 7.4, stored at RT.

Compound	Concentration
NaCl	144 mM
KCl	5.4 mM
$MgCl_2$ x 7 H_2O	1 mM
$CaCl_2$	1 mM
HEPES	10 mM

Buffers used for western blot

Table 2.36: Homogenization buffer stock. Adjusted to pH 7.4. 9 ml aliquots stored at -20 °C

Compound	Concentration
EGTA	1 mM
HEPES	10 mM
NaCl	150 mM
Sucrose	300 mM

Table 2.37: Homogenization buffer. Aliquots of 1 ml stored at -20 °C.

Compound	Volume
Homogenization buffer, stock	9 ml
Triton X-100, 10 %	1 ml
Phosphatase inhibitor	1 tab
Protease inhibitor	1 tab

Table 2.38: SDS Stop, 3x. Adjusted to pH 6.7, stored at RT.

Compound	Concentration
Tris	200 mM
SDS	6 % (v/v)
Glycerin	15 % (v/v)
Bromphenolblue	adjusted to color
β-Mercaptoethanol	10% (v/v)

Table 2.39: Tris/SDS, pH 6.8., 4x Adjusted to pH 6.8, stored at RT.

Compound	Concentration
Tris	500 mM
SDS	0.4 % (v/v)

Table 2.40: Tris/SDS pH8.8, 4x Adjusted to pH 8.8, stored at RT.

Compound	Concentration
Tris	1.5 M
SDS	0.4% (v/v)

Table 2.41: APS solution. Aliquots of 500 µl stored at -2°C.

Compound	Concentration
APS	10 %

Table 2.42: SDS running buffer, 10x. Adjusted to pH 8.3, stored at RT.

Compound	Concentration
Tris	250 mM
Glycine	1.9 M
SDS	1 % (v/v)

Table 2.43: Transferbuffer, 10x. Stored at RT.

Compound	Concentration
Tris	325 mM
Glycine	1.9 M

Table 2.44: Transferbuffer, 1x. Stored at 4 °C.

Compound	Concentration
Transferbuffer, 10 x	1x
Methanol	10 % (v/v)

Table 2.45: TBS buffer, 10x. Adjusted to pH 7.5, stored at RT.

Compound	Concentration
Tris	100 mM
NaCl	1.5 M

Table 2.46: TBS-Tween buffer, 1x. Stored at RT.

Compound	Concentration
TBS Buffer, 10 x	1x
Tween 20	0.1 % (v/v)

Table 2.47: Stacking gel. Volume for two 1 mm gels.

Compound	Volume
Acrylamide	500 µl
4 x Tris/SDS, pH 6.8	940 µl
H_2O	2.31 ml
APS, 10 %	18.8 µl
TEMED	7.5 µl

Table 2.48: Separating gel, 10 %. Volume for two 1 mm gels.

Compound	Volume
Acrylamide	4.0 ml
4 x Tris/SDS, pH 8.8	3.0 ml
H_2O	5.0 ml
APS, 10 %	48 µl
TEMED	18 µl

Buffers used for immunohistochemistry

Table 2.49: IHC washing buffer. Stored at RT.

Compound	Concentration
10 x TBS Buffer.	1x
Tween 20	0.05 % (v/v)

Table 2.50: IHC permeabilization buffer. Stored at RT.

Compound	Concentration
10 x TBS Buffer.	1x
Triton X-100	0.2 % (v/v)

Table 2.51: Sudan black B stock. Dissolved in ethanol (100 %), stored at RT.

Compound	Concentration
Sudan black B	1 % (m/v)

Table 2.52: Sudan black B staining solution. Dissolved in ethanol (70 %), centrifuged at 4000 g for 10 min, prepared freshly before use.

Compound	Concentration
Sudan black B stock	0.2 % (v/v)

2.1.10 Consumables

Table 2.53: Consumables

Denotation	Manufacturer, Catalogue no.
20 G Sterican	Braun, 4657519
6 Well Plate	Falcon, 351146
96 Well Plates	Thermo Fisher Scientific, 167008
Bacillol 30 Foam	Hartmann, ANY8.1
Cell culture flask T175	Greiner, 660175
Compitips advanced 5 mL	eppendorf, 0030 089.456
Cryo Tube Vials	Thermo Scientific, 363401
Dako Pen	Dako , S2002
Deckgläser 24 x 50 mm	Roth, 1871.2
Dialysis Tubing, 1 Inf Dia 8/32-6.3 mm	Medicell Int. Ltd, DTV 12000.01.000
EasyFill Cell Factory Nunclon, 2 trays	Thermo Fisher, 140250
EasyFill Cell Factory Nunclon, 4 trays	Thermo Fisher, 140360
Filterpaper	Hahnemüle, FP598
Filtropur S 0,2	Sarstedt, 83.1826.001
Gauze	Th Geyer, 9.068291
Gauze	Th Geyer, 9.068291
Gelloader Pipette Tips	Sarstedt, 70.1190.100
Kimtech	Kimberly-Clark, 7558
Laboratory film	Parafilm, PM-996
Leukosilk	BSN medical, 09567-00 AP
Luer-Lok Syringes, 20 mL	BD Plastipak, 300629
Micro-Touch	Ansell, 700124
Microcentrifuge tube	Roth, 4190.1
Microscope Cover Glasses 25 mm	Assistent, 41001125
Microscope Slides	Thermo Fisher Scientific, J1800AMNZ
MiniFlex Round Tips	Biozym, 728014
Multiply µStrip Pro 8-strip	Sarstedt, 72.991.002
Nitrocellulose Membrane, 0.45 µM	Amersham, 10600002
Nonabsorbable Braided Silk Suture	FST, 18020-50
Osmotic minipumps	ALZET, 2001D
PCR 0.1 mL 4-tube & 4-cap strips	Biozym, 711200

Table 2.53: Consumables

Denotation	Manufacturer, Catalogue no.
Petri dish	SAP, 4002291
Polyamide mesh 200 µm	Th. Geyer, 9068292
Quality Pipette Tips 1000 µL	Sarstedt, 70.762.100
SafeSeal tube 1.5 mL	Sarstedt, 72.706
Serological Pipette 10 mL	Sarstedt, 86.1254.001
Serological Pipette 2 mL	Sarstedt, 86.1252.001
Serological Pipette 25 mL	Sarstedt, 86.1255.001
Serological Pipette 5 mL	Sarstedt, 86.1253.001
Serological Pipette 50 mL	Sarstedt, 86.1256.001
Softa-Man acute	Braun, 19114
Spitzen, 10 mL	Biozym, 725064
Steritop 0.22 µm 1000 mL	Merck, SCGPT10RE
Superfrost®Plus	Thermo Sci., J1800AMNZ
Surgical scalpels, disposable	Braun, 5518083
Tip StackPack 10 µL	Sarstedt, 70.760.502
Tip StackPack 100 µL	Sarstedt, 70.760.502
Transfer pipette	Sarstedt, 86.1172.001
Tube 15mL	Sarstedt, 62.554.002
Tube 50mL	Sarstedt, 62.574.004
U-40 Insulin 30Gx1/2	Braun, 40012525
U-40 Insulin Omnifix Solo	Braun, 9161309V
UVette	Eppendorf, 9529 10051
X-ray film (Super RX)	Fujifilm, 7410 19230

2.1.11 Devices

Table 2.54: Devices.

Denotation	Manufacturer
accu-jet pro	Brand
Axiovert 200M	Zeiss
Beamsplitter DV2	Photometrix

Table 2.54: Devices.

Denotation	Manufacturer
Centrifuge Fresco 17	Thermo Scientific
Centrifuge Hareus Megafuge 8R	Thermo Scientific
Centrifuge Hareus Pico 17	Thermo Scientific
Class II Biological Safety Cabinet	Labgard
CO_2 Incubator	Sanyo
Developer SRX-101A	Konica Minolta
E-Box	Vilber Lourmat
Filter Cube 05-EM	Photometrix
FlexStation 3	Molecular Devices
Freezer Comfort	Liebherr
Fridge Comfort	Liebherr
Gene Touch	Bioer
Glacier Ultralow Temperature Freezer	Nuaire
ISM831C	Ismatec
LABOKLAV	HSP
LED KL 1600	Schott
LED pE-100 440 nm	CoolLED
Leica DMI3000 B	Leica
LX 320A scs	Precisa
MaxQ 4450	Thermo Scientific
Micro Ultracentrifuge CS150 FNX	Hitachi
Microwave	Panasonic
Mupid-One	Advance
my FUGE	Benchmark
optiMOS	Q imaging
PCB1000-2	Kern
pH Level 1	inoLab
PowerPac	Bio Rad
RCT standard	IKA
Research plus (10 µL - 10 mL)	eppendorf
RiOs™3	MilliporeSigma
Rotor Gene Q	Qiagen

Table 2.54: Devices.

Denotation	Manufacturer
Scanner LiDE 220	Canon
Shaker DRS-12	ELMI
Slidescanner Nano Zoomer 2.OHT	Hamamatsu
SMZ 745T	Nikon
Spectrophotometer DS-11	Denovix
ThermoMixer C	eppendorf
TI-1 Transilluminator	Biometra
Tube sealer STF3	Hitachi
Ultra Turrax T-10 basic	IKA
Vibramax 100	Heidolph
Vortex-Genie 2	Scientific Industries
Water Bath	Julabo
Zeiss LSM 800	Zeiss

2.1.12 Software

Table 2.55: Software.

Software	Version	Manufacturer
ApE	v2.0.49.10	Wayne Davis
CellProfiler	3.0.0	Broad Institute
Excel	14.7.4	Microsoft
Fiji	1.53e	National Institutes of Health
GraphPad Prism	6.01	Graphpad
Ilastik	1.3.0-OSX	EMBL
ImageJ	1.48v	National Institutes of Health
Inkscape	1.0.1	inkscape.org
Mendeley Desktop	1.19.4	Mendeley Ltd.
Micro-Manager	1.4.5	Open Imaging
NDP.view 2	U12388-01	Hamamatsu
nSolver	4.0	Nanostring
Overleaf	Web application	WriteLaTeX Limited

Table 2.55: Software.

Software	Version	Manufacturer
QuPath	0.2.2	QuPath
XQuartz	2.7.11	X.org foundation
ZEN (blue edition)	2.5	Carl Zeiss

2.2 Methods

2.2.1 Cloning

To study the functionality and effect of DNG on a cellular level in HEK 293 cells and isolated ARVCM we constructed pcDNA3-DNG, a plasmid used for transient transfection in HEK cells, and adenovirus expression vector pAd-CMV-V5-DNG, to produce Adv-DNG for the transduction of isolated ARVCM. For *in vivo* studies AAV vectors pds-TnT-DNG and pSSV-TnT-mCherry-2A-DNG were cloned but the first not used for further experiments in this thesis.

pds-TnT-DNG

We kindly received the DNG DNA template from Kiavash Movahedi (Vlaams Instituut voor Biotechnologie, Belgium). Initially we amplified DNG by standard high fidelity polymerase chain Reaction (PCR) using primers Ncol1-for and Not1-rev to introduce restriction enzyme cutting sites, present also in the plasmid of our destination vector pds-TnT-Fluc. The PCR reaction was performed using 100 ng DNG template and standard reaction composition as listed in Table 2.56.

Table 2.56: High fidelity PCR composition.

Components	Volume (µl)
Pfu Polymerase 10x Buffer	10
dNTP mix 10 mM each	2
Forward primer 10 pmol/µl	2.5
Revers primer 10 pmol/µl	2.5
DNA template 100-300 ng	variable
Nuclease free water	ad 100

Thermal cycling as stated in Table 2.57 and amplification time adjusted to template length of 1.2 kB with 0.5 kB amplification per minute.

PCR product was then separated by gel electrophoresis in a 1 % agarose gel supplemented with DNA stain Midori Green. 10 µl of 10x DNA gel loading buffer was added to PCR reaction mix. Samples were run along with 1 kB DNA ladder at 100 V for 30 minutes. Gels were then inspected briefly under UV-Light, the desired DNA band cut out from gel and DNA extracted using the QIAquick® Gel Extraction Kit following the manufacturers instructions and eluted in 40 µl water.

Table 2.57: PCR thermal cycling protocol.

Stage	Temperature (°C)	Time	Number of Cycles
Initial denaturation	95	5′	1x
Denaturation	95	0′30″	
Annealing	55	0′30″	30x
Amplification	72	2′30″	
Final extension	72	7′	1x
Cool down	4	∞	1x

The DNG PCR product insert and vector were both digested with the same restriction enzymes. Restriction enzymes cut double stranded DNA at specific restriction sites and produce "sticky ends" by cutting DNA with a step off leaving behind single stranded DNA overhangs. By combining insert and vector in the ligation reaction, the "sticky ends" anneal to the complementary DNA strand and fragments are re-ligated by T4 DNA ligase.

Restriction enzyme reaction components as in Table 2.58 with Ncol1 and Not1 used as restriction enzymes are incubated at 37 °C for 2 hours and digested DNA fragments separated by gel electrophoresis, extracted from gel as previously described and the vector eluted in 50 µl - the insert in 25 µl EB-Buffer.

Table 2.58: Restriction enzyme digestion.

Components	Volume (µl)
6 µg Vector OR PCR product	variable
CutSmart enzyme buffer	5
Restriction enzyme I	2.5
Restriction enzyme II	2.5
Ampuwa H_2O	ad 40

DNA fragments with sticky ends are combined in the ligation reaction as seen in Table 2.59 incubated for a minimum of 2 hours at 14 °C. Successful ligation reaction produces a intact plasmid made of vector and insert.

The plasmid was then amplified by transforming it into chemically competent Top10 *E.coli* bacteria. The plasmid harbours an ampicillin resistance gene which ensures that only bacteria containing the plasmid can proliferate in the presence of ampicillin. Transformation of the ligated plasmid in *E.coli* was achieved by adding 60 µl water and 20 µl 5-KCM Buffer to the ligation reaction. Competent Top10 *E.coli* were carefully thawed on ice and 100 µl of bacteria suspension added to the ligation reaction and gently mixed. Reaction mix was

Table 2.59: Ligation reaction.

Components	Volume (µl)
PCR product OR insert	11.5
Vector	1
10x T4 ligase buffer	1.5
T4 DNA ligase	1

kept on ice for 20 minutes and then incubated at room temperature for another 10 minutes. 1 ml LB-medium was added and incubated for 50 minutes at 37 °C at 700 rpm on a shaker. Bacteria were spun down and the reconstituted pellet spread out on LB-Plate with ampicillin (1:1000 v/v) added. Plates were incubated at 37 °C over night.

E.coli that have incorporated the plasmid proliferate on the LB-plate and form colonies, which can be clearly recognized by eye. Multiple colonies were picked and dissolved in a 15 ml falcon tube with 3 ml LB-medium with supplemented ampicillin and incubated over night on a shaker at 37 °C.

Plasmids were then extracted from *E.coli* using the QIAprep® Miniprep extraction Kit according to the manufacturers instructions and eluted in 10 µl water. The successful ligation and transformation in *E.coli* was then confirmed by control digestion. Restriction enzymes are utilized here to cut the plasmid at present cutting sites and the fragmented plasmid is then separated by gel electrophoresis. The predicted fragment size can then be compared to the sample fragments to confirm successful cloning.

8 µl of the eluted plasmid was used for control digestion as stated in Table 2.60 and incubated for 30 minutes at 37 °C. 1.5 µl DNA loading buffer was then added to the control digestion reaction, separated by gel electrophoresis and analyzed for correct band size. Undigested plasmid and digested original vector plasmid are run along the same gel to further confirm correct enzyme digestion and pasmid integrity.

Table 2.60: Plasmid control digestion.

Components	Volume (µl)
Eluted plasmid	8
CutSmart enzyme buffer	1
Restriction enzyme I	0.5
Restriction enzyme II	0.5

E.coli culture suspensions which incorporated the desired plasmid was then further amplified by adding 100 µl bacteria suspension to 50 ml LB-media with ampicillin added and

incubated over night at 37 °C with constant shaking at 200 rpm.

E.coli cultures were then centrifuged for 5 minutes at 5000 rpm at 4 °C and plasmids extracted using the QIAprep® Midiprep Kit following the manufacturers instructions. Plasmid was then eluted in 200 µl EB-Buffer.

pc-DNA3-DNG

pcDNA3-DNG was cloned by extracting the DNG insert from pds-TnT-DNG plasmid using restriction enzymes KpnI and NotI which were also used to process the original pcDNA3 vector to produce matching "sticky ends" which enables annealing and ligation of vector and insert to produce pcDNA3-DNG.

The restriction enzyme digestion reactions were carried out as stated in Table 2.58 with KpnI and NotI used as enzymes and 6 µg vector as well as 10 µg insert as input DNA. Digestion was carried out at 37 °C for 1 hour. Fragments were then separated by gel electrophoresis and correct DNA bands cut out from gel, DNA extracted and eluted from column as described in section 2.2.1.

Ligation reaction was carried out as stated in Table 2.59 whereas here, 2 µl vector and 11.5 µl insert were used. Reaction was incubated at 14 °C over night. Ligation reaction was then transformed in Top10 *E.coli* as described in section 2.2.1. Control digestion of amplified colonies with restriction enzymes KpnI and NotI. Further amplification of positive colonies as described in section 2.2.1 with ampicillin (1:1000 v/v) present in LB-medium.

AAV9 expression vector pSSV-TnT-mCherry-2A-DNG

For *in vivo* gene transfer of DNG we cloned DNG along with fluorescence protein mCherry connected via 2A into the single stranded AAV9 expression vector. 2A is a self cleaving peptide which causes ribosomal skipping leading to cleavage of polypeptides that were connected trough 2A (Luke et al., 2008). It was utilized in this thesis to cleave DNG from mCherry whereas the latter will be expressed in the cytosol and can be used as marker of successful viral transduction.

DNG and mCherry-2A was first amplified by high fidelity PCR with primers that introduce restriction enzyme cutting sites. For DNG, 240 ng of pds-TnT-DNG was used as a template with primers DNGRsrIIfor and DNGFseIrev. For mCherry-2A, 250 ng MHC-Cherry2AHydro was used as a template and primers CherryHindIIIfor and CherryRsrIIrev. PCR reaction as shown in Table 2.56 and thermal cycling shown in Table 2.57 using Pfu polymerase and amplification time of 2′24″, adjusted to template length. PCR products were then separated on a gel and DNA extracted as described in section 2.2.1. Restriction enzyme digestion was

then performed to process PCR products DNG and mCherry-2A, as well as 6 µg of the AAV9 vector pSSV-TnT-Fluc to create "sticky ends" and enable triple ligation. Restriction enzyme digestion was carried out as described in 2.58 whereas for DNG: RsrII and FseI, mCherry-2A: HindIII and RsrII and pSSV-Fluc: HindIII and FseI were used as restriction enzymes. Reaction was carried out at 37 °C for 2 hours. Digested products were subsequently separated on a gel and DNA extracted as previously described in section 2.2.1. The inserts were eluted in 25 µl and the vector eluted in 50 µl EB-buffer.

The digested inserts and vector were then annealed and ligated in a triple ligation comprised of 2 µl vector, 6 µl DNG and 4.5 µl mCherry-2A PCR products and further compiled as in Table 2.59. Ligation reaction was carried out at 14 °C over night.

Ligation reaction was then transformed in competent Top10 E. coli bacteria with ampicillin added to LB-medium and positive colonies amplified to QIAprep®Miniprep as previously described in section 2.2.1. Control digestion was carried out using RsrII FseI and HindIII. Correct colonies were then further amplified to Midiprep and eluted in 200 µl EB-Buffer. Multiple Midiprep preparations were pooled and prior to AAV production, an additional control digestion was carried out with restriction enzyme XmaI. Vector samples were stored at -20 °C until further use.

Adv-DNG expression vector pAd-CMV-V5-DNG

DNG was cloned into Adv5 expression vector using Invitrogens Gateway®technology. This system utilizes enzymes and nucleotide sequences that have been derived from bacteriophages for integration and excision of viral genes into and out of the host, in this case *E. coli*, genome. It enables quick and highly specific shuttling of DNA fragments in-between plasmids. Recombination is directed to specific *att* sites driven by clonase enzymes that catalyze the reaction in a unidirectional way. The BP-clonase catalyses the recombination of *att*B sites with *att*P sites producing *att*L and *att*R sites whereas LR-clonase catalyses the reverse reaction. With this method, a gene of interest which is flanked by *att*B sites can be inserted into an *Entry clone* at *att*P sites, catalysed by BP-clonase. The entry clone now harbours the gene of interest flanked by *att*L sites and can then be used to shuttle the inserted gene into the desired *Destination vector* where *att*R sites are present, in our case the Adv5 expression vector, catalyzed by LR-clonase. In the final *Destination vector* the gene of interest is again flanked by *att*B sites. After recombination, plasmids are transfected in competent Top10 *E. coli* for plasmid amplification. The *Entry clone* as well as the *Destination vector* harbour the *ccdB* gene flanked by *att* sites. The *ccdB* gene codes for a toxic protein that inhibits bacterial growth. When recombination is successful, *ccdB* gene is exchanged for the gene of interest,

and thus proliferation of bacteria that have incorporated the correct plasmid is not inhibited. Positive selection of *E. coli* that have incorporated the desired plasmid is further achieved by the use of antibiotics in the growth medium and antibiotic resistance as part of the plasmid vetor whereas the *Entry clone* harbours kanamycin- and the *Destination vector* ampicillin resistance genes (Reece-Hoyes and Walhout, 2018).

DNG was first amplified by standard PCR using 100 ng pcDNA3-DNG as a template and primers pcDNA3aatBfor and pcDNA3aatBrev which flank DNG and additionally introduce *att*B sites. PCR reaction composition and thermal cycling as shown in Table 2.56 and 2.57. PCR product was then separated by gel electrophoresis, DNA band cut out from gel and DNA extracted as described in section 2.2.1 and eluted in 25 µl water. BP-reaction consisted of 50 ng *att*B-PCR product, 150 ng of *Entry clone* pDONR and 2 µl BP Clonase II with TE-buffer added prior to a final volume of 10 µl. Reaction was incubation at 25 °C over night. BP-reaction was then transfected in competent *E.coli* using KCM-buffer method as described earlier in section 2.2.1 and plated on LB-plates supplemented with kanamycin and incubated at 37 °C over night. Colonies were picked and amplified in LB-medium with added kanamycin over night. Plasmid was then extracted by Miniprep preparation and eluted in 30 µl TE-Buffer as described earlier in section 2.2.1. Successful recombination was confirmed by control digestion using 500 ng plasmid DNA and EcoRI and HindIII as restriction enzymes. Restriction enzyme reaction composition as stated in Table 2.58 and fragment band analysis by gel electrophoresis as previously described in section 2.2.1.

LR-Reaction consisted of 150 ng *entry clone*, the product of previous BP-reaction, and *destination vector* pAd-CMV-V5-DEST with 2 µl LR-Clonase II in TE-Buffer to a final volume of 10 µl. Reaction was incubation at 25 °C over night. LR-Reaction was then transfected in competent *E.coli* as described earlier and plated on LB-plates with ampicillin added and incubated over night at 37 °C. Colonies were picked the next day and amplified in 50 ml LB-Medium with supplemented ampicillin. Plasmids were then extracted from bacteria by Midiprep preparation and eluted in 200 µl EB-buffer and plasmid integrity analysed by final control digestion with restriction enzyme XbaI as previously described.

In preparation for the virus production the plasmid must be linearized for transfection in HEK 293A cells. For the linearization reaction 5 µg of pAd-CMV-V5-DNG were cut using PacI with further components as listed in Table 2.58 and reaction incubated at 37 °C for one hour. DNA was then purified and extracted by ethanol precipitation:

For DNA precipitation, 70 µl of 100 % Ethanol pre-cooled to -20 °C was added to the linearization reaction followed by 10 µl of 3 M sodiumacetate at a pH value of 5.2. Reaction was incubated at -20 °C for 30 minutes and subsequently centrifuged for 10 minutes at 13.3 rpm. The supernatant was discarded and the pellet washed once with 500 µl 75 % ethanol and

centrifuged again for 5 minutes. DNA pellet was then air dried at RT and dissolved in 10 µl water. Linearized DNA was then stored at -20 °C until further use.

2.2.2 Cell culture

HEK 293A cell culture

HEK 293A cells were used for adenovirus preparation and to express FRET biosensor Epac1-camps along with DNG for initial functionality test. Cells were maintained in HEK cell culture medium and cultivated at 37 °C and 5 % CO_2. Maintenance of HEK 293A cells which comprised of cryopreservation, thawing, maintaining cell culture and providing cells for experiments, were kindly handled by Karina Schlosser.

Lipofectamine transfection

Gene transfer of foreign plasmid DNA in HEK 293A cells to initiate adenovirus production or transient gene expression for experimental purposes was achieved by Lipofectamine 2000™ transfection. Lipofectamine is a chemical transfection agent that forms complexes comprised of negatively charged nucleic acid and positively charged lipid molecules that enables transfer of nucleic acid across the mammalian lipid membrane into the nucleus (Kim and Eberwine, 2010).

HEK 293A cells were plated the day before to reach optimal confluency of 60-80 % the day of transfection. Cells were plated onto a 10 cm ∅ culture dish for adenovirus preparation or 6-well plates equipped with 25 mm ∅ round glass coverslides.

Lipofectamine transfection mix was first prepared as in Table 2.61, mixed thoroughly and incubated at RT for 20 minutes. Mixture was then dispersed evenly on cells whereas for the 6-well plates, 50 µl per well was used. Cells were then returned to the incubator until further use.

Table 2.61: Lipofectamine transfection mix.

Components	Volume (µl)
Opti-MEM®	300
Total plasmid DNA 3 µg	variable
Lipofectamine 2000®	7

Adenovirus preparation

Adenovirus Adv-DNG was prepared following standard amplification and virus purification protocols. In brief, linearized adenovirus expression vector pAd-CMV-V5-DNG was transfected in HEK 293A cells by Lipofectamine 2000™transfection as described in section 2.2.2 to initiate adenovirus amplification. At 7 to 14 days post-transfection cells were lysed and the supernatant, containing active adenovirus used to transduce the second batch of HEK 293A cells in three T175 cell culture flasks. Amplification continued to multiple EasyFill Cell tray systems to achieve significant virus-titer for subsequent virus purification.

HEK 293A cells were first lysed for virus purification in Triton-X-100/PBS solution and adenovirus precipitated from supernatant by adding 0.5 volumes of 20 % PEG 8000/2.5 M NaCl followed by centrifugation. Virus fraction was resuspended in PBS and purified by CsCl gradient ultracentrifugation. Virus band was aspirated and further concentrated by dialysis in sucrose buffer. The physical virus concentration was determined by optical densiometry ($OD_{260\,nm}$) and diluted in glycerol to a final glycerol concentration of 10 %. Virus was aliquoted and stored at -80 °C until further use. Biological virus-titer was determined by plaque essay to obtain virus plaque-forming units per ml.

Adenovirus amplification, preparation and biological virus-titer determination were kindly carried out by Karina Schlosser.

AAV preparation

AAV serotype 9 for *in vivo* application were provided by the AAV vector production unit of the O.Mueller group at the University of Heidelberg. In brief, ssAAV9-TnT-mCherry-2A-DNG and ssAAV9-TnT-mCherry were co-transfected with helper plasmid (pDP9rs providing AAV9 capsid and adenoviral genes) in HEK 293T cells for virus production. AAV were purified by filtration followed by iodixanol step gradient centrifugation and titrated by real-time quantitative PCR (rt-qPCR) (Werfel et al., 2014; Heckmann et al., 2016). AAV were aliquoted and stored at -20 °C until further use.

2.2.3 Animals used in experiments

Wistar rats were used for the isolation of ventricular cardiomyocytes and C57Bl6/J as well as C57Bl6/N mice for *in vivo* experiments. Handling of animals was done according to international animal welfare guidelines and approved by the Authority for Health and Consumer Protection BGV Hamburg (approval Nr. 47/15).

2.2.4 Adult rat ventricular cardiomyocytes isolation

Adult rat ventricular cardiomyocytes (ARVCM) were isolated from 2 months old wistar rats by collagenase digestion in a Langendorff system (Louch et al., 2011).

Rats were heparinized by intraperitoneal injection of 1000 units heparine 15 minutes before CM isolation. Sacrification by cervical dislocation under isofluorane anaesthesia followed. The thorax was disinfected with 70 % ethanol, the heart rapidly excised and transferred in ice-cold PBS. The aortic arch was visualized and cannulated with a 16 G blunted needle and fixed to the cannula using a clamp and silk rod ligation. The cannulated heart was then mounted to the Langendorff system and perfused with 1x perfusion buffer for 1 minute at 37 °C and a flow rate of 8 ml/min. Then, perfusion buffer was changed to digestion buffer. After the system was sufficiently perfused with digestion buffer, the out-flowing digestion buffer was recycled and the heart perfused for 9 minutes. 5 ml of digestion buffer was retained for subsequent mechanical CM dissociation. The ventricular tissue was cut from the mounted heart below the atrioventricular level and placed in a 10 cm ∅ petri dish containing 5 ml of digestion buffer. The tissue was then gently mechanically dissected using a scissor followed by slow aspiration and ejection of the dissolving tissue using a 10 ml pipette. The enzymatic digestion was stopped by adding 12 ml of stop buffer. Undigested tissue residues were separated from cell suspension by filtration through a 200 µm mesh. Stop buffer was added to the cell suspension to a final volume of 25 ml in a 50 ml tube. Cells were let to sediment for 8 minutes. Supernatant was removed and pellet resuspended in 25 ml of stop buffer. The sedimentation process was repeated for three times and with each repetition, stop buffer was exchanged to stop buffer with increasing calcium concentrations (final calcium concentrations: Stop I: 100 µM, Stop II: 400 µM, Stop III: 900 µM). After re-calcification cells were counted by diluting 100 µl of cell suspension 1:10 fold in STOP III buffer. Five lanes of 5 µl each were evenly spread out on a petri-dish and rod-shaped viable cardiomyocytes visualized on a cell-culture microscope and counted manually. Cell suspensions was then split and adjusted to 10.000 cells per 150 µl for plating on 25 mm ∅ round glass coverslides and 100.000 cells per 2 ml/well for western blot analysis.

2.2.5 ARVCM *in vitro* experiments

Adv-DNG MOI determination

Isolated ARVCM were plated on laminin (15 µl/well) pre-coated 6-well plates at a density of 100.000 cells per well and incubated for two hours at 37 °C and 5 % CO_2. Non-adherent cells were washed off by aspirating the plating medium and a gentle wash with 2 ml of

culture medium. 2 ml of culture medium was then added with increasing MOI of adenovirus Adv-DNG (0, 10, 30, 100, 300 and 1000). Cells were returned to the incubator at 37 °C and 5 % CO_2 for 24 hours. G_s alpha protein expression was analysed by western blot analysis as described in section 2.2.11 and section 2.2.11.

PLN-Ser^{16} phosphorylation

ARVCM were plated on laminin (15 µl/well) pre-coated 6-well plates. 100.000 cells per well were plated and incubated for two hours in the incubator at 37 °C and 5 % CO_2. After a gentle wash to remove non-adherent cells culture medium with adenovirus Adv-GFP (adenovirus control) or Adv-DNG (MOI of 300) was added. Cells were then incubated for 48 hours at 37 °C and 5 % CO_2. Prior to stimulation, cells were washed then pre-incubated with ICI 50 nm followed by stimulation with 100 nm Isoproterenol and 50 nm ICI for 15 minutes in cell culture medium at 37 °C and 5 % CO_2. Cells were then placed on ice, washed once with PBS followed by protein isolation and western blot analysis with primary antibodies used to detect phosphorylated PLN-Ser^{16} and GAPDH as described in section 2.2.11 and 2.2.11.

Induction of hypertrophy and semi-automated cell morphology measurements

ARVCM were plated in 6-well plates on laminin (5 µl/well) pre-coated 25 mm ∅ round glass coverslides. 10.000 cells per well were plated and incubated for two hours in the incubator at 37 °C and 5 % CO_2. Cells were then washed and medium replaced with culture medium supplemented with Adv-GFP (adenovirus control) and Adv-DNG (MOI 300) and returned to the incubated at 37 °C and 5 % CO_2. 24 hours post transduction cells were pre-incubated by replacing medium to stimulation medium, supplemented with 100 µM ascorbic acid and 50 nM ICI. Ascorbic acid functiones as an antioxidant to prevent isoproterenol degradation throughout the experiment. Apart from the control groups, isoproterenol was added to a final concentration of 100 nm and 10 µm. Stimulation was continued for 24 hours.

Hypertrophic changes were analyzed by microscopy of viable cells and subsequent semi-automated morphology measurements. Viable stimulated ARVCM were imaged on a Leica DMi1 phase-contrast cell culture microscope at 10x magnification. Identical illumination and filter settings were used throughout the experiments. A minimum of 20 images were acquired for each group. A workflow was utilized in this thesis using open source software, *Ilastik* and *CellProfiler*, capable of batch-processing large image data sets, to achieve user-independent fast morphology measurements of viable cardiomyocytes. *Ilastik* is a open source machine learning image segmentation and classification tool developed by the ilastik team in Anna Kreshuk's lab at the European Molecular Biology Laboratory (Berg et al., 2019).

The algorithm can be ”trained” by the use of training images whereas the user defines image features *e.g.* cells as foreground and the empty space in-between as background. The ”trained” algorithm can then be applied to a batch of images. Classified images can be exported as grayscale images for further analysis. *CellProfiler* 3.0 was subsequently used for image analysis. It is a open source tool developed by MIT´s Broad Institute's Imaging Platform (McQuin et al., 2018). Images can be analyzed by combining image processing operations as modules (*e.g.* thresholding, object identification, measurements, data analysis) to a pipeline. A pipeline can then be applied for high-content image analysis.

A subset of images from each experimental group (Phase contrast image: 2.1a) was loaded in *Ilastik* and ARVCM manually labeled as foreground against the also labeled background. With each new label, the algorithm is re-defined until satisfactory segmentation was achieved (real-time view of probability map: 2.1b). The algorithm was then applied to the complete set of batched images and classified probability map exported as *.tif* file which can be imported and processed by *CellProfiler* (grayscale image: 2.1c). *CellProfiler* 3.0 pipeline for the identification and morphological measurement of viable, rod-shaped ARVCM, comprised of the following modules:

1. *Color To Gray*: Original grayscale image was split into individual channels
2. *Identify Primary Objects*: Advanced settings were used, Global Otsu Thresholding, typical object diameter: 50 to 5000 pixel (as seen in 2.1d)
3. *Measure Object Size Shape*: Identified Objects (2.) measured
4. *Filter Objects*: Rod shaped Objects filtered (surface area: 5.000 to 50.000 (pixel arbitrary units (a.u.))^2, eccentricity: $\geqslant 0.85$, solidity: $\geqslant 0.85$) (as in Figure 2.1e)
5. *Measure Object Size Shape*: Morphological measurements of filtered objects
6. *Export To Spreadsheet*: Measurement results exported in *.csv* format
7. *Overlay Outlines*: Filtered object outlines displayed on original image
8. *Display Data on Image*: Filtered object surface area displayed on original outlined image (as in Figure 2.1f)
9. *Save Image*: Processed images saved

The parameters chosen in module *Filter Objects* are applied to the measurement results made earlier in *Measure Object Size Shape*. The limits were set empirically by analysing a

subset of training images. Surface area of 5.000 to 50.000 (pixel a.u.)^2 was set to exclude small non-ARVCM artefacts or conglomerates of ARVCM that fulfill the shape-descriptive criteria: eccentricity and solidity. Eccentricity is the ratio of the distance between the foci of an ellipse to it´s major axis length that has the same second-moments as the object analysed. The eccentricity of a circle is 0 whereas it approaches 1 for a straight line. An eccentricity of $\geqslant 0.85$ reliably excludes non-rod shaped, non-viable, ARVCM which can be appreciated in Figure 2.1d to 2.1e. Solidity is equated as the ratio of Object-Area to Convex-Hull-Area. The Convex-Hull-Area is described as, figuratively depicted, the surface of a rubber band that encloses the object´s area. Solidity approaches 1 in a perfect convex object with no outer-surface irregularities or indentations. Besides object area as cell surface area, Feret's diameter was chosen to measure ARVCM width and length. Feret's diameter is the minimum (= cell width) or maximum (= cell length) distance between to parallel lines enclosing the measured object.

Morphological measurements were normalized to control condition to account for mean difference in ARVCM population.

2.2.6 FRET microscopy

Intracellular cytsolic cAMP concentrations were measured in HEK 293A and ARVCM expressing FRET-cAMP biosensor and DNG. Cells were imaged on a Nikon eclipse Ti-4 inverted fluorescence microscope equipped with a 60x magnification oil immersion objective. Cells plated on 25 mm ∅ round glass coverslides were mounted in a microscopy chamber, washed with 400 µl of FRET-Buffer and incubated in 400 µl of FRET-Buffer for 5 minutes prior to FRET measurements. Samples were excited at λ = 440 nm with a coolLED light emitting diode, emitted light split by a beam splitter into donor (CFP λ = 480 nm) and acceptor (YFP λ = 353 nm) channels and subsequently detected on a complementary metal-oxide-semiconductor (CMOS) camera. Cells that exhibited homogeneous FRET biosensor expression were chosen for measurements. Time-laps images were acquired every 5 seconds, controlled by Micro Manager 1.4.5 software. Prior to experimental image acquisition a steady baseline was achieved by adjusting exposure time and LED-intensity. After a stable baseline was recorded, agonists, diluted in 400 µl of FRET-Buffer, were gently added whereby the identical time-intervals were adhered to in all FRET experiments.

Image analysis was performed on Micro Manager 1.4.5 software. A region of interest was drawn around individual cells and averaged fluorescence intensities of donor- and acceptor-channel respectively exported for data analysis using Excel software. FRET ratio was calculated as in equation 2.1 whereby the FRET correction factor b was incorporated to obtain

final corrected FRET ratio $\mathrm{FRET}_{\mathrm{corr}}$. FRET correction factor accounts for the spectral bleed-trough of donor fluorescence into the acceptor spectrum at the wavelength of maximum acceptor emission, where acceptor emission intensity is measured. Due to the unequal spectral distribution, bleed-trough of acceptor emission into donor spectrum is insignificant. The correction factor was determined in a separate experiment and kindly provided by Axel Kraft. Final FRET values were normalized to baseline.

$$\mathrm{FRET}_{\mathrm{corr}} = \frac{\text{averaged YFP intensity}}{\text{averaged CFP intensity}} - b \tag{2.1}$$

FRET HEK-cells

HEK 293A cells were plated on 25 mm ∅ round glass coverslides and transfected using Lipofectamine 2000™as described in section 2.2.2. The transfection reaction mix used for a 6-well plate was composed as in Table 2.61. The control group was transfected with 1.5 µg

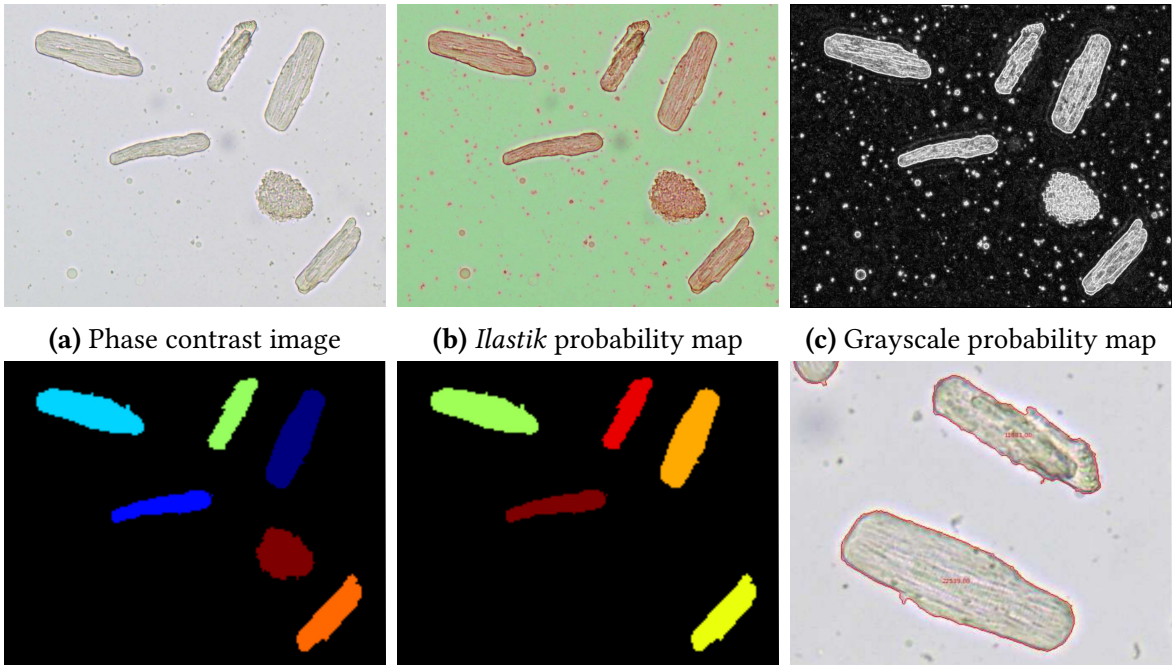

(a) Phase contrast image **(b)** *Ilastik* probability map **(c)** Grayscale probability map

(d) Identified objects **(e)** Filtered objects **(f)** Outlined cardiomyocytes

Figure 2.1: Semi-automated cell morphology measurements of viable ARVCM. Phase-contrast images at 10x magnification were acquired **(a)** and classified using trained algorithm in *Ilastik* **(d, c)** for better object identification in *CellProfiler* **(d)**. Objects (rod shaped CM) were filtered by: surface area: 5.000 to 50.000 (pixel a.u.)^2, eccentricity: $\geqslant 0.85$ and solidity: $\geqslant 0.85$ **(e)**. Original image enlarged and rotated with CM outlined. All images were enlarged for better visualization.

of pcDNA3-Epac1-camps, plasmid encoding for the cytosolic FRET-cAMP biosensor Epac1-campsNikolaev, Bünemann, Hein, et al., 2004 and 1.5 µg of empty pcDNA3 plasmid whereas in the DNG group, 1.5 µg of pcDNA3-Epac1-camps and 1.5 µg pcDNA3-DNG was used. FRET measurements were performed 24 hours post-transfection as described above.

FRET ARVCM

ARVCM were plated on 25 mm ∅ round glass coverslides and transducted as described in 2.2.5. Adenovirus encoding for FRET-cAMP biosensor Epac1-camps (Nikolaev, Bünemann, Hein, et al., 2004) (MOI 300) was transducted solely in the control group and in the DNG group, along with Adv-DNG (MOI 300). FRET measurements were performed 48 hours post-transduction as described above.

2.2.7 Mouse AAV injection and model of chronic β-AR stimulation induced cadiac hypertrophy

The functionality of ssAAV9-TnT-mCherry-2A-DNG was initially tested in two 5 weeks old C57Bl6/N mice. Cardiac function at rest and DNG effect in a model of β-AR stimulation induced cardiac hypertrophy was tested in C57Bl6/J mice. Mice at the age of 2 months were injected with either ssAAV9-TnT-mCherry (AAV control, from now on displayed in abbreviated form: AAV-mCherry) or ssAAV9-TnT-mCherry-2A-DNG (AAV-DNG) with 10^{12} vector genomes in 150 µl PBS per animal by tail vein injection. 3 weeks post AAV injection chronic 1-week β-AR stimulation was induced by isoprenaline infusion. Isoprenaline 30 µg/g/day or vehicle (saline with supplemented antioxidant ascorbic acid) as vehicle was administered by subcutaneous placement of osmotic minipumps under 1.5 % isofluorane anaesthesia. After implantation, sufficient analgesia was provided and the well-being of animals monitored on a daily basis. Overview of the experiment as shown in Figure 2.2.

AAV-injection and implantation of osmotic minipumps were kindly performed by Birgit Geertz.

2.2.8 Echocardiography

Cardiac *in vivo* phenotype was analyzed by transthoracic echocardiography using VisualSonics Vevo 3100 system and Vevolab software. Mice were anaesthetised under 1.5-2 % isoflurane and fixed supine on a heat plate. B- and M-Mode images of the short axis view were acquired to obtain fractional shortening % (FS %) and ejection fraction % (EF %), interventricular septum in diastole (IVSd) and systole (IVSs), left ventricular posterior wall in diastole (LVPWd)

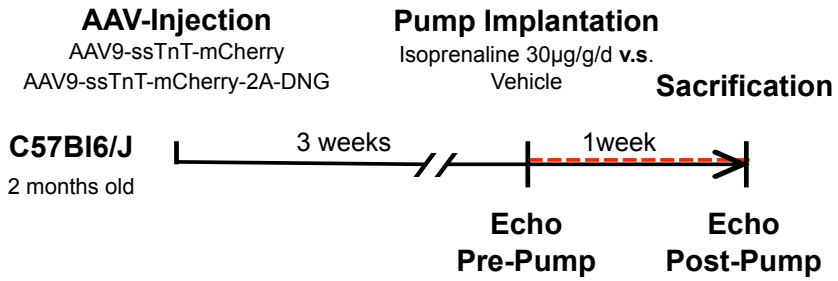

Figure 2.2: Timeline of *in vivo* AAV-injection and model of chronic β-AR stimulation induced cadiac hypertrophy.

and systole (LVPWs) and left ventricular internal diameter in diastole (LVIDd) and systole (LVIDs). Estimated LV mass was calculated according to the equation 2.2.

$$\text{Estimated LV mass} = 1.05((\text{LVIDd} + \text{LVPWd} + \text{IVSd})^3 - (\text{LVIDd})^3) \tag{2.2}$$

Echocardiography was kindly performed by Birgit Geertz and images analysed by Kirstie de Jong.

2.2.9 Mouse sacrification and tissue preparation

Mice were sacrificed by cervical dislocation under isoflurane anaesthesia. Total body weight was obtained and hearts quickly excised and placed in ice-cold PBS. The aortic trunk was visualised and mounted on a blunt 20 G cannula followd by gentle retrograde coronary perfusion with 0.5 ml of Custodiol® to arrest the heart in diastole. The heart was then weighted on a micro scale and subsequently dissected at the mid-cross sectional area. The base, used for histology, was submerged in pre-cooled 4 % Histofix®. The right ventricle of the remaining heart tissue was removed and left ventricular heart tissue cut into pinhead-sized pieces and shock-frozen in liquid nitrogen. Heart tissue was stored at -80 °C until further use. To obtain the tibia length, hind legs were removed, stripped of their skin and submerged in 10 ml of 1 M sodium hydroxide under constant shaking at RT over night. Tibias were separated from soft tissue, washed with water and dried at RT over night. Tibia length was measured using a caliper.

2.2.10 Histology

Tissue fixation and paraffin processing

Cross-sectional heart tissue was fixed in pre-cooled 4 % Histofix® at 4 °C over night and subsequently transferred to PBS and stored at 4 °C. Tissue was embedded in paraffin following standard procedures, sectioned in 3 µm slices and mounted on glass histology slides. Paraffin embedding and sectioning of heart tissue was kindly performed by the UKE mouse pathology core facility.

Immunohistochemistry and WGA staining

Tissue slides were dewaxed and hydrated as in Table 2.62.

Table 2.62: Paraffin dewaxing and hydration sequence.

Solution	Incubation Time (min)
Xylol	20
Xylol	20
Ethanol 100 %	3
Ethanol 100 %	3
Ethanol 96 %	5
Ethanol 90 %	5
Ethanol 80 %	5
Ethanol 65 %	5
Ethanol 50 %	5
Water	∞

Antigens were retrieved by boiling the hydrated slides in citrate buffer for 15 minutes using a microwave at 200 W. Slides were then washed three times in TBST and permeabilized in TBS-Triton X-100 0.2 % for 15 minutes. After washing in TBST tissue sections were circled with water repellent Dako pen. 40 µl of antibodydiulent supplemented with 5 % donkey serum was used to block unspecific antibody binding sites prior to antibody staining. Primary antibody mCherry 1:750 in antibody diulent was incubated over night at 4 °C in a moistened staining chamber. Slides were then washed extensively three times for 30 min each in TBST and incubated with secondary antibody 1:500 at RT. After fluorophores have been added to the staining protocol, all following steps were performed in the dark. Slides were then again washed extensively and 40 µl wheat germ agglutinin (WGA) was added onto the slides for 30 minutes. Following another washing step slides were emerged in freshly prepared 0.2 %

sudan black B in 70 % ethanol to quench tissue auto-fluorescence for 30 min Sun et al., 2011. The slides were washed extensively again in TBST and TBS as the last washing step and mounted in Fluoromount G plus DAPI. Stained slides were stored at 4 °C and imaged soon after.

Fluorescence microscopy and cardiomyocyte cross-sectional area determination

Whole slide fluorescence histology images were obtained on the Axio Scan.Z1 system at UKE anatomy department.

The AAV-transduction efficiency was determined in IHC cross-sectional heart sections stained as described above by manually counting the number of positive (mCherry stained red cells) and negative cells in 4 exported region of interests of 495 x 430 µm from random mid-ventricular areas taken from 4 animals 4 weeks after systemic injection of ssAAV9-TnT-mCherry or ssAAV9-TnT-mCherry-2A-DNG using cell counter makro on *ImageJ*.

Images for cardiomyocyte measurements were captured on a ApoTome system (Zeiss) using Axiovision 4.8.2 software at 20x magnification. Automatic exposure mode was chosen and 10 images around the inner left-ventricular circumference were acquired and exported as *.tif* files. A similar workflow as described in section 2.2.5 was established to enable semi-automated cariomyocyte cross-sectional area measurement using *Ilastik* and *CellProfiler* software. A subset of WGA channel training images was first imported to *Ilastik* and WGA stained cell boundaries labeled as foreground. The trained *Ilastik* classification algorithm was then applied to the complete batch of images and classified probability map, as in Figure 2.3a, exported as *.tif* file.

CellProfiler pipeline for the measurement of cross-sectional cardiomyocyte area was composed of the following modules:

1. *Color To Gray*: Original grayscale image was split into individual channels
2. *Identify Primary Objects*: Advanced settings were used, Global Otsu Threshold, typical object diameter: 20 to 200 pixel units, no declumping (as in Figure 2.3b)
3. *Measure Object Size Shape*: Identified Objects (2.) measured
4. *Filter Objects*: Round CM filtered by: eccentricity: $\leqslant 0.7$, form factor: $\geqslant 0.4$, solidity: $\geqslant 0.85$, Min. Feret's Diameter: $\geqslant 35$ pixel units (filtered objects as in Figure 2.3b)
5. *Measure Object Size Shape*: Morphological measurements of filtered objects
6. *Export To Spreadsheet*: Measurement results exported in *.csv* format

7. *Overlay Outlines*: Filtered object outlines displayed on original image (as in Figure 2.3d)

8. *Save Image*: Processed images saved

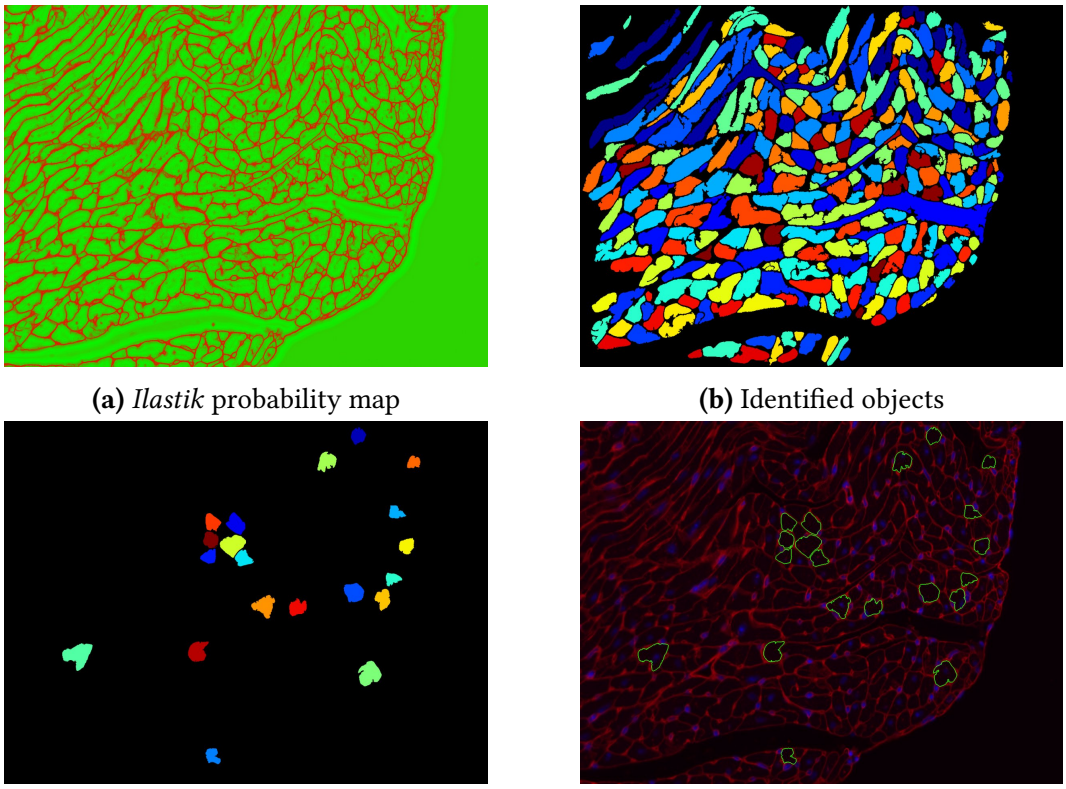

(a) *Ilastik* probability map

(b) Identified objects

(c) Filtered objects

(d) Original Image CM Outlined

Figure 2.3: Semi-automated CM cross-sectional area measurements in WGA stained heart histology sections. WGA images were acquired at 20x magnification and classified using trained algorithm in *Ilastik* **(a)** for better object identification in *CellProfiler* **(b)**. Objects were filtered by: eccentricity: $\leqslant 0.7$, form factor: $\geqslant 0.4$, solidity: $\geqslant 0.85$, Min. Feret's Diameter: $\geqslant 35$ pixel units **(c)**. Original image (WGA red, DAPI blue) with filtered CM outlined in green **(d)**.

Interstitial fibrosis measurement

Fibrosis was determined in formalin fixed and paraffin embedded Picrosirius-red stained cross-sectional heart sections. The staining was performed in batch to reduce staining variance using standard picrosirius red (PSR) protocol. Whole slide images were obtained on the NanoZoomer 2.0-HT system and images further processed using Hamamatsu NDP.view2

software. PSR staining and imaging was kindly performed by Kirstin Harmann at the UKE mouse pathology facility.

For each animal, 20 images at 20x magnification of ventricular areas excluding noticeable vessels were exported in *.tiff* file format. Images were loaded in *CellProfiler* for further processing. The following pipeline was used:

1. *Color To Gray*: Original grayscale image was split into individual channels
2. *Image Math*: Original gray image inverted
3. *Threshold*: Manual threshold of 0.125 was applied to image (2.) for total tissue area
4. *Unmix Colors*: Custom absorbance settings were adapted from *Fiji* MRI fibrosis tool macro which is based on the colour deconvolution plugin from Gabriel Landini to separate PSR staining (Red: 0.148, Green: 0.772, Blue: 0.618)
5. *Mask Image*: PSR separated image from (4.) was masked using total tissue area as mask
6. *Threshold*: Manual threshold of 0.15 was applied to masked PSR separated image to give fibrosis area
7. *Measure Image Area Occupied*: Area of total tissue and fibrosis measured
8. *Export To Spreadsheet*: Measurement results exported in *.csv* format
9. *Save Image*: Processed images saved

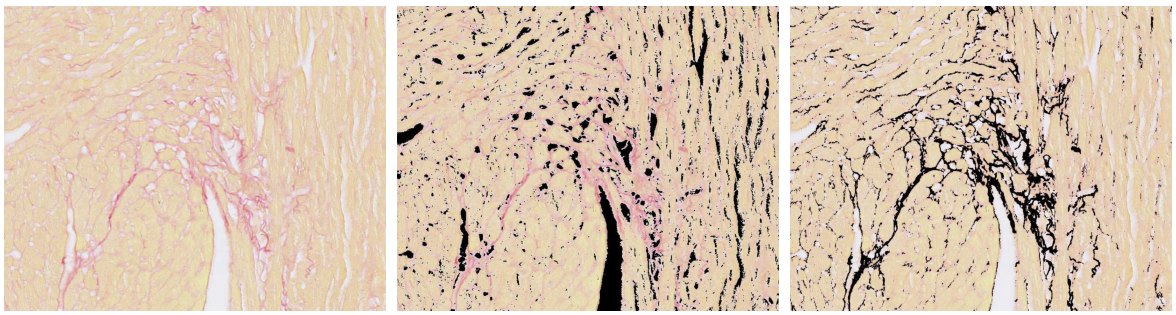

(a) PSR original image **(b)** Background area **(c)** Fibrosis area

Figure 2.4: Area of fibrosis measurement. Whole slide images from picrosirius red stained heart sections were exported at 20x magnification **(a)** and batch processed in *CellProfiler*. Ratio of masked total tissue area **(b)** and fibrosis area **(c)** (in black) was calculated.

2.2.11 Western blot

Protein preparation from cells

Adult rat ventricular cardiomyocytes were cultured on laminin coated 6-well plates at a density of 100.000 cells/well. Prior to lysis, cells were washed on ice with 2 ml ice-cold PBS and scraped off in 80 µl Lysis Buffer. Cells were then disrupted by aspirating and ejecting multiple times trough a 30 G Insulin syringe. Lysates were then incubated on ice for 15 minutes and centrifuged for 5 minutes at 8000 rpm on a cooled table top cetrifuge (4 °C. Protein concentration was determined using bicinchoninic acid (BCA) protein assay following the manufacturers instructions.

Protein preparation from heart tissue

Blood free snap frozen heart tissue samples were homogenized in 300 µl Lysis Buffer using a tissue homogenizer. Samples were then centrifuged for 5 minutes at 8000 rpm on a cooled table top cetrifuge. Protein concentration was determined using BCA Protein Assay.

Western blot analysis

Protein lysates were diluted in Lysis Buffer containing SDS Stop 3x Buffer to a protein-concentration of 1 µg/µl and boiled at 95 °C for 5 minutes. Sodium dodecyl sulfate polyacrylamide gel electrophoresis (SDS-PAGE) (LAEMMLI, 1970) was used to separate the protein samples by their molecular size in 8-10 % acrylamide gels and subsequently transferred onto nitrocellulose membrane. Successful protein transfer was visually examined by brief Coomassie staining. Membranes were then blocked with 5 % milk powder in TBS-T except for the detection of calsequestrin where 3 % bovine serum albumin in TBS-T was used and incubated for one hour. Primary antibodies were diluted as stated in Table 2.7, added and incubated at 4 °C over night. Membranes were washed trice in TBS-T and secondary horseradish peroxidase linked antibodies added and incubated for 1 hour as stated in Table 2.8. Membranes were washed again and protein bands visualized by signal detection on X-ray films using SuperSignal™West Pico PLUS kit. X-ray films were developed in a film processor, scanned and protein quantification assessed by densiometric band analysis in relation to loading control using western blot plugin in *Fiji*.

2.2.12 RNA expression analysis

RNA isolation

To minimize ribonucleic acid (RNA) degradation snap frozen heart tissue samples were transferred to 200 µl -80 °C pre-cooled RNAlater®-ICE and incubated first at -80 °C and placed in -20 °C over night prior to RNA isolation. Tissue was then homogenized in 300 µl RLT lysis buffer with β-mercaptoethanol added using a homogenizer and RNA isolated according to the RNEasy®Fibrous tissue kit instructions. RNA concentration and purity was analyzed by NanoDrop spectrophotometer. RNA was stored at -80 °C until further use.

Quantitative real time PCR

Quantitative real time PCR is a widely used method for gene expression analysis. SYBR®green rt-qPCR and $2^{-\Delta C_t}$ data analysis was used to analyze the expression levels of DNG and endogenous Gα_s normalized to glyceraldehyde 3-phosphate dehydrogenase (GAPDH) as housekeeping gene.

In brief, RNA is first transcribed by reverse transcriptase to complementary DNA. Specific primers are used to amplify short (70-150 bp) nucleotide sequences. With each amplification cycle, assuming ideal reaction conditions, the amount of DNA doubles. SYBR®green, present in the PCR reaction, is a dye that intercalates in-between double-stranded DNA whereupon the fluorescence characteristics change resulting in an increase of emission intensity. During the optimal cycling period, the measured emission intensity doubles with each PCR cycle. Depending on the initial amount of target template, the exponential phase is reached at different PCR cycles. By setting a threshold emission intensity, each sample analysed surpasses the threshold at a different cycle. Depending on the initial amount of target template present, the cycle threshold (ct)-value differs (Ponchel et al., 2003).

Relative gene expression is achieved by comparing ct-values of a gene of interest to a housekeeping gene using the $2^{-\Delta C_t}$ method (Livak and Schmittgen, 2001).

Complementary DNA synthesis

RNA was thawed from -80 °C on ice and RNA concentration repeatedly measured by spectrophotometry. RNA was diluted with ribonuclease (RNase) free water to a concentration of 100 ng/µl. Complementary DNA was synthesised from 200 ng RNA using the iScript™cDNA synthesis kit as shown in Table 2.63.

The cDNA synthesis reaction was carried out in a thermal cycler following the protocol as in Table 2.64. cDNA was stored at -20 °C until further use.

Table 2.63: iScript™cDNA synthesis mix.

Components	Volume (µl)
RNA template 200 ng	variable
RNase free H_2O	ad 20
5 x iScript™reaction mix	4
iScript™reverse transcriptase	1

Table 2.64: iScript™cDNA synthesis thermal cycling protocol.

Stage	Temperature (°C)	Time
Priming	25	5′
Reverse transcription	42	30′
Reverse transcriptase inactivation	85	5′
Cool down hold	4	∞

Rt-qPCR primer design and testing

The GAPDH primers were kindly provided by Alexander Froese. The remaining rt-qPCR primers were designed as advised in (Bustin and Huggett, 2017; Thornton and Basu, 2011) which includes extensive *in silico* testing to ensure primer specificity and exclude primer or amplicon secondary structures that could impair essay efficiency prior to "wet lab" implementation.

Primers to specifically detect *DNG* were designed in *Primer3plus* with parameters set to the qPCR default settings (optimal primer size: 20 bp, melting temperature: 60 °C and GC-content: 50 %) and forced the primer 3'-end to be positioned over a DNG nucleotide G/C mutation. Gα_s specific primers were designed using NCBI *primer-BLAST*®tool with primer settings set to meet the criteria as mentioned above with amplicon size between 50-150 bp and additionally, primers must span exon-exon junction. A target region was defined on the complex locus of *mus musculus GNAS* to include the majority of splice variants which included: transcript variants 1, 3, 5, 7, 8 and 9. Primer *in silico* specificity was analysed using *primer-BLAST*®and *MFE-Primer*$^{3.1}$®. Formation of primer hairpins, homo- and hetero-dimers was excluded in *OligoAnalizer* tool from IDT™. Secondary amplicon structure formation was analyzed using *Mfold* tool from The RNA Institute. Simulation conditions were adapted to SYBR®-green assay conditions with sodium concentration set to 50 mM and magnesium to 3 mM at 60 °C.

Primers were "wet lab" tested by performing SYBR®-green rt-qPCR with primer concentrantions ranging from 0.2 µM to 1 µM on a pooled cDNA mix from DNG (+/-) samples. qPCR

product was also separated on a 2 % agarose gel in TAE-buffer supplemented with Midori green along with 100 bp DNA-ladder. Gel was run at 100 V for 30 minutes and visualized under UV-light. Primer pairs with good essay stability trough different primer concentrations, a single peaked melting curve and a single DNA band at the predicted amplicon size were chosen for experiments.

Rt-qPCR analysis

Rt-qPCR analysis was performed on the thermal cycler Rotor-Gene®Q system and reaction carried out in 0.1 ml tubes loaded on a 72-well rotor. The SYBR®-green rt-qPCR reaction composition as described in Table 2.65. All samples were run in triplicates and for each probe analysed, a negative control (Ampuwa H_2O) was run along with a posive control (+DNG cDNA mix).

Table 2.65: SYBR®-green rt-qPCR master mix. Final primer concentration of 500 nM.

Components	Volume (µl)
SYBR®-green	5
Primer mix (for.+rev.)	1
cDNA (1:3 dilution)	1
Ampuwa H_2O	3
Total Volume	10

Thermal cycling as in Table 2.66. Gain optimization was performed before first acquisition.

Table 2.66: rt-qPCR thermal cycling protocol

Stage	Temperature (°C)	Time	Number of Cycles
Initial denaturation	95	10′	1x
Denaturation	95	0′10″	
Annealing	60	0′15″	39x
Amplification	72	0′20″	
Melting curve 0.5 °C steps	72-95		1x

The Rotor-Gene®Q software was used for rt-qPCR data analysis with the threshold set at the exponential phase. Exported ct-values were then further analysed using the $2^{-\Delta C_t}$ method (Livak and Schmittgen, 2001) and expressed as relative expression to housekeeping gene *GAPDH* as follows:

$$\Delta C_t = C_t(\text{target gene}) - C_t(\text{housekeeping gene}) \tag{2.3}$$

$$\text{Ratio} = 2^{\Delta C_t} \tag{2.4}$$

$$\text{Gene expression (\% housekeeping gene)} = 100 \cdot \frac{1}{2^{\Delta C_t}} \tag{2.5}$$

Nanostring

Expression levels of genes related to hypertrophy were analyzed with the NanoString® Elements technology. NanoString® nCounter® is a novel probe-based expression analysis system that enables direct quantification of mRNA gene copy numbers in isolated RNA. It utilizes nucleotide probes that have a molecular fluorescence *barcode* attached which bind to RNA samples and can subsequently be directly quantified. Multiple genes, merged in a panel, can be analyzed simultaneously and normalized to numerous housekeeping genes. The customized hypertrophy panel included target- and housekeeping genes as listed in Table 2.6. Nanostring analysis was carried out at the Nanostring Facility as part of the institute of Experimental Pharmacology and Toxicology at the UKE.

2.2.13 Statistics

Statistical analysis was carried out with *GraphPad Prism* software. A minimum of 3 biological replicates per group were used for *in vitro*, whereas 6 replicates were used for *in vivo* experiments. Data is presented as mean values $\pm$ standard error of the mean (SEM). Normal distribution of data was assumed for *in vitro* experiments and evaluated using the Kolmogorov-Smirnov test in the *in vivo* experiments. Statistical significance was analysed by two-sided unpaired student's t-test and two-way ANOVA followed by Tukey's post-hoc test as appropriate. Nonparametric Kruskal-Wallis test followed by Dunn's multiple comparison test was used in experiments in which samples failed normality test. A p-value of < 0.05 was considered as statistically significant. One animal was excluded from grouped analysis which will be discussed separately.

3 Results

This chapter presents the following results: (i) DNG functionality to block signal transmission from the Gα_s coupled β-ARs in HEK293A cells. (ii) Successful *in vitro* adenoviral gene transfer of DNG in ARVCM and functionality to block β-AR stimulation induced cAMP formation and reduced downstream signaling. (iii) DNG inhibition of hypertrophic growth of ARVCM to chronic β_1-AR stimulation. (iv) Successful *in vivo* gene transfer of DNG to the murine heart. (v) DNG *in vivo* effect on cardiac function at rest and in a model of chronic β_1-AR stimulation induced cardiac hypertrophy.

3.1 DNG functionality in HEK cells

The functionality of DNG was first analyzed by stimulation of β-AR and measuring cytosolic cAMP response by FRET cAMP analysis in HEK cells. Specific FRET cAMP biosensor Epac1-camps (Nikolaev, Bünemann, Hein, et al., 2004) was expressed along with DNG in HEK cells. β-AR receptors were stimulated with 100 nM of the non-selective β-AR agonist isoproterenol (ISO). Maximum cAMP accumulation was achieved by broad inhibition of PDEs with 100 µM 3-isobutyl-1-methylxanthine (IBMX) and unspecific AC activation with 10 µM Forskolin. cAMP increase in response to β-AR stimulation induces a reduction in FRET-ratio whereas the maximum cAMP accumulation induces the maximum FRET response. In the control cells, 100 nM ISO resulted in a cAMP reaction of 91 ± 1.5 % of maximum FRET. The FRET response to ISO was reduced to 18 ± 2.9 % of maximum FRET in DNG expressing HEK cells. cAMP response to 100 nM ISO related to maximum FRET was significantly reduced by approximately 80 % in DNG expressing HEK cells, compared to non-DNG transfected control cells, as shown in Figure 3.1. Thus, confirming DNG functionality in HEK cells by significantly reducing the cytosolic cAMP increase in response to non-selective β-AR stimulation.

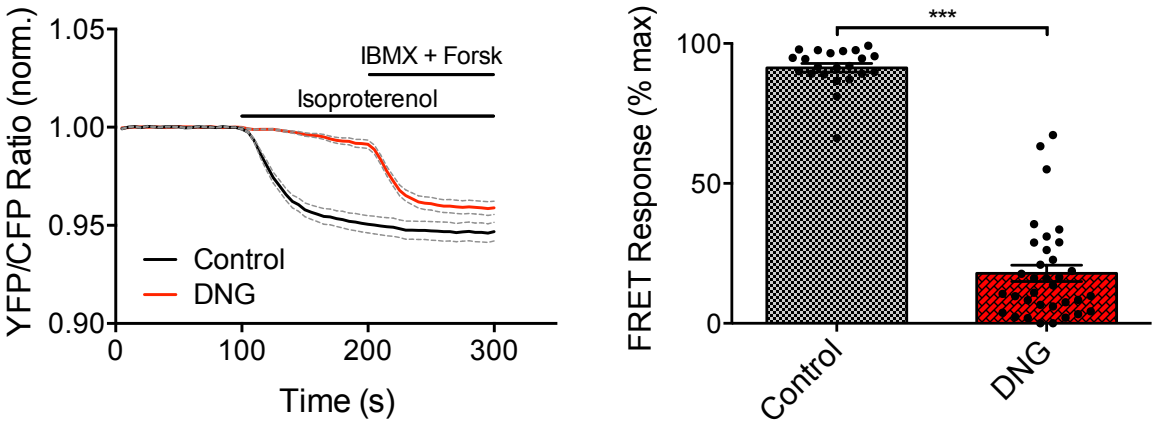

Figure 3.1: FRET cAMP response to β-adrenergic stimulation in HEK cells expressing DNG. Left, mean FRET traces over time (23/3 for control, 34/3 for DNG) recorded in HEK cells transiently transfected for 24 hours with plasmid Epac1-camps solely in the control group and additionally with plasmid pc-DNA3-DNG in DNG group, stimulated with 100 nM isoproterenol (ISO), followed by 100 µM IBMX and 10 µM forskolin. Dotted gray lines are error bars in $\pm$ SEM. **Right,** corresponding quantification of FRET cAMP ISO response related to maximum FRET represented as mean $\pm$ SEM. Significance was tested by unpaired Student's t-test. $\star\star\star$ is p-value of < 0.001.

3.2 DNG expression and functionality in ARVCM

To explore the functionality of DNG in ARVCM, adenovirus Adv-DNG was produced by cloning DNG sequence into the Adv-5 backbone harboring cytomegalovirus (CMV) promoter using Gateway® technology. First, it was necessary to determine the appropriate multiplicity of infection (MOI) for the transduction of ARVCM with Adv-DNG. Functionality was then tested by measuring FRET cAMP response and cAMP dependent phosphorylation of downstream target of PKA to β-AR stimulation.

3.2.1 DNG expression and MOI determination

The adequate adenovirus concentration used for transduction was first determined by transduction of ARVCM with increasing MOI of Adv-DNG. DNG protein expression was analyzed after 24 hours of virus incubation by western blot using antibody, to detect Gα_s, which is also specific to Gα_s mutant DNG, as shown in Figure 3.2.

The two Gα_s isoforms can be identified in the control non-Adv exposed ARVCM: Gα_s-small (45 kDa), which is the predominant isoform in ARVCM, and the faint band of Gα_s-large

(52 kDa). In the Adv-DNG exposed ARVCM an additional protein band slightly larger than the Gα_s-large protein band could be distinguished. Most stable DNG expression was reached at an MOI of 300 and was therefore chosen for subsequent experiments.

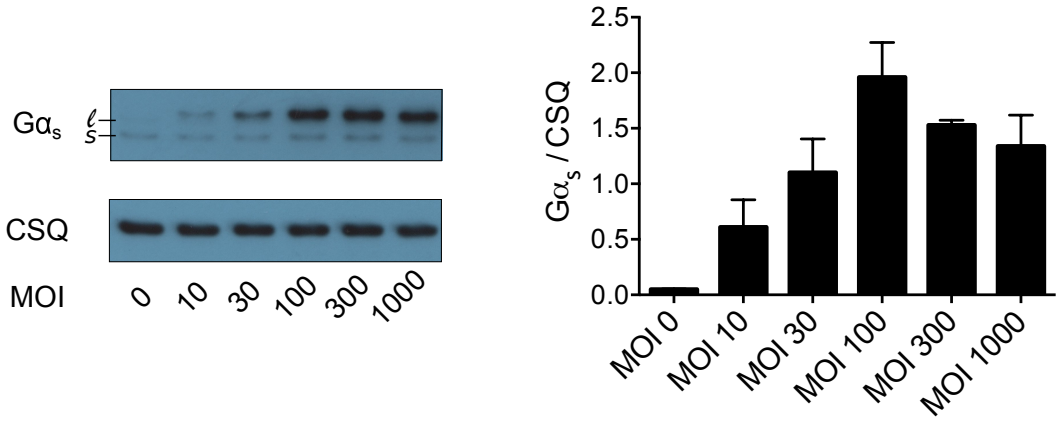

Figure 3.2: Western blot analysis of DNG expression in ARVCM transducted with increasing MOI of Adv-DNG. Left, Representative WB of ARVCM lysates (5 µg protein/lane) transducted with increasing MOI of Adv-DNG for 24 h and probed with Gα_s specific antibody to detect the short 45 kDa and large 52 kDa isoform which also detects DNG and calsequestrin (CSQ) as loading control. **Right,** corresponding quantification of the large 52 kDa Gα_s isoform protein band including DNG relative to CSQ. Data of 3 biological replicates per group are shown as mean ± SEM.

3.2.2 DNG functionality in ARVCM

cAMP FRET measurements

The inhibitory property of DNG on Gα_s signaling in cardiomyocytes was analyzed by FRET cAMP measurements in Adv-DNG transducted ARVCM. Isolated ARVCM were tranducted with Adv-DNG along with adenovirus encoding for cytolsolic FRET cAMP biosensor Epac1-camps (Bastug-Özel et al., 2019). Stimulation of β-AR with 100 nM ISO resulted in a FRET response of 43.23 ± 2.4 % to maximum FRET induced by broad inhibition of PDEs with 100 µM IBMX and unspecific AC activation with 10 µM Forskolin in non-DNG transducted ARVCM. In DNG expressing ARVCM the FRET response to 100 nM ISO was 9.4 ± 0.96 % related to maximum FRET. DNG significantly reduced FRET response to 100 nM related to maximum FRET by approximately 78 % compared to non-DNG expressing control ARVCM as shown in Figure 3.3.

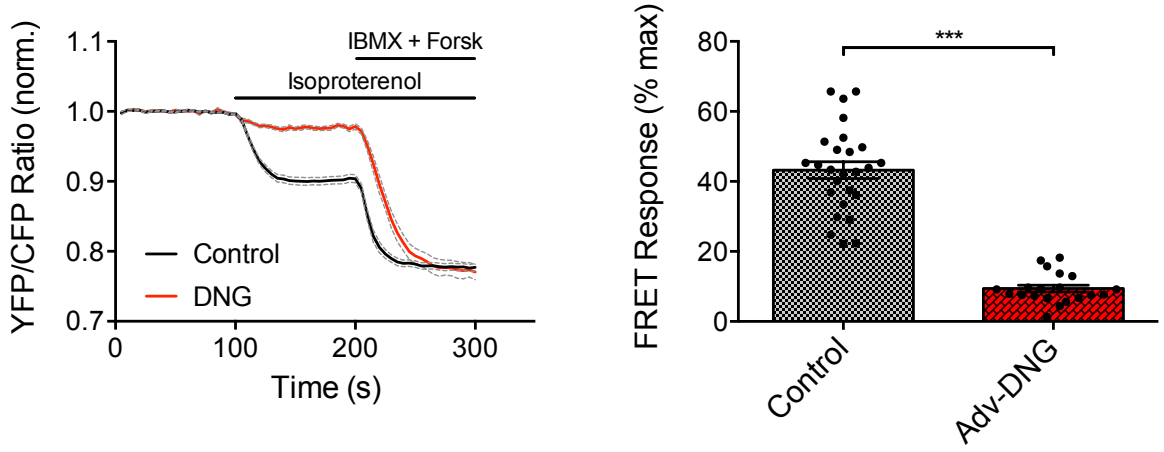

Figure 3.3: FRET cAMP response to β-adrenergic stimulation in ARVCM expressing DNG. Left, mean FRET traces over time (27/3 cell for control, 20/3 for Adv-DNG) recorded in ARVCM transducted for 24 hours with cytosolic FRET cAMP sensor Adv-E1-camps (MOI 300) and additionally with Adv-DNG (MOI 300) in the DNG group, stimulated with 100 nM isoproterenol (ISO), followed by 100 µM IBMX and 10 µM forskolin. Dotted gray lines are error bars in $\pm$ SEM. **Right,** corresponding quantification of FRET cAMP ISO response related to maximum FRET represented as mean $\pm$ SEM. Significance was tested by unpaired Student's t-test. $\star\star\star$ is p-value of < 0.001.

ARVCM PLN-Ser^{16} phosphorylation

To further substantiate the inhibitory effect of DNG on Gα_s signaling in cardiomyocytes we investigated the phosphorylation state of PLN at the Ser^{16} residue, which is a cAMP dependent downstream substrate of PKA, in ARVCM expressing DNG upon β-AR stimulation. Stimulation with 100 nM ISO for 15 minutes resulted in significant phosphorylation of PLN-Ser^{16} normalized to GAPDH in ARVCM transducted with Adv-GFP as adenovirus control as shown in Figure 3.4. In ARVCM expressing DNG, PLN Ser^{16} phosphorylation was significantly reduced by approximately 64 % compared to ISO stimulated control group.

ARVCM hypertrophic growth in response to chronic β_1-AR stimulation

Chronic β_1-AR stimulation induces hypertrophic growth in ARVCM. To investigate the inhibitory effect of DNG on the development of β_1-AR induced hypertrophic growth in ARVCM we exposed ARVCM transducted with Adv-DNG and Adv-GFP as adenovirus control 24 hours post-transduction to 100 nM and 10 µM isoproterenol in the presence of 50 nM of the β_2-AR antagonist ICI-118,551 (ICI) for 24 hours as shown in Figure 3.5. Cell morphology was subsequently measured by semi-automated image analysis on viable ARVCM and

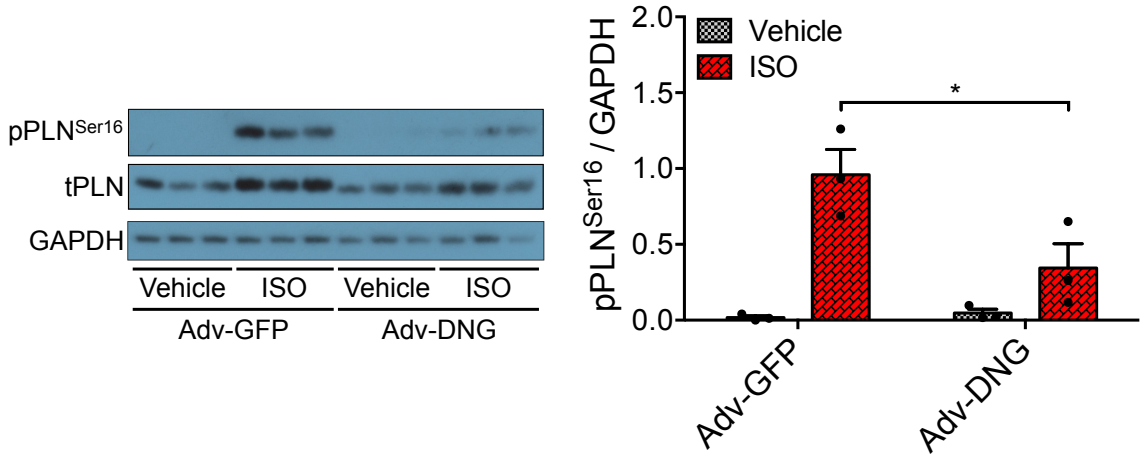

Figure 3.4: Western blot analysis of cAMP regulated PKA dependent PLN-Ser^{16} phosphorylation to β-adrenergic stimulation in ARVCM expressing DNG. Left, Western blot of phosphorylated PLN-Ser^{16}, total PLN and GAPDH as loading control from ARVCM lysates (20 µg protein/lane) transducted for 24 h with Adv-GFP as adenovirus control and Adv-DNG (MOI 300), stimulated with 100 nM isoproterenol (ISO) for 15 minutes. **Right,** corresponding quantification of PLN-Ser^{16} phosphorylation normalized to GAPDH. Data of 3 biological replicates per group are shown as mean ± SEM. Significance was analyzed by two-way ANOVA following Tukey's post-hoc test. ⋆ is p-value of < 0.05.

morphometric parameters shown as percent change to the respective control condition.

The morphometric parameters in the control conditions were similar in-between the Adv-GFP and Adv-DNG transducted ARVCM. The cell surface are was 14517 ± 322.0 a.u. and 14433 ± 281.8 a.u., the cell width 69.91 ± 1.2 a.u. and 69.01 ± 1.7 a.u. and cell length 277.4 ± 2.2 a.u. and 279.0 ± 2.9 a.u., respectively, for Adv-GFP and Adv-DNG at the control condition. An increase in cell surface area, cell width and cell length was observed in the control group at 100 nM and 10 µM ISO, respectively. The increase in cell size was most prominent in cell surface area followed by cell width, less pronounced in cell length. Cell surface area increased statistically significant in non-DNG expressing ARVCM in response to 100 nM ISO by 5.9 ± 0.53 % and to 10 µM ISO by 7.3 ± 0.76 % whereas the increase in DNG transducted ARVCM was insignificant at 2.7 ± 1.3 % to 100 nM ISO and 2.1 ± 1.3 % to 10 µM ISO. The increase in cell surface area to 10 µM ISO was significantly reduced in the DNG expressing ARVCM. Cell width also increased significantly in the non-DNG expressing ARVCM whereas here, no significant difference in cell width at 100 nM or 10 µM ISO to DNG expressing ARVCM was observed.

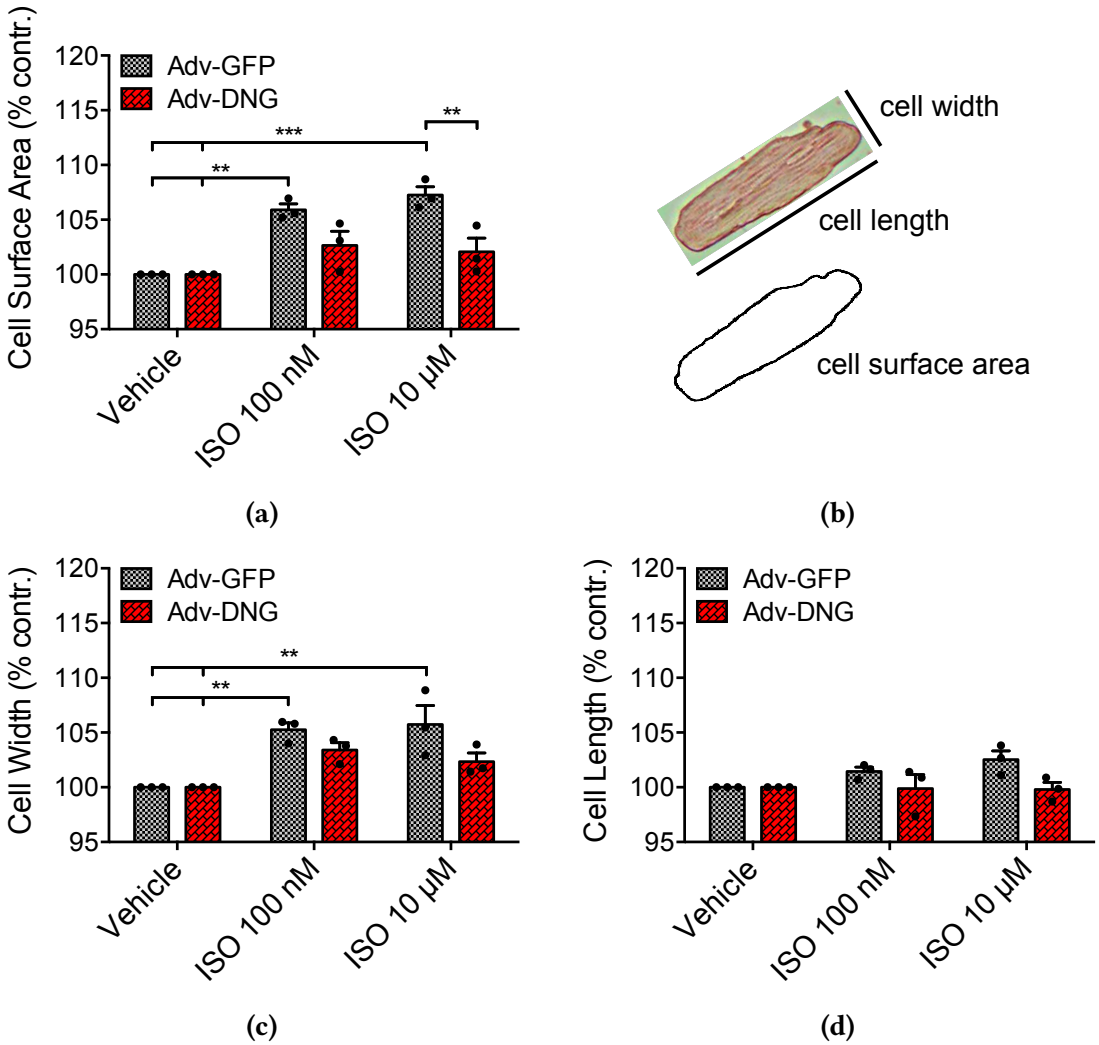

Figure 3.5: Morphometric changes of ARVCM expressing DNG to chronic β_1-adrenergic stimulation. ARVCM were transducted for 24 hours with Adv-GFP as adenovirus control or Adv-DNG (MOI 300) and subsequently stimulated for 24 hours at basal conditions or stimulated with 100 nM and 10 µM isoproterenol (ISO) respectively. 50 nM of the β_2-AR antagonist ICI-118,551 (ICI) and 100 µM ascorbic acid was present in all groups during stimulation. Images were taken from viable cells and analyzed by semi-automated cell morphology measurements using open-source software *Ilastik* and *CellProfiler* as described in Section 2.2.5. Data is mean change in cell surface area **(a)**, cell width **(c)** and cell length **(d)** normalized to basal conditions $\pm$ SEM. Data of 3 biological replicates, number of cells per group: min: 341, max: 745, mean: 493. Significance was analyzed by two-way ANOVA following Tukey's post-hoc test. $\star$ is p-value of < 0.05, $\star\star$ is p-value of < 0.01, $\star\star\star$ is p-value of < 0.001. Schematic depiction of morphometric parameters cell width (Feret Min), cell length (Feret Max) and cell surface area **(b)**.

3.3 AAV DNG *in vivo* gene transfer and model of β-AR stimulation driven cardiac hypertrophy

After promising *in vitro* results were obtained *in vivo* expression by AAV serotype 9 gene transfer of DNG was pursued. Successful AAV functionality was initially confirmed by transgene expression analysis in two ssAAV9-TnT-mCherry-2A-DNG injected mice and the *in vivo* effect assessed in a prospective cohort study to investigate the impact on cardiac function at baseline and in a model of β-AR stimulation driven cardiac hypertrophy.

Single stranded AAV serotype 9 was used for *in vivo* gene transfer of DNG. Cardiomyocyte specific expression was achieved by harboring cardiomyocyte-specific troponin T (TnT) promoter. Reporter fluorescence protein mCherry was attached to DNG via the 2A sequence, resulting in post-transcriptional cleavage of DNG and cytosolic mCherry expression. A section of ssAAV9-TnT-mCherry-2A-DNG vector map is illustrated in Figure 3.6. Identical virus backbone and promoter sequence encoding solely for mCherry were used as AAV transduction control (ssAAV9-TnT-mCherry).

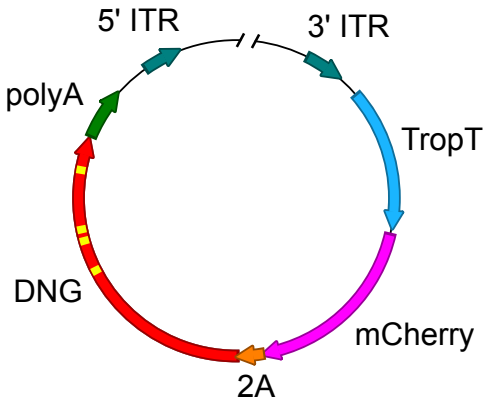

Figure 3.6: pSSV9-TnT-mCherry-2A-DNG vector map. Illustration of vector map section of single stranded AAV serotype 9 with 5'- and 3'ITR (inverted terminal repeat), human troponin T promoter (TropT), fluorescence protein mCherry, 2A self cleaving peptide, DNG with mutations highlighted in yellow and polyadenylation tail (polyA).

3.3.1 Initial transgene expression analysis in AAV-DNG injected mice

The AAV ssAAV9-TnT-mCherry-2A-DNG was initially tested in two 5 weeks old C57BL6/N mice by tail vein injection of 10^{12} vg/animal. The expression of DNG was subsequently analysed 6 weeks later in cross-sectional cardiac tissue by immunohistochemistry (IHC) probing

for mCherry and western blot using antibody to detect Gα_s, which is also specific to Gα_s mutant DNG and antibody to detect mCherry as shown in Figure 3.7. No-AAV injected mice were used as control.

Strong even mCherry expression was present in cross-sectional heart sections with almost all of CM exhibiting a degree of increased mCherry fluorescence compared to no-AAV injected IHC stained control sections. The protein expression of Gα_s/DNG was markedly increased in AAV-DNG injected animals, compared to no-AAV injected control, as well as the expression of mCherry, which was not present in the latter.

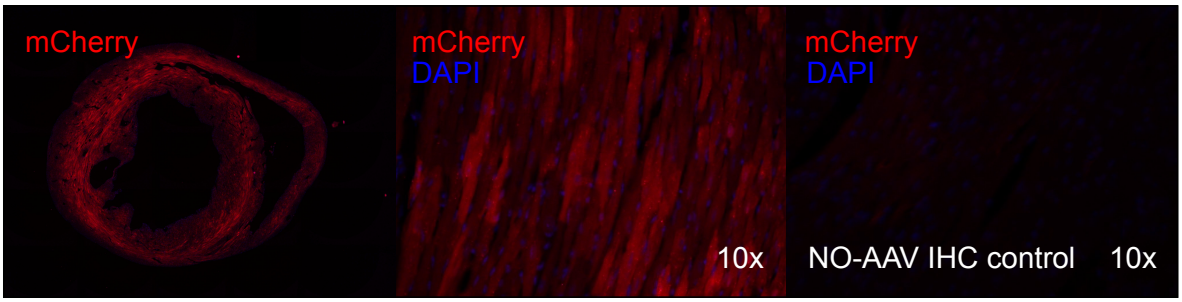

(a) ssAAV9-TnT-mCherry

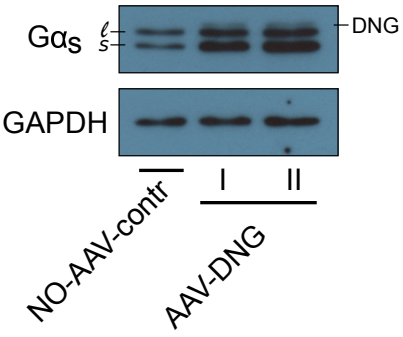

(b)

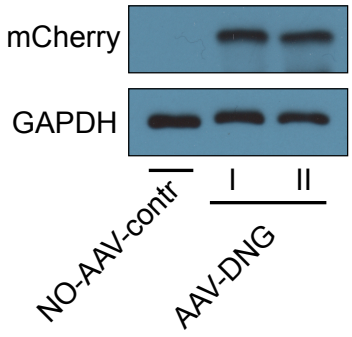

(c)

Figure 3.7: Initial Gα_s and reporter protein mCherry expression analysis in AAV-DNG injected mice. Representative IHC images of cross-sectional cardiac tissue sections stained with anti mCherry antibody (red) and DAPI (blue) **(a)**, WB probing for Gα_s (5 µg protein/lange) **(b)** and mCherry (18 µg protein/lange) **(c)** from 11 weeks old mice, 6 weeks after systemic injection of 10^{12} vg/animal of ssAAV9-TnT-mCherry-2A-DNG (AAV-DNG). No-AAV injected mouse cardiac tissue was used as control for IHC staining and WB analysis.

3.3.2 Baseline cardiac function of AAV injected mice

Baseline cardiac function was assessed by transthoracic echocardiography under isoflurane anaesthesia in 11-12 weeks old mice (C57Bl6/J), 3 weeks after the injection of 10^{12} vg/animal of either ssAAV9-TnT-mCherry-2A-DNG or ssAAV9-TnT-mCherry. Obtained echocardiographic parameters are shown in Table 3.1.

Heart rate during echocardiographic analysis was similar in between groups. No significant differences in functional cardiac parameters ejection fraction (EF) and fractional shortening (FS) were observed. AAV-DNG injected mice exhibited statistically significant increase in the dimensions of the left ventricular posterior wall in diastole (LVPWd). The LVPWd was unaltered in the AAV-mCherry injected control animals.

Table 3.1: Transthoracic echocardiograms of AAV-DNG injected mice. Echocardiograms were obtained under isoflurane anaesthesia from 11 weeks old mice 3 weeks after the systemic injection of 10^{12} vector genomes of ssAAV9-TnT-mCherry (AAV-mCherry) or ssAAV9-TnT-mCherry-2A-DNG (AAV-DNG). Significance was tested by unpaired Student's t-test. $\star$ is p-value of < 0.05, $\star\star\star$ is p-value of < 0.001.

	Units	AAV-mCherry (n=12)	AAV-DNG (n=11)
Weight	g	21.13 ± 0.31	21.40 ± 0.23
Heart rate	bpm	382.42 ± 10.30	378.00 ± 6.82
EF	%	37.68 ± 1.78	33.59 ± 2.24
FS	%	18.26 ± 0.98	16.08 ± 1.16
IVSd	mm	0.19 ± 0.01	0.23 ± 0.02
IVSs	mm	0.42 ± 0.03	$0.52 \pm 0.03^{*}$
LVPWd	mm	0.17 ± 0.01	$0.20 \pm 0.01^{*}$
LVPWs	mm	0.33 ± 0.02	0.33 ± 0.02
LVIDd	mm	5.20 ± 0.04	5.35 ± 0.07
LVIDs	mm	4.42 ± 0.09	4.60 ± 0.10
LV mass/BW	a.u.	3.33 ± 0.20	3.64 ± 0.30

3.3.3 Model of chronic β-AR stimulation induced cardiac hypertrophy

To investigate the effect of DNG on the development of β-AR induced cardiac hypertrophy *in vivo*, β-AR were stimulated in AAV injected mice by chronic one-week infusion of unselective β-AR agonist isoproterenol.

6 mice (C57Bl6/J) per group that were previously assessed for basal cardiac function were

randomly assigned to receive either chronic exposure to isoprenaline (30 µg/g/day) or vehicle over 1 week by the subcutaneous implantation of agonist loaded osmotic minipumps. Cardiac function was assessed by transthoracic echocardiography under isoflurane anaesthesia before and after agonist exposure. Hearts were subsequently excised for the analysis of transgene expression and cardiac remodeling, in particular the development of hypertrophy which was assessed in heart weight to tibia length ratio, cardiomyocyte size in histology slides. Gene expression was analyzed for DNG effect on a surrogate marker of the β-AR signaling cascade, and the expression of pathological hypertrophy associated *fetal genes*.

Furthermore, the expression of genes related to cardiac fibrosis and fibrosis in histology slides were analyzed.

Transthoracic echocardiography

Obtained echocardiographic results before and after the induction of β-AR induced cardiac hypertrophy in AAV injected mice are shown in Figure 3.8 with further parameters shown in Table 3.2.

Heart rate at rest was similar in the vehicle exposed AAV-injected animals. In response to ISO exposure, heart rate was significantly increased by approximately 40 % in AAV-mCherry and 47 % in AAV-DNG injected mice compared to vehicle control.

In the post-pump inter-group comparison, functional parameters EF and FS were significantly enhanced by approximately 54 % and 66 % in the AAV-mCherry ISO group compared to AAV-mCherry vehicle control whereas in the AAV-DNG injected animals the increase to ISO exposure in EF and FS was insignificant at 34 % and 41 % respectively. The increase in heart rate, EF and FS did not differ significantly in between the ISO exposed AAV-mCherry and AAV-DNG injected animals.

The ISO exposure resulted in concentric hypertrophic growth in AAV-mCherry injected animals with significant increase in left ventricular structural dimensions. In the post-pump inter-group comparison, the ISO exposure resulted in a significant increase in wall dimensions interventricular septum in diastole (IVSd) (114 %) and left ventricular posterior wall in diastole (LVPWd) (121%). The left ventricular internal diameter in diastole (LVIDd) did not change significantly in response to ISO exposure.

In AAV-DNG injected animals, the observed increase in left ventricular wall dimensions to ISO exposure were significantly attenuated. In the post-pump inter-group comparison, the increase in left ventricular wall dimensions IVSd (48 %) and LVPWd (22 %) to ISO expo-

sure were not significant. The LVIDd in the AAV-DNG injected animals was not affected in response to ISO exposure.

In the ISO vs. ISO group comparison, LVPWd increase was significantly reduced in the AAV-DNG injected animals compared to AAV-mCherry control.

The increase in estimated left ventricular mass to body weight ratio (LV mass/BW) in the ISO treated groups were not statistically significant. The left ventricular mass to tibia length although increased significantly by approximately 53 % in both the AAV-mCherry as well as in the AAV-DNG group.

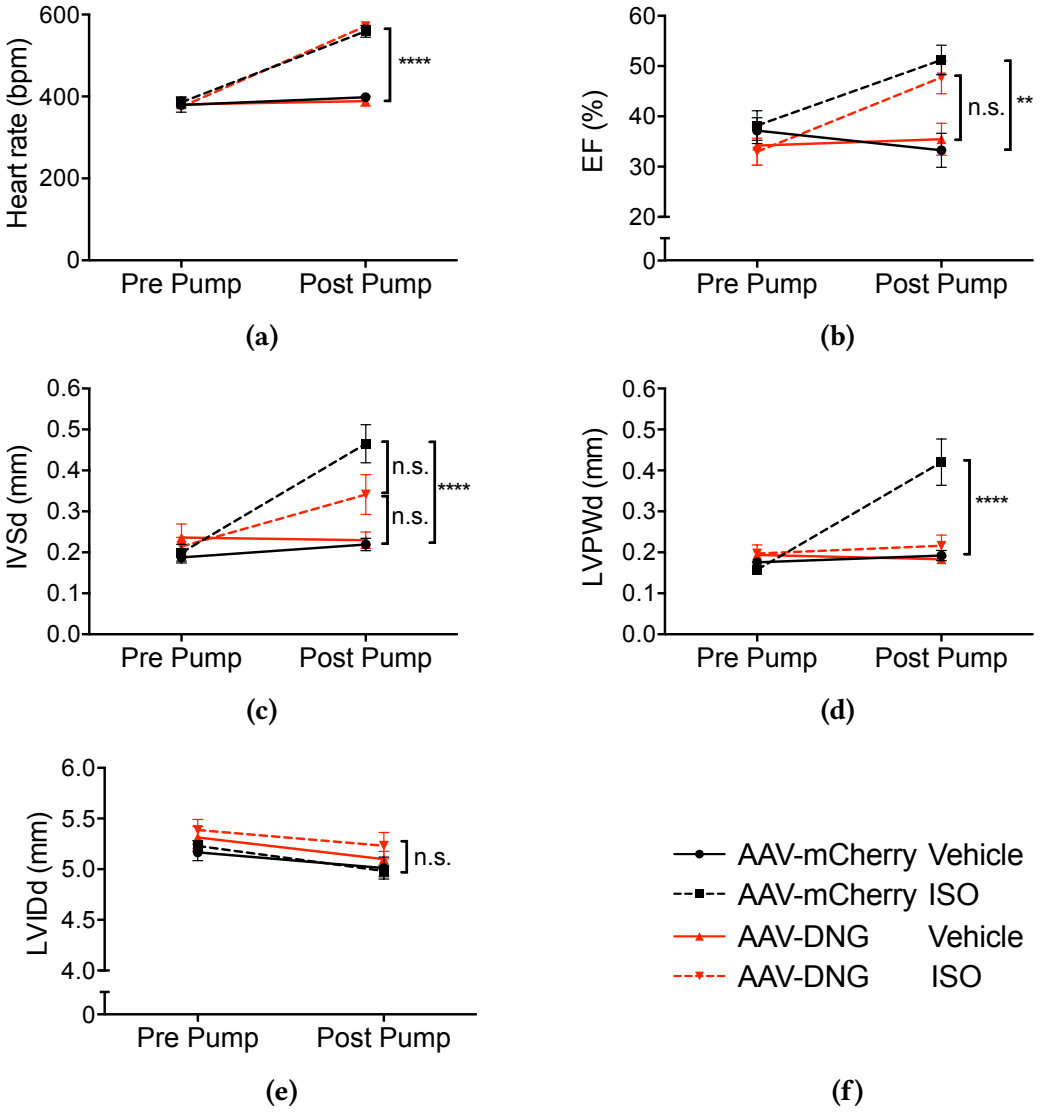

Figure 3.8: Transthoracic echocardiography of mice expressing DNG in model of chronic β-AR stimulation driven cardiac hypertrophy. Echocardiograms were obtained under isoflurane anaesthesia before and after the induction of cardiac hypertrophy by chronic β-AR stimulation (Isoprenaline 30 µg/g/day (ISO) vs. vehicle infusion over 1 week) in 11-12 weeks old mice 3-4 weeks after the systemic injection of 10^{12} vector genomes of ssAAV9-TnT-mCherry (AAV-mCherry) or ssAAV9-TnT-mCherry-2A-DNG (AAV-DNG). Echocardiographic parameters shown: **(a)** Heart rate (beats per minute), **(b)** Ejection fraction (%), **(c)** interventricular septum in diastole (mm), **(d)** left ventricular posterior wall in diastole (mm), **(e)** left ventricular internal diameter in diastole (mm), **(f)** corresponding labels. Data are mean values $\pm$ SEM, n = 5-6 animals per group. Significance was analyzed in the post pump groups by two-way ANOVA following Tukey's post-hoc test. $\star\star$ is p-value of < 0.01, $\star\star\star\star$ is p-value of < 0.0001

Table 3.2: Transthoracic echocardiograms of mice expressing DNG in model of chronic β-AR stimulation driven cardiac hypertrophy. Echocardiograms were obtained under isoflurane anaesthesia from 12 weeks old mice 4 weeks after the systemic injection of 10^{12} vector genomes of ssAAV9-TnT-mCherry (AAV-mCherry) or ssAAV9-TnT-mCherry-2A-DNG (AAV-DNG) after the induction of cardiac hypertrophy by chronic 1 week β-AR stimulation (Isoprenaline 30 µg/g/day (ISO) vs. vehicle infusion). Significance was analyzed by two-way ANOVA following Tukey's post-hoc test. Symbols represent significant differences in between groups. ⋆ is AAV-mCherry Vehicle vs. ISO, † is AAV-DNG Vehicle vs. ISO, # is ISO vs. ISO. No significant differences were observed in Vehicle vs. Vehicle. Repeated symbols are used as follows: Single is p-value of < 0.05, double is p-value of < 0.01, triple is p-value of < 0.001 and quadruple is p-value of < 0.0001.

		AAV-mCherry		AAV-DNG	
	Units	Vehicle (n=6)	ISO (n=6)	Vehicle (n=6)	ISO (n=5)
Weight	g	24.21 ± 0.89	26.40 ± 0.32	24.66 ± 0.37	26.61 ± 0.57
Heart rate	bpm	398.33 ± 10.25	559.33 ± 13.13****	388.50 ± 11.01	571.80 ± 8.01††††
EF	%	33.25 ± 3.07	51.22 ± 2.68 **	35.40 ± 2.90	47.73 ± 2.94
FS	%	15.84 ± 1.59	26.21 ± 1.68 **	17.01 ± 1.56	24.04 ± 1.81
IVSd	mm	0.22 ± 0.01	0.47 ± 0.04 ***	0.23 ± 0.02	0.34 ± 0.04
IVSs	mm	0.39 ± 0.02	0.85 ± 0.06 ****	0.42 ± 0.03	0.69 ± 0.04††
LVPWd	mm	0.19 ± 0.01	0.42 ± 0.05 ****	0.18 ± 0.01	0.22 ± 0.02##
LVPWs	mm	0.32 ± 0.01	0.67 ± 0.09 **	0.34 ± 0.02	0.45 ± 0.04
LVIDd	mm	5.01 ± 0.10	4.98 ± 0.05	5.10 ± 0.07	5.23 ± 0.12
LVIDs	mm	4.38 ± 0.07	3.94 ± 0.15	4.48 ± 0.10	4.27 ± 0.14
ENDOarea d	mm^2	16.00 ± 0.28	15.69 ± 0.47	16.57 ± 0.44	17.27 ± 0.75
ENDOarea s	mm^2	11.43 ± 0.44	10.05 ± 0.61	12.28 ± 0.65	10.51 ± 0.83
EPIarea d	mm^2	20.39 ± 0.44	25.04 ± 0.50 ****	20.69 ± 0.42	23.38 ± 0.76†
EPIarea s	mm^2	18.09 ± 0.68	21.96 ± 0.64 **	19.28 ± 0.37	21.64 ± 0.99
LV mass/BW	a.u.	2.83 ± 0.22	3.91 ± 0.46	2.92 ± 0.21	4.09 ± 0.21
LV mass/TL	a.u.	3.94 ± 0.20	6.04 ± 0.69 *	4.19 ± 0.30	6.39 ± 0.45†

Transgene expression analysis

Transgene expression was additionally analysed 4 weeks after AAV injection and after the induction of chronic β-AR stimulation induced cardiac hypertrophy.

IHC staining of cross-sectional cardiac tissue using mCherry specific antibody was performed to quantify the reporter fluorescence mCherry positive cardiomyocytes in vehicle treated AAV-mCherry and AAV-DNG injected mice. Furthermore, western blot analysis from gross left ventricular tissue protein lysates was used for the detection of Gα_s, which is also specific to DNG. Expression analysis was complemented by rt-qPCR gene expression analysis of Gα_s *GNAS* complex locus gene and *DNG* in mRNA from gross left ventricular tissue.

Images of IHC stained cross-sectional heart sections are shown in Figure 3.9. Even ventricular mCherry expression was confirmed in all animals. The number of mCherry expressing cardiomyocytes was counted manually in anti-mCherry IHC stained cross-sectional heart sections as described in section 2.2.10. In the vehicle treated AAV-mCherry group, 33.49 ± 3.19 % of CM and 54.61 ± 3.39 % of CM in the vehicle treated AAV-DNG group exhibited strong mCherry fluorescence.

Transgene expression was further analyzed in gross left ventricular tissue by western blot probing for Gα_s, which also detects DNG. CSQ was used as loading control as shown in Figure 3.10a and 3.10b. Gα_s protein was significantly reduced by 18 % in AAV-DNG injected and vehicle exposed animals compared to AAV-mCherry vehicle control. The enhanced Gα_s signal as well as the appearance of a double band indicating DNG, as it was detected in the initial transgene expression analysis in Figure 3.7, was not reproduced. In the ISO exposed animals, the Gα_s protein expression was significantly reduced to near identical values of 35 % of initial Gα_s protein in AAV-mCherry and AAV-DNG injected animals.

At the transcriptional level Gα_s gene *GNAS* in gross left ventricular tissue was not affected by neither AAV injection nor one week ISO exposure as shown in Figure 3.10c. The absence of enhanced Gα_s WB signal in AAV-DNG injected mice was further complemented by DNG specific rt-qPCR. DNG mRNA expression in gross left ventricular tissue in AAV-DNG injected animals is shown in Figure 3.10d. *DNG* expression normalized to *GAPDH* as housekeeping gene was approximately 5 % of the expression level of *GAPDH* normalized *GNAS*. The *DNG* expression level did not change significantly after ISO exposure.

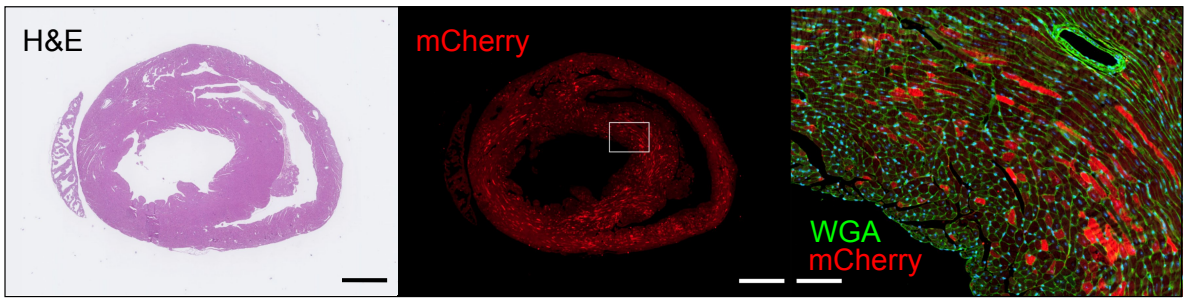

(a) ssAAV9-TnT-mCherry

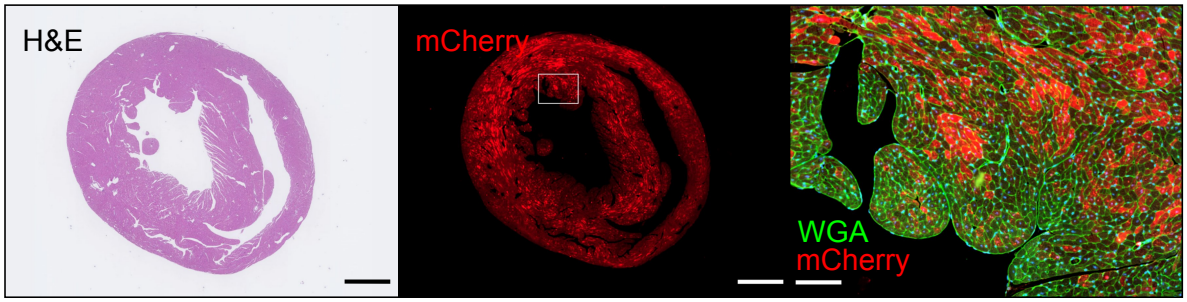

(b) ssAAV9-TnT-mCherry-2A-DNG

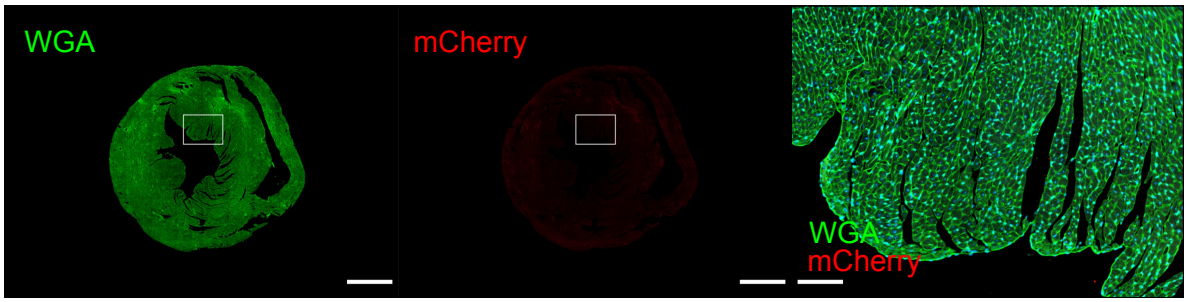

(c) No-AAV injected IHC control

Figure 3.9: Reporter protein expression analysis in mouse cardiac IHC stained histology slides after systemic AAV injection. Representative images of cross-sectional cardiac tissue sections from 3 months old vehicle treated mice, 4 weeks after systemic injection of 10^{12} vector genomes of ssAAV9-TnT-mCherry (AAV-mCherry) **(a)** or ssAAV9-TnT-mCherry-2A-DNG (AAV-DNG) **(b)** and no-AAV injected immunohistochemistry control in **(c)** stained with anti-mCherry antibody (red), WGA (green) and DAPI (blue) for the detection of reporter fluorescence protein mCherry. Scale bar is 1 mm in the two left whole slide images, 100 µm in right enlarged images.

Heart weight to tibia length ratio and cardiomyocyte size

Cardiac hypertrophy was analysed by measuring heart weight to tibia length ratio (HW/TL) and cardimoyocyte cross-sectional area in histology slides from one-week ISO exposed AAV injected animals as shown in Figure 3.11.

One week ISO exposure resulted in significant cardiac hypertrophy. This was observed in the heart weight to tibia length ratio in the AAV-mCherry group with an increase of approximately 28 % (8.3 ± 0.36 mg/mm to 10.63 ± 0.68 mg/mm) to ISO exposure. The increase in HW/TL ratio was slightly reduced and statistically insignificant in the AAV-DNG group at approximately 21 % (8.63 ± 0.45 mg/mm to 10.46 ± 0.35 mg/mm) with no statistically significant difference observed in between the ISO exposed groups.

Mean cardiomyocyte cross-sectional area increased in both ISO exposed groups but not to a statistically significant degree. In the AAV-mCherry group, there was a mean increase of 10.2 % (2212 ± 100.5 a.u. to 2437 ± 97.41 a.u.) and in the AAV-DNG group of 15.6 % (2094 ± 78.29 a.u. to 2421 ± 116.2 a.u.).

Nanostring®gene expression analysis for DNG effect on β-AR signaling cascade and pathological hypertrophy

Chronic β-AR stimulation has profound effects on the cardiac β-AR signaling cascade, stress signalling and development of pathological cardiac hypertrophy, which is accompanied by re-expression of *fetal* genes. Nanostring®nCounter®technology was used to assess gene expression in gross left-ventricular tissue. The following genes were analyzed: protein phosphatase inhibitor-1 (PPI-1), four and a half LIM domain protein 1 (Fhl1), four and a half LIM domain protein 2 (Fhl2) as well as the typical *fetal* genes α-myosin heavy chain (Myh6), β-myosin heavy chain (Myh7), natriuretic peptide A (ANP) and natriuretic peptide B (BNP). Normalized mRNA counts are shown in figure 3.12.

The expression of PP-I1 (*Ppp1r1a*) was similar in the vehicle exposed AAV-mCherry and AAV-DNG animals. In response to ISO although, the expression was significantly reduced in AAV-mCherry (-60 %) and to a lesser degree in AAV-DNG (-43 %) animals. The expression of the biomechanical stress sensor *Fhl1* increased in response to ISO in the AAV-mCherry (59 %) and more pronounced in AAV-DNG (87 %) group. The *Fhl2* expression on the contrary did not change in this study. A significant reduction in *Myh6* (-29 %) was observed in the ISO exposed AAV-mCherry group, while in the AAV-DNG group, the reduction in *Myh6* (-10 %) was insignificant. The *Myh7* expression levels were not significantly affected. The expression of genes encoding for the two natriuretic peptides ANP and BNP were differently affected: While the *Nppb* expression was unaltered, the *Nppa* expression in in response to ISO was increased by 217 % the AAV-mCherry group. This increase was abolished in the ISO exposed AAV-DNG group.

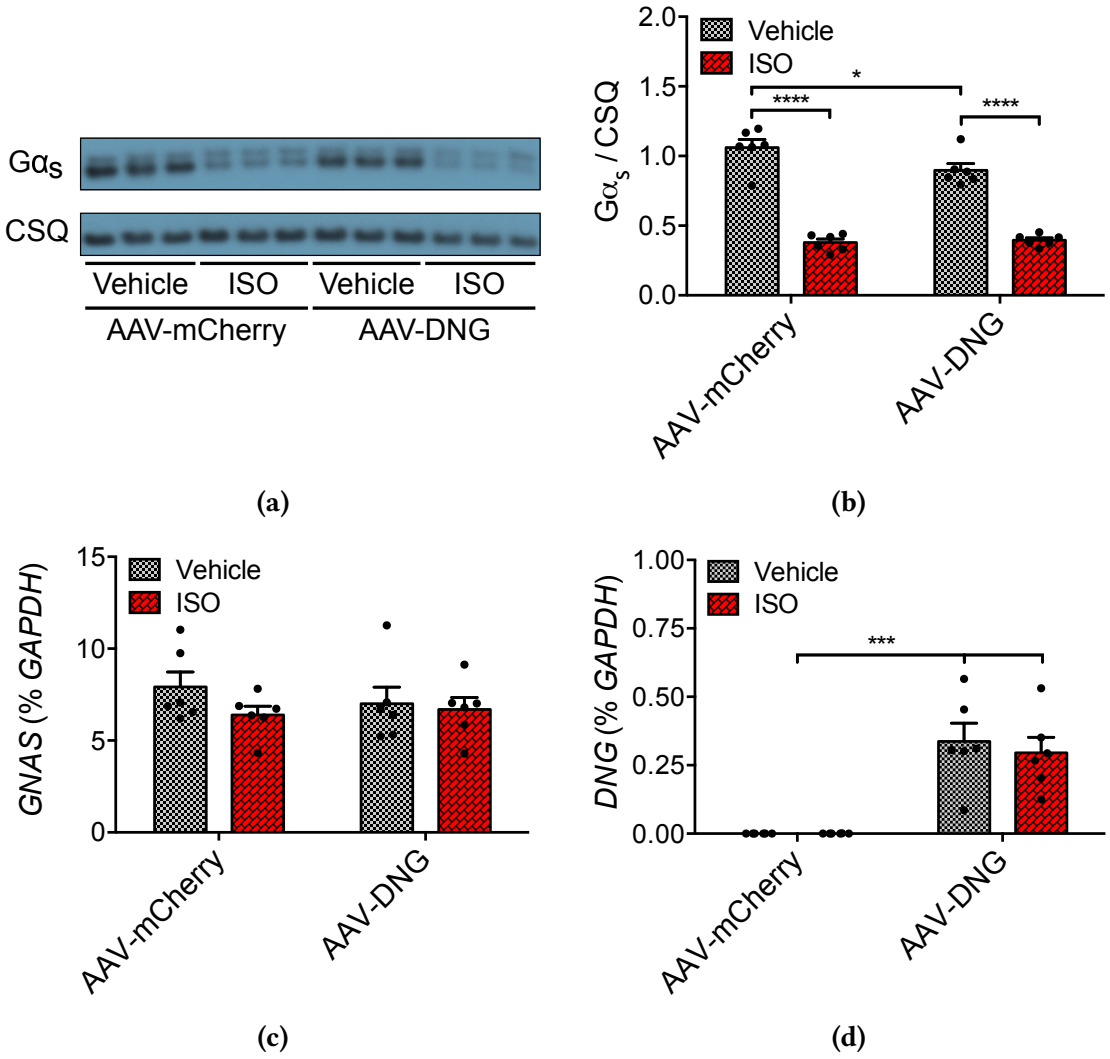

Figure 3.10: Expression analysis of Gα_s and DNG on RNA and protein level of mice expressing DNG after model of chronic β-AR stimulation driven cardiac hypertrophy. Western blot and rt-qPCR from left ventricular tissue from mice after the induction of cardiac hypertrophy by chronic β-AR stimulation (Isoprenaline 30 µg/g/day (ISO) vs. Vehicle infusion over 1 week) in 12 weeks old mice 4 weeks after the systemic injection of 10^{12} vector genomes of ssAAV9-TnT-mCherry (AAV-mCherry) or ssAAV9-TnT-mCherry-2A-DNG (AAV-DNG). **(a)** is representative Gα_s western blot with CSQ as loading control (5 µg protein/lange). **(b)** corresponding quantification of Gα_s western blot to loading control CSQ. **(c)** rt-qPCR for the detection of Gα_s complex locus *GNAS* in relation to housekeeping gene *GAPDH*. **(d)** rt-qPCR for the detection of *DNG* in relation to housekeeping gene *GAPDH*. Data are mean values $\pm$ SEM, n = 5-6 animals per group. Significance was analyzed by two-way ANOVA following Tukey's post-hoc test. $\star$ is p-value of < 0.05, $\star\star$ is p-value of < 0.01, $\star\star\star$ is p-value of < 0.0001.

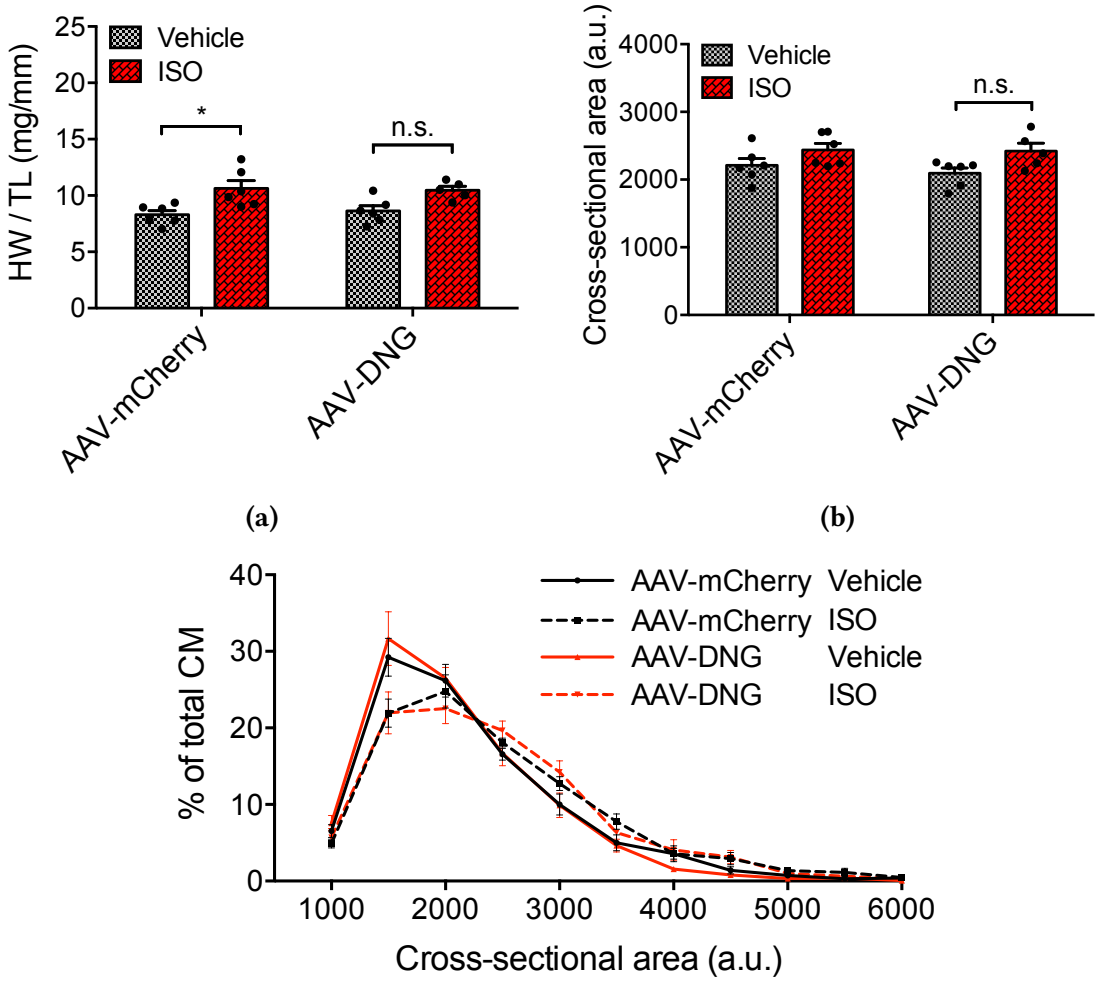

Figure 3.11: Development of hypertrophy in mice expressing DNG after model of chronic β-AR stimulation driven cardiac hypertrophy. **(a)** Heart weight to tibia length ratio and **(b)** cross-sectional cardiomyocyte area in paraffin embedded and WGA stained heart sections analyzed by semi-automated cardiomyocyte measurements with corresponding histogram **(c)** after the induction of cardiac hypertrophy by chronic β-AR stimulation (Isoprenaline 30 µg/g/day (ISO) vs. Vehicle infusion over 1 week) in 12 weeks old mice 4 weeks after the systemic injection of 10^{12} vector genomes of ssAAV9-TnT-mCherry (AAV-mCherry) or ssAAV9-TnT-mCherry-2A-DNG (AAV-DNG). Data are mean values $\pm$ SEM, n = 5-6 animals per group. **(a)** significance was analyzed by two-way ANOVA following Tukey's post-hoc test. **(b)** AAV-DNG vehicle group did not pass normality test and statistical significance was therefore analyzed with Kruskal-Wallis test followed by Dunn's multiple comparison test. $\star$ is p-value of < 0.05.

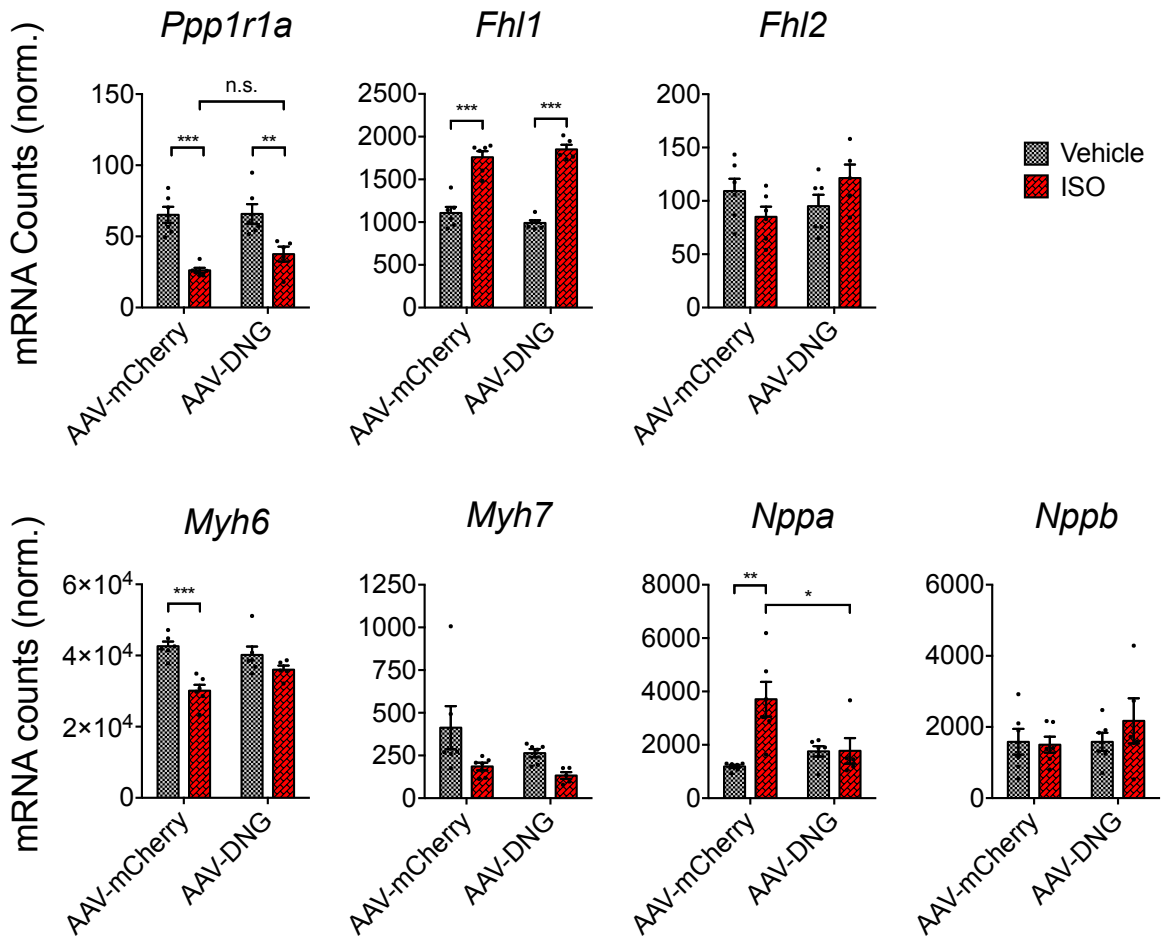

Figure 3.12: Expression of *fetal* genes in cardiac tissue from mice expressing DNG after model of chronic β-AR stimulation driven cardiac hypertrophy. Normalized Nanostring®mRNA counts (identical y-axis label in all graphs) from RNA isolated from left ventricular tissue after the induction of cardiac hypertrophy by chronic β-AR stimulation (Isoprenaline 30 µg/g/day (ISO) vs. Vehicle infusion over 1 week) in 12 weeks old mice 4 weeks after the systemic injection of 10^{12} vector genomes of ssAAV9-TnT-mCherry (AAV-mCherry) or ssAAV9-TnT-mCherry-2A-DNG (AAV-DNG). Displayed genes are: Protein Phosphatase Inhibitor-1 (*Ppp1r1a*), four and a half LIM domain protein 1 (*Fhl1*), four and a half LIM domain protein 2 (*Fhl2*), α-myosin heavy chain (*Myh6*), β-myosin heavy chain (*Myh7*), natriuretic peptide A (*Nppa*) and natriuretic peptide B (*Nppb*). Data are mean values $\pm$ SEM, n = 5-6 animals per group. Significance was analyzed by two-way ANOVA following Tukey's post-hoc test. $\star$ is p-value of < 0.05, $\star\star$ is p-value of < 0.01, $\star\star\star$ is p-value of < 0.001.

Concomitant fibrosis

The development of cardiac fibrosis was assessed by Nanostring® nCounter® gene expression analysis of genes related to fibrosis including *periostin (Postn)*, *collagen type I alpha 1 chain (Col1a1)* and *collagen type III alpha 1 chain (Col3a1)*. Furthermore, interstitial fibrotic area was measured in PSR stained cross-sectional heart sections.

As shown in Figure 3.13 the expression of fibrotic genes *Postn*, *Col1a1* and *Col3a1* increased significantly in both ISO exposed AAV-mCherry and AAV-DNG groups. The increase in the AAV-DNG ISO vs. AAV-mCherry ISO groups however was significantly attenuated. Neither group developed macroscopically detectable fibrosis as the area of interstitial fibrosis in PSR stained sections was unaltered.

3.3.4 Exclusion of AAV-DNG ISO exposed outlier

One animal was excluded from grouped analysis. The excluded animal belonged to the AAV-DNG injected and ISO exposed group. In comparison to the other animals of the respective intervention group, the excluded animal developed exacerbated eccentric heart failure with marked interstitial fibrosis as shown in Figure 3.14. Here, the left ventricular function was significantly impaired accompanied by left ventricular wall thinning. The interstitial fibrosis exceeded the 1.5 fold of the interquartile range. Such effects are not typical for the ISO infusion cardiac hypertrophy model (Chang, Ren, et al., 2018).

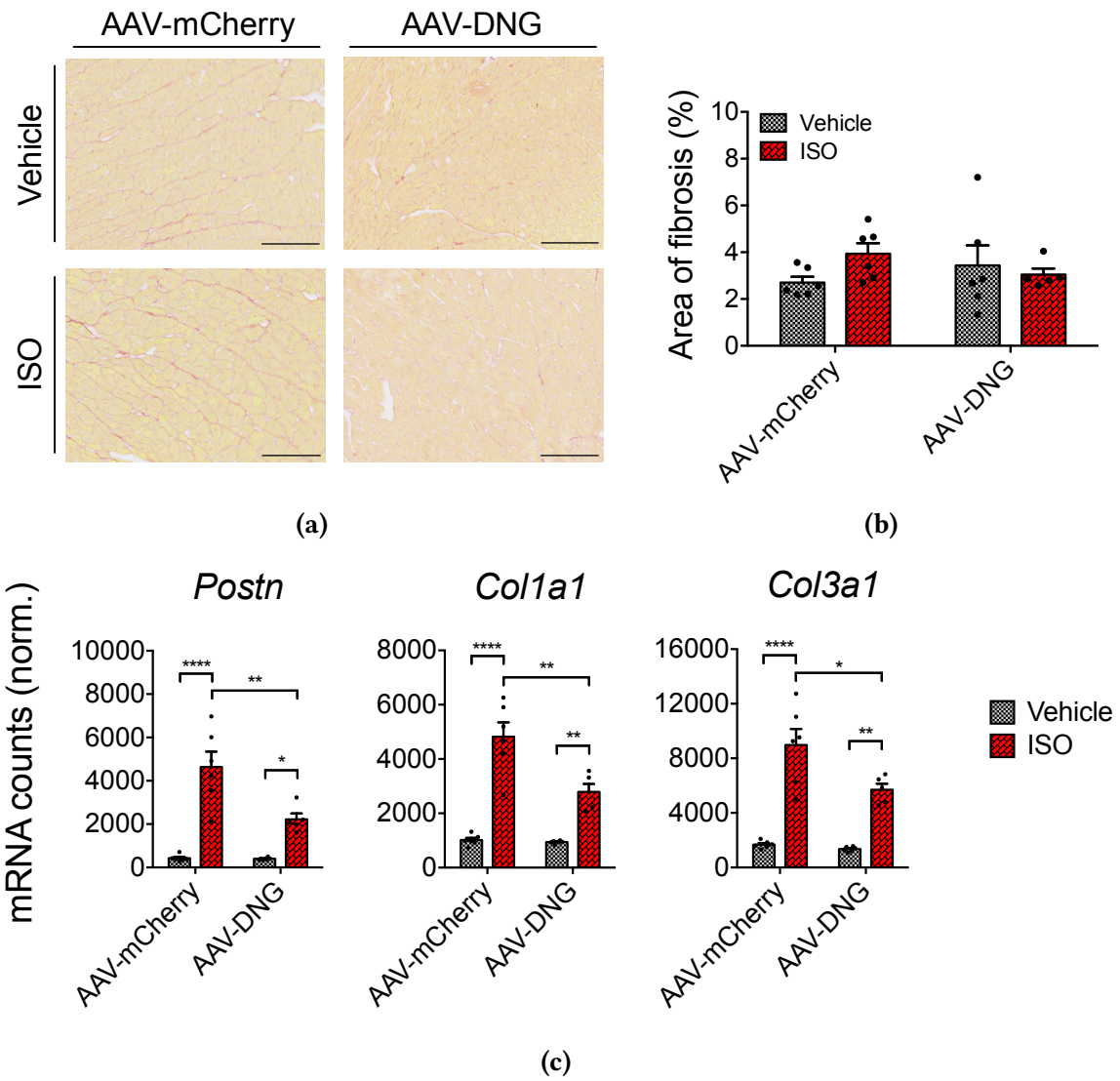

Figure 3.13: Fibrosis in cardiac tissue from mice expressing DNG after model of chronic β-AR stimulation driven cardiac hypertrophy. Representative PSR stained heart sections **(a)** with the respective quantification of fibrotic area **(b)** and normalized Nanostring®mRNA counts (identical y-axis label in the respective graphs) of fibrosis related genes periostin (*Postn*), collagen type I alpha 1 (*Col1a1*) and collagen type III alpha 1 (*Col3a1*) in **(c)** from left ventricular tissue after the induction of cardiac hypertrophy by chronic β-AR stimulation (Isoprenaline 30 µg/g/day (ISO) vs. Vehicle infusion over 1 week) in 12 weeks old mice 4 weeks after the systemic injection of 10^{12} vector genomes of ssAAV9-TnT-mCherry (AAV-mCherry) or ssAAV9-TnT-mCherry-2A-DNG (AAV-DNG). Data are mean values $\pm$ SEM, n = 5-6 animals per group. Significance was analyzed by two-way ANOVA following Tukey's post-hoc test. $\star$ is p-value of < 0.05, $\star\star$ is p-value of < 0.01, $\star\star\star\star$ is p-value of < 0.0001. Scale bar is 100 µm.

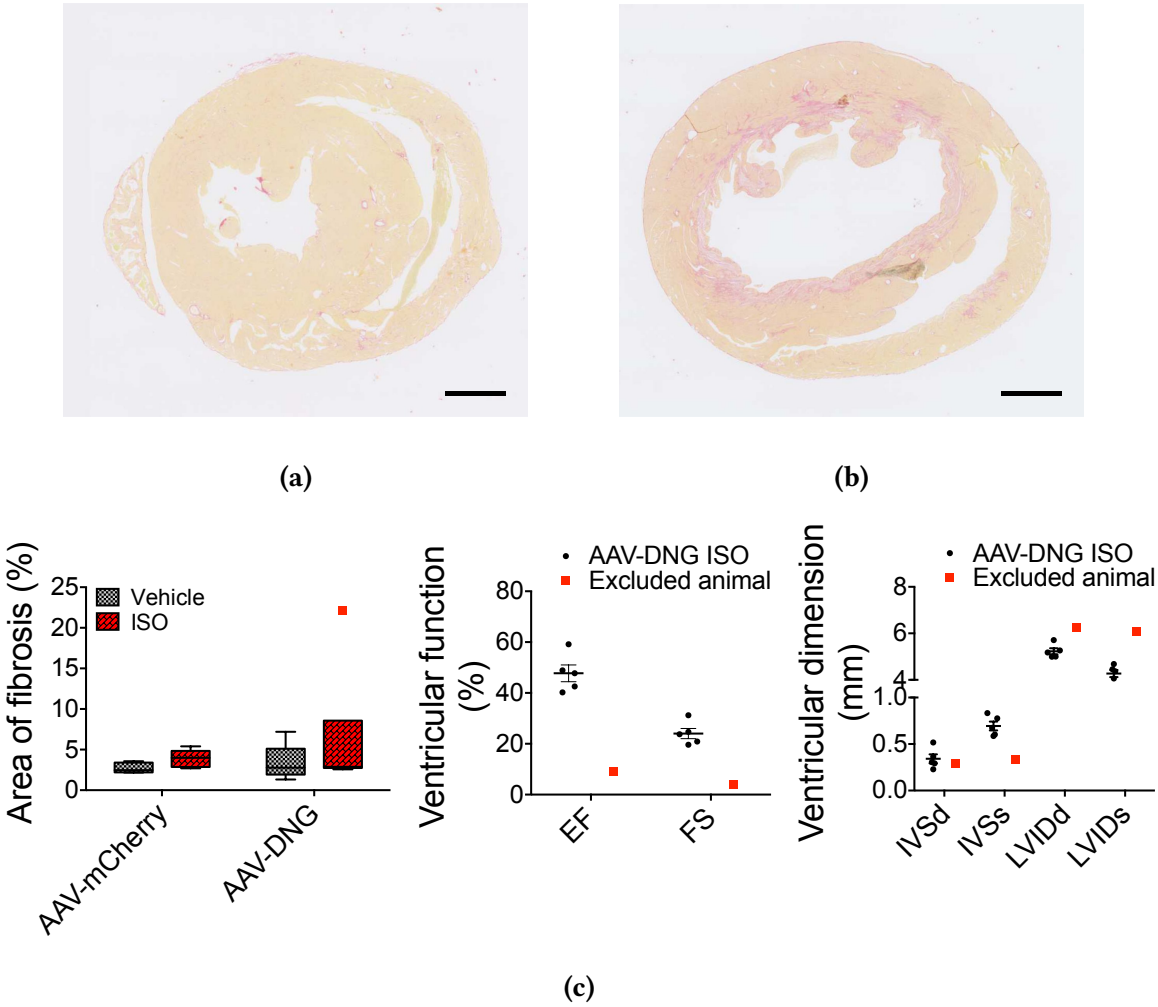

Figure 3.14: Exclusion of one animal from grouped analysis. The excluded animal belonged to the AAV-DNG injected and isoprenaline exposed group. The exclusion was based on excessive eccentric heart failure and fibrosis for which the area of fibrosis exceeded the 1.5 fold interquartile range in the corresponding group. **(a)**, representative PSR stained cross-sectional heart section from AAV-DNG ISO stimulated group. **(b)** PSR section from excluded animal with prominent fibrosis and left ventricular dilation. Corresponding quantification of fibrosis where data is represented as box plot with whiskers of 1.5 times the interquartile range. **((c) left)**, echocardiographic functional parameters EF and FS **((c) center)**, echocardiographic left ventricular dimensions **((c) right)**. n = 5-6 animals per group. Scale bar is 1 mm.

4 Discussion

The aim of this thesis was to test a dominant negative $G\alpha_s$ protein (DNG) for its ability to block the β-AR signaling cascade and subsequently prevent the development of hypertrophic growth to β_1-AR stimulation *in vitro*. Furthermore, cardiomyocyte specific DNG expression was to be achieved by AAV-mediated gene transfer to the murine heart *in vivo*. Mice with cardiomyocyte directed DNG expression were assessed for transgene expression. Also, the DNG effect on basal heart function as well as on the development of hypertrophy and remodeling in a model of chronic β-AR stimulation driven cardiac hypertrophy analyzed.

To summarize the results, DNG was successfully expressed *in vitro* by adenoviral gene transfer in ARVCM. *In vivo* expression of DNG to the murine heart was achieved by AAV-mediated gene transfer. The inhibition of the β-AR signaling cascade was shown *in vitro* with subsequently inhibited hypertorphic growth to chronic β_1-AR stimulation in ARVCM. The *in vivo* effect of DNG revealed a mild hypertrophic phenotype in echocardiography three weeks post AAV injection at rest. In response to chronic one-week β-AR stimulation AAV-DNG injected mice were protected from cardiac hypertrophy in echocardiography and also from enhanced expression of pathological hypertrophy related *fetal* and pro-fibrotic genes. The development of hypertrophy was significantly reduced in echocardiography in DNG expressing mice. However, DNG expressing mice were not protected from cardiac hypertrophy at the whole organ level, nor at the level of individual cardiomyocytes. One DNG expressing animal developed severe cardiac decompensation and was excluded from grouped analysis.

The following chapter is structured in a preceding discussion of the methods used for: (i) Cardiomyocyte directed gene transfer of DNG *in vitro* and *in vivo*, (ii) assessment of DNG functionality *in vitro* and model for induction of β-AR induced cardiac hypertrophy and remodeling and (iii) cardiomyocyte morphology measurements. Afterwards, the results of DNG expression on β-AR signaling cascade and subsequent development of hypertrophy *in vitro* are discussed including the *in vivo* effect on baseline cardiac function at rest and to chronic β-AR stimulation. Furthermore, the study limitations and a possible deployment of DNG as a gene therapy in heart failure are discussed followed by the conclusions and outlook.

4.1 Discussion of the methods

4.1.1 *In vitro* and *in vivo* gene transfer of DNG

The functionality and integrity of the cDNA DNG construct was first assessed in HEK-cells. HEK-cells are a suitable model to test DNG as they express Gα_s coupled β-ARs (Lavoie et al., 2002). Gene transfer of DNG in HEK-cells can be achieved by transient transfection of pcDNA3-DNG plasmid. The implementation of DNG in the cardiomyocyte system was first approached *in vitro* by adenoviral gene transfer of DNG in ARVCM. The majority of *in vitro* studies regarding ventricular cardiomyocytes, either neonatal rat ventricular myocytes, adult ventricular myocytes isolated from rat or mouse, H2C9 myoblasts or human embryonic and pluripotent stem cells are used (Peter et al., 2016). ARVCM were chosen for reasons of availability and acquired experience in culture and gene transfer. Furthermore, in comparison to neonatal rat ventricular myocytes, ARVCM resemble more closely the adult physiology. Fully differentiated ARVCM are not suitable for non-viral gene transfer (Louch et al., 2011). Gene transfer can be achieved by the use of adenovirus. In ARVCM adenovirus are commonly used as viral vectors for gene transfer. The adenovirus type 5 harbouring the CMV promoter achieves homogeneous transgene expression in ARVCM 24-48 hours post-transduction (Kirshenbaum et al., 1993). Due to the intention to co-express fluorescent FRET biosensor for subsequent FRET measurements attachment of a fluorescent reporter gene to analyze transgene expression was not desired. Transgene expression was subsequenty analyzed by Gα_s western blot. Sufficient DNG expression was achieved in ARVCM by adenoviral gene transfer 24 hours post transduction as shown in Figure 3.2.

The *in vivo* expression of DNG was achieved by the use of AAVs as viral vectors for gene transfer. Recombinant AAV are increasingly used for gene therapy approaches in cardiovascular research and are currently tested in human heart failure gene therapy trials (Kieserman et al., 2019). Recombinant AAV-serotype 9 is the preferred choice for cardiac gene transfer in the mouse. One reason is the high natural tropism of AAV9 to the heart (Inagaki et al., 2006) which reduces transduction of other tissues or organs. To further eliminate off-target transgene expression, the cardiac specificity was enhanced by harboring the human cardiac troponin T (TnT) promoter. Werfel et al. (2014) generated an AAV9 using the human TnT promoter which is highly specific to cardiomyocytes, achieves sustained promoter activity over time and does not induce any adverse transduction related reactions in other organs. Furthermore, no inflammatory response in the heart of AAV9 injected mice is observed. Due to the favorable characteristics the AAV9 harbouring the human cardiac TnT promoter was

chosen as viral vector for *in vivo* gene transfer.

The genome of naturally occurring AAVs is single-stranded DNA. To become transcriptionally active it requires the synthesis of double-stranded DNA by the host cell (Ferrari et al., 1996). For single-stranded AAV (ssAAV) the complementary-strand synthesis is rate limiting and reduces efficiency (McCarty et al., 2003). With the introduction of self-complementary AAV (scAAV) this rate limiting step was overcome. scAAV were designed as a single-stranded inverted repeat with two palindromic inverted repeats at the respective ends and a mutated terminal repeat at the center. The single-stranded DNA self-anneals to double-stranded DNA upon viral unpacking in the host-cell and circumvents the need for complementary-strand synthesis (McCarty et al., 2003). The disadvantage of scAAV is the reduced packaging capacity of approximately 2.4 kB (Wu et al., 2007).

To determine the transduction efficiency the fluorescence protein mCherry was expressed as a reporter gene along with DNG and additionally used as the transgene in the control AAV. The DNG construct was attached to mCherry via the 2A sequence (Luke et al., 2008) which results in post-translational cleavage of the respective proteins and cytosolic mCherry expression. The combined size of the TnT promoter, mCherry-2A-DNG and the polyadenylation tail is 2.7 kB and is exceeding the above mentioned 2.4 kB maximum packaging capacity of scAAV. Single-stranded AAV serotype 9 was therefore used. Although the use of ssAAV exhibits reduced expression efficacy, high transgene expression can be achieved in the mouse heart by tail-vein injection of ssAAV9. Inagaki et al. (2006) reported a cardiac transduction efficiency of 99.5 % 10-12 days after tail-vein injection of 10^{12} vg of single-stranded AAV9-lacZ in C57BL/6 mice. 10^{12} vg of ssAAV9 were used in this study to ensure sufficient transgene expression and the effect of DNG analyzed by initiation of agonist exposure 21 days post AAV injection. In depth discussion of the AAV mediated DNG gene transfer in cardiomyocytes follows in Section 4.2

4.1.2 Assessment of DNG functionality and model of β-AR induced cardiac hypertrophy and remodeling

The ability of DNG to inhibit $G\alpha_s$ coupled β-AR signaling was initially assessed *in vitro* in HEK cells and subsequently in ARVCM. HEK cells are a suitable model to test DNG as they express β-ARs (Lavoie et al., 2002) and can therefore be utilized by measuring cytosolic cAMP reaction to β-AR stimulation. Stimulation of the β-ARs activates AC which produces cAMP. cAMP dynamics were measured in HEK cells and ARVCM in high temporal resolution by live

cell FRET microscopy using cytosolic FRET-cAMP biosensor Epac1-camps (Nikolaev, Bünemann, Hein, et al., 2004). β-AR were stimulated by 100 nM isoproterenol (ISO), which is a non-selective β-AR agonist, and the response related to maximum FRET induced by broad inhibition of PDEs and activation of ACs. To verify the cAMP-FRET results and uncover the inhibitory effect on a downstream target of the β-AR signaling axis the phosphorylation state of PLN was analyzed in Adv-DNG transducted ARVCM by western blot. PLN is one of the key PKA substrates, critically involved in the excitation-contraction coupling machinery and phosphorylated at the Ser^{16} residue upon β-AR stimulation (MacLennan and Kranias, 2003).

Sustained β_1-AR stimulation induces hypertrophic growth in ARVCM (Schäfer et al., 2000). Here, DNG was tested in ARVCM in the ability to block hypertrophic growth to sustained β_1-AR stimulation. Schäfer et al. (2000) demonstrated that ISO can only induce hypertrophic growth in ARVCM to selective β_1-AR stimulation which was achieved by equimolar presence of the β_2-AR antagonist ICI-118551 (ICI) or Gα_i inhibitor pertussis toxin. The cardiomyocytes in the study by Schäfer et al. (2000) were cultured for 24 h in the presence of 10 µM ISO/ICI and increased in cell length by approximately 10 %, cell width by 17 % and cell surface area by 30 %.

The degree of ARVCM hypertrophy to β_1-AR stimulation was less pronounced than anticipated (Fig. 3.5). In the control cardiomyocytes a 7 % increase in cell surface area to 10 µM ISO/ICI was observed. The discrepancy to the degree of hypertorphy reported by (Schäfer et al., 2000) could have been caused by the use of a fixed dose of 50 nM ICI throughout all ISO concentrations which was adapted from a study by Schirmer et al. (2018). This differed to the equimolar ISO/ICI used by Schäfer et al. (2000). With increasing ISO concentration and relative reduction in the proportional ICI, the ICI β_2-AR competitive antagonism could have been overcome and further hypertrophic growth inhibited by β_2-AR Gα_i action. Although, in the study by Schirmer et al. (2018), the increase in cell-surface area to 10 µM ISO/50 nM ICI reached approximately 20 %. In contrast to the study by Schäfer et al. (2000) however, the stimulation was initiated 24 h post-transduction in this thesis, even 72 h in the study by Schirmer et al. (2018), which most probably has impacted the cell surface density of responsive β-AR and thus impaired the hypertrophic response to chronic β-AR stimulation. On the other hand, robust increase of up to 10 % in cell width have been reported previously in adenovirus transducted ARVCM to 10 µM ISO without co-administration of ICI 24 h post transduction (Li et al., 2020). The limited hypertrophic growth, compared to the literature, could also have been due to partially degraded ISO.

Contrary to the study by Schäfer et al. (2000), in which hypertrophic growth was only

observed at ISO concentrations of $\geqslant 3$ µM, significant increase in cell-surface area and cell width was observed to 100 nM ISO as shown in Figure 3.5. This minor but significant increase in size was measured by the use of objective semi-automatic morphology measurements which will be discussed in depth in Section 4.1.3.

The ability of DNG to inhibit β-AR stimulation induced hypertrophy and remodeling was investigated in *in vivo* in AAV-DNG injected mice. Chronic infusion of ISO was chosen in this study to model the contribution of β-AR signaling in driving cardiac hypertrophy and remodeling in the hyperadrenergic state observed in heart failure disease progression. The degree of cardiac remodeling and decompensation over time to chronic ISO infusion is dependent on the mouse strain, dosing, application and duration of ISO exposure (Wang, Rau, et al., 2016; Rau et al., 2015). Cardiac hypertrophy in response to sustained sub-cutaneous (s.c.) ISO infusion at 30 µg/g/day in C57/Bl6J mice can be observed as early as three days following continuous ISO infusion (Puhl et al., 2016). Marked cardiac hypertrophy, fibrosis and LV-dilation reflecting cardiac decompensation is seen in C57/Bl6J mice following 14 d s.c. infusion at 60 µg/g/day ISO or prolonged four weeks intraperitoneal injection at 10 µg/g/day (Yan et al., 2015; Grimm et al., 2015). In C57/Bl6J at 30 µg/g/day of ISO up to 14 d there is usually no sign of cardiac decompensation but marked cardiac hypertrophy (Puhl et al., 2016), re-expression of *fetal* genes and development of cardiac fibrosis (Grimm et al., 2015; Webb et al., 2010). With emphasis on the initial phase of hypertrophy development a one week duration of chronic s.c. ISO infusion at 30 µg/g/day was chosen in this study.

The ISO model was functional as shown by the HW/TL ratio increase of approximately 28 % to one-week ISO (Fig. 3.11). The degree of HW/TL ratio increase is comparable to the literature. As an example, a 20 % increase in HW/TL ratio was observed following three days of 30 µg/g/day ISO (Puhl et al., 2016) and 17 % increase following one week of 15 µg/g/day ISO (El-Armouche, Wittköpper, et al., 2008).

4.1.3 New implementation of semi-automated cardiomyocyte hypertrophy measurements

Measurements of cardiomyocyte hypertrophy of isolated cardiomyocytes and cardiomyocytes *in situ* are frequently performed on images manually which, from personal experience, is susceptible to investigator bias. Although blindfolded analysis somewhat improves this bias, it is hypothesized that an automated image analysis with definite inclusion or exclusion criteria for analysis is advantageous in terms of objectivity, reliability and time efficiency.

ARVCM exhibit high morphological heterogeneity, therefore a large number of cells must be analyzed to obtain statistically reliable data (Wright et al., 2020). From personal experience, manual measurement of individual cardiomyocytes in bright-field images is time consuming and prone to investigator bias. The quality of cardiomyocytes in culture decreases over time and agonist intervention (Louch et al., 2011). The investigator is biased to subjectively include cells for analysis while others are excluded based on deteriorated morphology *e.g.* kinked or bloated appearance. Cell fixation and cytoskeleton or membrane labeling enables the acquisition of fluorescence images and the use of semi-automated image analysis using open source software like *ImageJ* or *CellProfiler*. Fixation and staining has several drawbacks: (i) Significant detachment of cardiomyocytes, which might dis-proportionally affect agonist treated or untreated control cells, (ii) in-homogeneous staining due to loss of antigen to agonist treatment and (iii) labor and cost intensive.

The use of a bright-field cell culture microscope for image acquisition of viable cardiomyocyte in cell-culture conditions eliminates any bias due to cell fixation and staining. The use of bright-field images for automated image analysis poses several challenges: Images taken from viable cells exhibit low contrast and heterogeneous color intensity levels which hinders the ability to specify a global set of threshold parameters that are required in cell segmentation methods, implemented in image analysis software like *CellProfiler* (Buggenthin et al., 2013).

The *Ilastik* pixel classification tool can be utilized to close this gap. The software uses a machine learning based random forest classifier which is trained by user annotations and provides probability map images that can be used for subsequent object identification and morphology measurements in high-throughput capable software like *CellProfiler* (Berg et al., 2019). The parameters used to filter viable rod shaped cardiomyocytes in *CellProfiler* were selected empirically. The processed output images were inspected visually for major miss-classifications and only a negligible number of cardiomyocytes were wrongfully included or excluded from measurement. The upper cell-surface area limit prevented the inclusion of cell-conglomerates that met the shape descriptive parameters. A thorough analysis of false positive and negative frequency as well as a blindfolded comparative manual measurement were not carried out.

Hypertrophic growth of cardiomyocytes in histology sections is commonly assessed by measuring the cross-sectional area in WGA stained mid-ventricular heart sections. Cardiomyocytes exhibit an elliptical shape and are sectioned from various angles in histology slides, which impacts the cross-sectional area measurements. If an area was chosen in which cardiomyocytes were sectioned not perpendicular to the long axis, the cross-sectional area

increases significantly (Pertl et al., 2013). There are numerous protocols to measure WGA cross-sectional area in histology slides. Some researchers state that only enucleated cardiomyocyte are measured, others put emphasis on the mere round appearance but more often than not, no criteria for cell measurements are stated (Jahng et al., 2015; Ryu et al., 2016; Chen et al., 2015). Due to the lack of objective rules, the manual measurement of cross-sectional areas is susceptible to biased analysis and also time consuming (Winters et al., 2020). These limitations can be overcome by the implementation of automated cell morphology measurements. Lau, Xu, et al. (2018) recently published a *CellProfiler* pipeline for the measurement of WGA stained muscle fibers which, however, lacked inclusion/exclusion parameters and highlighted the challenge of weak cell boundary staining that lead to erroneous fusion of individual cardiomyocytes. To account for the latter, the *Ilastik* pixel classifier algorithm was trained on a subset of training images and used for cell boundary enhancement prior to image segmentation. Subsequent object identification in *CellProfiler* was significantly improved. The combination of shape descriptive parameters eccentricity, form factor and solidity enabled filtering and objective measurement of round shaped cardiomyocytes. The error of including the cross-sectional area of obliquely sectioned elliptical cardiomyocytes in cross-sectional area measurements was therefore reduced.

A possible bias in the automated analysis of cross-sectional area is the lower Feret´s Diameter limit of $\geqslant 35$ pixel units which was set to exclude small non-cardiomyocyte cells. This could dis-proportionally affect the hypertrophied sections in which cardiomyocytes could have been raised above the threshold in a proportion of cells and skewed the mean cross-sectional area towards lower values. As shown in the histogram on Figure 3.11c the percentage of cardiomyocytes smaller than 1000 a.u. did not differ in between the ISO exposed and control groups which indicates that this effect did not have a significant impact.

4.2 Functionality of DNG and effect on β-AR signaling *in vitro* and *in vivo*

The inhibitory properties of DNG on Gα_s signaling were determined by Berlot (2002) in HEK cells. Here, the cAMP formation from the Gα_s coupled luteinizing hormone receptor to 20 ng/ml human chorionic gonadotropin was inhibited by 97 % and reached approximately 80 % inhibition of response to saturating agonist concentrations. In this thesis, the inhibitory effect of DNG on the β-AR signaling cascade was assessed by live cell cAMP-FRET microscopy and by analysing the phosphorylation state of PLN at the Ser^{16} residue which is a key substrate of PKA.

Gene transfer of DNG along with cytosolic FRET-cAMP biosensor Epac1-camps (Nikolaev, Bünemann, Hein, et al., 2004) was pursued by transient transfection in HEK cells and adenoviral transduction in ARVCM (Bastug-Özel et al., 2019). Cytosolic live cell cAMP reaction to non-selective β-AR stimulation by 100 nM ISO was measured and related to maximum FRET induced by broad inhibition PDEs and ACs activation. DNG was functional in HEK-cells and ARVCM. The cAMP reaction to β-AR stimulation (100 nM ISO) was significantly inhibited by approximately 80 % in HEK-cells and ARVCM as shown in Figures 3.1 and 3.3. Similar to the saturating agonist concentrations that achieved maximum Gα_s DNG inhibition of 80 % (Berlot, 2002), the maximum FRET response to the high concentration of 100 nM ISO was inhibited by 80 % in HEK-cells and ARVCM. A concentration of 1 nM ISO is sufficient to induce significant *in vitro* cardiomyocyte contraction responses and doses above 10 nM induce maximum initial cAMP formation (De Arcangelis et al., 2008). Therefore, it can be assumed that ISO at 100 nM is above the maximum saturating agonist concentration where Gα_s inhibition is at maximum 80 % and a higher inhibition is expected at lower agonist concentrations which would also resemble a more physiologic environment.

Subsequent analysis of the PLN-Ser^{16} phosphorylation state to 100 nM ISO revealed an approximately 64 % inhibition by DNG in ARVCM as shown in Figure 3.4. The 15-20 % discrepancy in the degree of signaling cascade inhibition observed in the cAMP-FRET measurements and PLN-Ser^{16} phosphorylation state can be discussed in light of the phosphorylation dynamics of PLN. In a study by Jones et al. (2012), PLN-Ser^{16} phosphorylation in cardiomyocytes exposed to increasing doses of ISO reached a maximum plateau at 10 nM and did not increase any further. The 100 nM ISO used exceeded this concentration suggesting that the PLN-Ser^{16} phosphorylation was saturated in the control cardiomyocytes but further increased in DNG expressing cardiomyocytes which seemingly decreased the inhibitory competence of DNG.

The DNG was shown to be functional in inhibiting short-term β-AR Gα_s downstream signaling. Sustained inhibition was subsequently tested by analyzing the hypertrophic growth in Adv-DNG transducted ARVCM to chronic β_1-AR stimulation (Schäfer et al., 2000). Here, the development of hypertrophy was inhibited to sustained β_1-AR stimulation throughout increasing ISO concentrations as shown in Figure 3.5.

In murine models, over-expression of the major elements of the β-AR – Gα_s – PKA axis that result in enhanced signaling, are detrimental over time highlighting the adverse effects of chronic elevated sympathetic stimulation (Engelhardt, Hein, et al., 1999; Port et al., 1998; Iwase, Bishop, et al., 1996; Iwase, Uechi, et al., 1997; Antos et al., 2001). Murine models with reduced or diminished sympathetic drive to the heart by knock-out of the β_1-AR, β_1- and β_2-AR as well as the major AC type 5 exhibit normal cardiac phenotype and resting heart

function (Rohrer et al., 1996; Kiriazis et al., 2008; Okumura et al., 2003).

Cardiomyocyte specific blockage of $G\alpha_s$ signaling was first achieved *in vivo* by the α-MHC directed transgenic expression of a dominant negative $G\alpha_s$ mutant ($G\alpha_s$-DN) by Streit et al. (2016). Over-expression of $G\alpha_s$-DN results in normal cardiac phenotype and resting heart function with reduced heart rate in conscious mice. The cardiac function in AAV-DNG injected mice in this thesis was assessed by echocardiography under isoflurane anaesthiesia three weeks post AAV injection. AAV-DNG led to a mild increase in the LVPWd with otherwise comparable cardiac performance to AAV-mCherry injected control animals as shown in Table 3.1.

$G\alpha_s$-DN-mice are protected from pathological hypertrophy to chronic 14 d ISO infusion with significantly reduced increase in HW/TL ratio and cardiomyocyte cross-sectional area (Streit et al., 2016). Likewise, AAV-DNG injected mice are partially protected against one-week ISO induced pathological hypertrophy. Post-ISO echocardiography revealed reduced development of hypertrophy as the gain in IVSd and LVPWd to ISO exposure was significantly averted while the LVIDd was not affected, which would indicate malignant LV-dilation (Fig. 3.8). A DNG effect was not observed in structural changes to the heart as the increase in HW/TL ratio as well as the cardiomyocyte cross-sectional area did not differ significantly in the ISO exposed AAV-DNG in comparison to the AAV-mCherry injected animals. The cardiomyocyte size distribution changed towards higher values with both ISO treated groups affected in a nearly identical way (Fig. 3.11).

The expression of pathological hypertrophy associated *fetal* genes were differently affected: The expression of the scaffolding protein *Fhl1* was impacted by ISO exposure to a similar degree in both AAV-DNG and AAV-mCherry animals. *Fhl1* is a sarcomeric biomechanical stress sensor that scaffolds mitogen-activated protein kinase (MAPK) components to tintin spring elements and positively mediates stress signaling involving the $G\alpha_q$ signaling cascade in pressure overload induced heart failure and promotes pathological hypertrophy in mice (Liang et al., 2018; Sheikh et al., 2008). The cardiac expression of *Fhl1* is also increased in mice upon chronic β-AR stimulation (Lau, Cao, et al., 2018). *Fhl2* on the other hand exhibits protective properties as it represses calcineurin and NFAT signaling and is significantly up-regulated in mouse hearts exposed to chronic one-week β-AR stimulation (Hojayev et al., 2012). Contrary to the literature, *Fhl2* expression did not change significantly to one week chronic β-AR stimulation. In AAV-DNG injected mice, the down-regulation of *Myh7* was partially inhibited while the up-regulation of *Nappa* was significantly inhibited in comparison to AAV-mCherry injected mice. The down-regulation of *Myh7* observed in cardiac tissue from AAV-mCherry mice was not accompanied by the up-regulation of *Myh6*,

which is observed in C57BL/6J following chronic s.c. 14 d 30 µg/g/day ISO infusion (Yoshida et al., 2014). Not affected by ISO was the expression of *Nppb*.

Besides the induction of pathological hypertrophy, the over-expression of the above mentioned β-AR signaling cascade enhancing elements, as well as chronic ISO infusion, induces cardiac remodeling and fibrosis (Engelhardt, Hein, et al., 1999; Port et al., 1998; Iwase, Bishop, et al., 1996; Iwase, Uechi, et al., 1997; Antos et al., 2001; Grimm et al., 2015). Conversely, less collagen deposition is observed in response to chronic ISO infusion in Gα_s-DN-mice (Streit et al., 2016). One-week chronic ISO infusion did not cause collagen deposition in this thesis. The expression of pro-fibrotic genes *Postn* (Oka et al., 2007), *Col1a1* and *Col3a1* (Gao et al., 2017), although, were found to be significantly up-regulated in AAV-mCherry and significantly less elevated in AAV-DNG injected animals as shown in Figure 3.13.

The development of cardiac hypertrophy and remodeling is significantly reduced in Gα_s-DN mice to chronic ISO infusion (Streit et al., 2016). While DNG successfully averted *in vitro* hypertrophy to chronic β_1-AR stimulation, the *in vivo* effect led to discrepancies in the results: The effects observed in echocardiography and transcription of *fetal* and pro-fibrotic genes to chronic ISO infusion were marked by a limited inhibition of global cardiac and cardiomyocyte hypertorphy. The discrepancy can be discussed with the following aspects: (i) impaired AAV transduction efficiency, (ii) challenges in DNG – Gα_s expression and (iii) differences in DNG and Gα_s-DN.

AAV transduction efficiency

The *in vivo* transduction efficiency of ssAAV9-TnT-mCherry-2A-DNG (AAV-DNG) was initially determined by analyzing the expression of the reporter protein mCherry in a preliminary experiment. Two mice (C57BL/6N) at the age of 5 weeks were injected with AAV-DNG and transgene expression analyzed 6 weeks post AAV-injection by IHC and western blot analysis. Here, strong mCherry expression was detected in approximately 90 % of cardiomyocytes in IHC stained cross-sectional heart sections and additionally detected by western blot analysis in gross left ventricular tissue as shown in Figure 3.7a. At 4 weeks post AAV injection mCherry was evident in both the AAV-mCherry as well as the AAV-DNG injected control animals. Approximately 50 % of cardiomyocytes exhibited strong mCherry expression in cross-sectional heart sections as shown in Figure 3.9. The transduction efficiency was significantly lower than anticipated at 4 weeks post AAV injection, assuming reliable representation of transduction efficiency in IHC anti-mCherry stained histology slides. A

transduction efficiency of 99.5 % 10-12 days after tail-vein injection of 10^{12} vg of single-stranded AAV9-lacZ in C57BL/6 mice has been reported by Inagaki et al. (2006). Whereas a comparably low transduction efficiency was observed previously two weeks after the systemic retro-orbital injection of 10^{11} vg/g body weight of AAV9-TnT-GFP in 4-6 week-old mice by Bezzerides et al. (2019). Taking the reduced ssAAV efficiency into account (McCarty et al., 2003) it is likely that the transgene and DNG expression was not fully present at three weeks post AAV injection. It is hypothesised that DNG inhibition of hypertrophy development was limited in the initial phase of ISO stimulation while inhibition was increasingly effective to the late phase of ISO, sufficient to affect cardiac function in echocardiography and the transcription of pathological hypertrophy associated *fetal* and pro-fibrotic genes.

Furthermore, Streit et al. (2016) achieved α-MHC directed Gα_s-DN expression by generation of transgenic mice. In doing so, a more uniform expression is expected than trough gene transfer by the use of AAV. Here, a non-uniform expression of DNG could lead to varying transduction efficiencies to the conductive tissue. It is hypothesized that differences in the expression of dominant negative Gα_s mutants in the conductive tissue could differently affect heart rate at rest and to chronic ISO infusion. Here, the differentially affected heart rate may cause different degrees of tachycardia induced cardiomyopathy. Gα_s-DN mice exhibited significant heart rate reduction by approximately 10 % in conscious three months old animals (Streit et al., 2016). Heart rate measurements in conscious mice were not carried out in this thesis. Conclusions about resting heart rate during echocardiography cannot be drawn. The isoflurane anaesthesia used during echocardiography negatively impacts cardiac function with increasing doses (Pachon et al., 2015). The mean heart rate of approximately 380 bpm observed during echocardiography in both AAV-DNG and AAV-mCherry as shown in Table 3.1 and 3.2 is considered to be deep anaesthesia (Picard et al., 2014) in which case cardiac function is depressed and thus conclusions about resting heart rate are not possible. Contrary to the hypothesis of differently affected heart rate in ISO infused mice, the heart rate in Gα_s-DN as well as AAV-DNG injected mice, as shown in Table 3.2, exhibited unaltered increase in heart rate to ISO compared to the respective ISO exposed control animals (Streit et al., 2016).

In future *in vivo* studies the use of self-complementary AAV should be pursued. These AAV exhibit more rapid and more efficient transgene expression (Wang, Ma, et al., 2003) whereby here, the use of a reporter protein would not be possible due to the limited packaging capacity of scAAV.

DNG and Gα_s expression

Besides the above-discussed reduced transgene expression due to ssAAV inefficiency the expression of DNG itself can be discussed as a limiting factor. DNG is a mutated Gα_s subunit derived from rat *GNAS1* cDNA (Berlot, 2002). Other researchers have previously encountered challenges in the cardiac over-expression of Gα_s and similar challenges are expected with the expression of DNG.

The expression of DNG was initially analyzed by western blot in the preliminary AAV-DNG mice probing for Gα_s in gross left-ventricular tissue as shown in Figure 3.7. Both the short and the long isoform of Gα_s protein band were enhanced in western blot analysis. Also, a faint double band was detected above the long Gα_s isoform. The additional band most likely derived from DNG protein, which, in the original methodological study about DNG by Berlot (2002), appeared as a slightly larger band on western blot in direct comparison to endogenous Gα_s. The appearance of the DNG band in Gα_s western blot analysis was additionally observed in Adv-DNG transducted ARVCM as shown in Figure 3.2. Contrary to the faint DNG western blot band observed in the preliminary experiment the presence of DNG protein was not detected by Gα_s western blot 4 weeks post AAV injection as shown in Figure 3.10. The protein expression analysis was complemented by *DNG* specific rt-qPCR. Here, DNG mRNA was detected in gross left ventricular tissue. The rt-qPCR *DNG* primers are not mRNA specific and detection of genomic *DNG* cannot be excluded. The risk of DNA contamination was although significantly reduced by DNAse treatment of RNA samples.

Apart from reduced DNG expression at 4 weeks post AAV injection due to the discussed ssAAV limitations, the cardiomyocyte directed over-expression of Gα has posed a challenge to other research groups. It became evident that the artificial expression of Gα_s in cardiomyocytes is highly inefficient. In transgenic mice, Gα_s over-expression under the control of the cardiomyocyte specific α-MHC promoter resulted in a 38-fold increase in mRNA expression in the heart, while Gα_s protein increased merely by a factor of 2.8 (Gaudin et al., 1995). Similar inefficiency was observed in neonatal rat cardiomyocytes. Here, adenoviral overexpression of Gα_s was inefficient resulting in a mRNA to protein ratio of 40:1 (Hippe, Lüdde, et al., 2013). In gross left ventricular tissue in AAV-DNG mice, *DNG* was approximately 5 % of *GNAS* expression. Although here only limited conclusions can be drawn. Gα_s expression is not limited to cardiomyocytes but also present in vascular smooth muscle cells, endothelial cells and fibroblasts (Wang, Gareri, et al., 2018), all present in preparations from gross left-ventricular tissue. Effectively relating *DNG* to *GNAS* expression, would require to analyze mRNA extracted exclusively from cardiomyocytes.

While DNG expression was not detectable in western blot at 4 weeks post AAV-DNG injection, changes in the expression of $G\alpha_s$ were observed. In the initial preliminary AAV test the total $G\alpha_s$ expression was enhanced as shown in Figure 3.7. At 4 weeks post AAV-DNG injection although the total $G\alpha_s$ expression was statistically significantly reduced as shown in figure 3.10. The reduced $G\alpha_s$ protein expression in AAV-DNG injected vehicle treated mice at 4 weeks post AAV injection can be discussed by a direct impact of DNG on $G\alpha_s$ expression: The AC regulating $G\alpha$ proteins $G\alpha_s$ and $G\alpha_i$ in cardiomyocytes co-localize in membrane pools, such as caveolae and lipid rafts, in which their membrane attachment is dependent on binding to a distinct pool of $G\beta\gamma$ protein and subsequent formation of heterotrimetric G-protein whereas unbound $G\alpha_{s/i}$ is rapidly degraded (Hippe, Lüdde, et al., 2013; Hippe, Wolf, et al., 2009). In neonatal rat cardiomyocytes artificial increase of either $G\alpha_s$ or $G\alpha_i$ results in decreased membrane content of the respective unaffected protein, in a $G\beta\gamma$ dependent post-transcriptional mechanism (Hippe, Lüdde, et al., 2013). DNG, which has an increased affinity to $G\beta\gamma$ (Berlot, 2002), could initially sequester $G\beta\gamma$ from endogenous $G\alpha_s$ which would subsequently be subjected to increased protein degradation (Levis and Bourne, 1992; Naviglio et al., 2004). Here, the significant reduction in protein $G\alpha_s$ could be observed while theoretically DNG protein contents have not risen to western blot detectable concentrations in gross left ventricular protein lysates. The increased $G\alpha_s$ expression observed in the preliminary AAV-test might suggest a compensatory up-regulation of $G\alpha_s$ protein in response to DNG expression over time.

In response to ISO exposure $G\alpha_s$ protein was significantly reduced in both the AAV-mCherry and AAV-DNG injected mice. This was most likely due to a post-translational mechanism as the *GNAS* mRNA expression was not affected as shown in Figure 3.10. A major mechanism of post-translational control of protein content is the rate of protein degradation. Activated $G\alpha_s$ is subjected to enhanced protein degradation (Chang and Bourne, 1989; Levis and Bourne, 1992). β-AR stimulation induces $G\alpha_s$ polyubiquitination and subsequent protein degradaton by the proteasome system (Naviglio et al., 2004). Here, sustained β-AR stimulation has profound effects on the proteasome system: Chronic β-AR stimulation in the mouse significantly reduces the amount of polyubiquitinated protein in hypertrophied left ventricular tissue and is proposed to be a negative feedback-loop to catecholaminergic overstimulation as it impacts key elements of the β-AR signaling cascade (Drews et al., 2010). To which extend DNG is subjected to proteasomal degradation is unknown. To my knowledge, there are no studies regarding protein degradation of DNG.

In the hypothetical case of ubiquitous inhibitory DNG effect in cardiomyocytes, an at-

tenuated down-regulation of Gα_s in response to ISO is anticipated. Due to the expression of Gα_s in cells other than cardiomyocytes (Wang, Gareri, et al., 2018), the attenuated Gα_s down-regulation to ISO, as an indirect effect of DNG inhibition, could have been obscured in protein preparations from gross left ventricular tissue. The Nanostring® gene expression analysis, however, revealed an attenuated down-regulation of PPI-1 (*App1r1a*) in AAV-DNG ISO exposed animals as shown in Figure 3.12. PPI-1 is a distal amplifier of the β-AR signaling cascade, highly expressed in heart muscle and down-regulated in response to chronic β-AR stimulation in rodents and also observed in human heart failure (Weber et al., 2016; Wittköpper, Dobrev, et al., 2011). This effect was, although, insignificant in the ISO to ISO comparison. Nevertheless, the trend in attenuated *App1r1a* down-regulation to β-AR stimulation is an indicator of partial inhibitory effect of DNG.

Differences in DNG and Gα_s-DN

The two dominant negative Gα_s mutants DNG and Gα_s-DN (Streit et al., 2016) share some analogies but differ in one functional mutation site which could lead to varying effects on downstream signaling. The DNG construct used in this thesis is comprised of three sets of functional mutations: $\alpha 3\beta 5$, G226A and A366S. The inhibitory effect is exerted by increased receptor affinity, decreased receptor-mediated activation, impaired activation of adenylyl cyclase, increased affinity for $\beta\gamma$ and decreased affinity for GDP (Berlot, 2002). The Gα_s-DN construct used by Streit et al. (2016) was constructed by Iiri et al. (1999). It also contained the G226A and A366S mutations while instead of the mutations in the $\alpha 3\beta 5$ loop it contained the E268A mutation. According to Iiri et al. (1999) the Gα_s-DN mutant impacts Gα_s signaling by exhibiting a reduced ability for binding GDP (A366S) and further impair GTP binding and GTP dependent conformational change (G226A and E268A) which would stabilize a receptor bound empty state of $\alpha_e\beta\gamma$ and thus also sequester $\beta\gamma$. The Gα_s-DN mutant exhibited weaker inhibitory capacity than DNG to Gα_s signaling. Furthermore, Gα_s-DN is severely susceptible to thermal denaturation at 37 °C (Berlot, 2002; Iiri et al., 1999). While Gα_s-DN did not inhibit signaling from receptors that solely couple to Gα_i or Gα_q the inhibitory properties to receptors that couple to multiple Gα proteins is unknown. Here, DNG has the ability to block signaling from GPCR that can couple to multiple G-proteins besides α_s (Berlot, 2002).

Besides β-AR in cardiomyocytes, there are multiple GPCRs that couple to Gα_s but also other Gα subunits which might be subjected to the inhibitory effect of DNG: The histamine receptor H_2 is Gα_s coupled and affects cardiac function and apoptosis, the relaxin family peptide receptors RXFP1 is G$\alpha_{s/i}$ coupled and exerts anti-apoptotic properties, the Gα_s coupled vasopressin receptor V_2 modulates β-AR function and metabolism and the sphingosine

1-phosphate receptor S1PR2 is coupled to $G\alpha_{s/q}$ and $G\alpha_{12/13}$ affecting myofilament contractility and heart development (Wang, Gareri, et al., 2018). Differences in the inhibition of other GPCR signaling cascades by DNG in comparison to $G\alpha_s$-DN could also account for the observed discrepancy on the development of hypertrophy and fibrosis in this study.

Although the broad inhibitory effect of DNG poses a challenge in the interpretation of acquired results, it can also be applied in future studies to investigate the involvement of the above listed GPCR in cardiac disease and further to study the sub-cellular compartmentalization of G-proteins and their diverging cellular effects (Berlot, 2002).

4.3 Limitations

There are several limitations in this thesis. The conclusions about the *in vitro* effect of DNG on chronic β_1-AR stimulation induced hypertrophy were based solely on morphological changes. For definite conclusions the results could be substantiated by measuring additional independent markers of ARVCM *in vitro* hypertrophy, like [3 H] isoleucine incorporation or the RNA / protein to DNA ratio (Vidal et al., 2012; Schirmer et al., 2018). The unknown *in vivo* expression of DNG at 3 weeks post AAV-injection, prior to ISO infusion, limits the potential for interpretation. The expression analysis were based on direct detection of either DNG mRNA and protein in addition to the expression analysis of the reporter protein mCherry. *In vivo* DNG expression could additionally be investigated by measuring DNG effect on downstream β-AR signaling. For example, cAMP content or phosphorylation of β-AR downstream signaling cascade components in cardiomyocytes isolated from AAV-DNG injected mice, with and without *ex vivo* ISO stimulation, could reveal functional inhibitory properties and thus the presence of functional DNG (Myagmar et al., 2017). Also not addressed was the DNG effect on cardiomyocyte contractile function. Here, contractile measurements of Adv-DNG transducted ARVCM or left ventricular catheterization in AAV-DNG injected mice could reveal altered basal cardiomyocyte or cardiac function and altered response to acute β-AR stimulation.

Several factors limit the interpretation of the obtained results, for which more in-depth considerations and experiments were beyond the scope of this thesis. For example, little is known about the sub-cellular localization, trafficking and effect of DNG on other G-proteins. Novel mechanisms are identified that regulate $G\alpha_s$ and facilitate switch from $G\alpha_s$ to $G\alpha_i$ signaling and may be involved in the development of heart failure (Abu-Taha et al., 2017). Also unknown is the effect of DNG on other GPCR and downstream signaling. Including

signaling beyond the *classical* pathway, such as G-protein independent β-arrestin and GRK signaling, for which cardioprotective effects are assumed (Noma et al., 2007; Tilley, 2011). Further studies are needed to address these unknowns.

4.4 DNG as a genetic β-AR blocker in human heart failure

In humans, the clinical use of β-AR blockers is a cornerstone in HF therapy and significantly reduces morbidity and mortality in patients with HFrEF (Schinzari et al., 1999; Tepper, 1999; Packer, Coats, et al., 2001; Packer, Fowler, et al., 2002; Ponikowski, Voors, et al., 2016). Critical to the possible use of DNG in the treatment of HF is the ongoing debate about the mechanism behind the beneficial effect of β-AR blocker treatment. It is still unclear if the beneficial effect is due to blockage or re-sensitization of the β-AR signaling cascade (Lucia et al., 2018). If the re-sensitization of the β-AR system is the main beneficial effect, blockage of $G\alpha_s$ signaling by DNG would be undesirable. The clinical administration of β-AR blocker in patients with HF is initiated at a low-dose with gradual increase over the course of several weeks to a maximum tolerated dose (Ponikowski, Voors, et al., 2016; Gottlieb et al., 2002). Abrupt introduction of β-AR blocker therapy carries the risk of causing acute cardiac decompensation due to the negative inotropic effect (Gottlieb et al., 2002). In this thesis, one AAV-DNG injected and ISO exposed animal exhibited signs of severe cardiac decompensation as shown in Figure 3.14. The acute onset of β-AR blockage can be discussed as a possible explanation for acute cardiac decompensation.

Besides to effect of chronic sympathetic stimulation on cardiac remodeling and hypertrophy, excess catecholaminergic stimulation is also a major trigger of severe ventricular arrhythmias (Muller et al., 1997; Nam et al., 2005). Furthermore, elevated heart rate is an independent modifiable risk factor for disease outcome in patients with coronary artery disease and heart failure. Lowering heart rate has been proven effective and is currently a treatment option for patients with HF (Böhm et al., 2010; Fox et al., 2009; Ponikowski, Voors, et al., 2016). Both heart rate and arrhythmogenesis are influenced by $G\alpha_s$ dependent signaling (Wieneke et al., 2016). Targeting $G\alpha_s$ signaling in the conductive tissue reduces heart rate and heart rate response to ISO stimulation (Sebastian et al., 2013; Lugenbiel et al., 2012). Conductive tissue directed AAV-DNG gene therapy carries the potential of beneficial heart rate reduction in HF patients. In a future attempt to transfer the use of AAV-DNG to the human, engineered heart tissue would facilitate a suitable model to investigate the effect of DNG on β-AR signaling and cardiac function (Neuber et al., 2014).

5 Conclusion and outlook

The blockage of Gα_s coupled β-AR signaling in cardiomyocytes poses a promising gene therapeutic approach for cardiac disease. Chronic stimulation of the β-AR signaling cascade significantly contributes to cardiac deterioration in HF patients. One of the major adverse effects is the induction of pathological hypertrophy. Expression of a DNG by adenoviral gene transfer in ARVCM was achieved and successfully inhibited cAMP formation and downstream PLN phosphorylation to β-AR stimulation. Consistently, the development of *in vitro* hypertrophy to chronic β_1-AR stimulation was averted. The *in vivo* expression was achieved by ssAAV mediated gene transfer. Here, mice with cardiomyocyte specific expression of DNG exhibited regular cardiac function at three weeks post AAV injection as assessed by echocardiography. In response to one week chronic β-AR stimulation the development of cardiac hypertrophy was averted in echocardiography as well as the induction of pathological hypertrophy associated expression of *fetal* and pro-fibrotic genes. The development of cardiac hypertrophy in HW/TL ratio and cardiomyocyte cross-sectional area although was not inhibited. The discrepancy can be in part explained by delayed expression of DNG either due to ssAAV transduction limitations or limited expression of DNG, resulting in partial protective effect of DNG. Further research is needed to uncover the expression and degradation of DNG in cardiomyocytes as well as the effect of DNG on other GPCR signaling pathways to enable definite conclusions about the *in vivo* effect of DNG. Gene therapeutic AAV mediated myocardial and conductive tissue directed delivery of a dominant negative Gα_s mutant poses a promising, effective and versatile tool to investigate the effect of Gα_s inhibition for *in vivo* experiments. Here, AAV-DNG can be utilized to investigate the involvement of Gα_s in disease progression in heart failure models, as well as in the context of inherited cardiac diseases. Furthermore, a future application as gene therapy for cardiac disease can be envisioned and therefore warrants further investigations.

Bibliography

Abrams, Jonathan (Dec. 1985). "Vasodilator Therapy for Chronic Congestive Heart Failure". In: *JAMA: The Journal of the American Medical Association* 254.21, p. 3070.

Abu-Taha, Issam H. et al. (2017). "Nucleoside Diphosphate Kinase-C Suppresses cAMP Formation in Human Heart Failure". In: *Circulation* 135.9, pp. 881–897.

Agüero, Jaime et al. (2012). "Myocardial G protein receptor-coupled kinase expression correlates with functional parameters and clinical severity in advanced heart failure". In: *Journal of Cardiac Failure* 18.1, pp. 53–61.

Ambrosy, Andrew P. et al. (2014). "The global health and economic burden of hospitalizations for heart failure: Lessons learned from hospitalized heart failure registries". In: *Journal of the American College of Cardiology* 63.12, pp. 1123–1133.

Antos, Christopher L., Norbert Frey, Steven O. Marx, Steven Reiken, Marta Gaburjakova, James A. Richardson, Andrew R. Marks, and Eric N. Olson (2001). "Dilated cardiomyopathy and sudden death resulting from constitutive activation of protein kinase A". In: *Circulation Research* 89.11, pp. 997–1004.

Aoi, Wataru and Myron H. Weinberger (1976). "The Effect of Age and Norepinephrine on Renin Release by Rat Kidney Slices In Vitro". In: *Proceedings of the Society for Experimental Biology and Medicine* 151.1, pp. 47–52.

El-Armouche, Ali, Torsten Pamminger, Diana Ditz, Oliver Zolk, and Thomas Eschenhagen (2004). "Decreased protein and phosphorylation level of the protein phosphatase inhibitor-1 in failing human hearts". In: *Cardiovascular Research* 61.1, pp. 87–93.

El-Armouche, Ali, Katrin Wittköpper, et al. (2008). "Phosphatase inhibitor-1-deficient mice are protected from catecholamine-induced arrhythmias and myocardial hypertrophy". In: *Cardiovascular Research* 80.3, pp. 396–406.

Asai, Kuniya et al. (1999). "β-Adrenergic receptor blockade arrests myocyte damage and preserves cardiac function in the transgenic G(sα) mouse". In: *Journal of Clinical Investigation* 104.5, pp. 551–558.

Bastug-Özel, Zeynep et al. (Mar. 2019). "Heart failure leads to altered β2-adrenoceptor/cyclic adenosine monophosphate dynamics in the sarcolemmal phospholemman/Na,K ATPase microdomain". In: *Cardiovascular Research* 115.3, pp. 546–555.

Bekheirnia, Mir Reza and Robert William Schrier (2006). "Pathophysiology of water and sodium retention: Edematous states with normal kidney function". In: *Current Opinion in Pharmacology* 6.2, pp. 202–207.

Beller, George and Barry Zaret (2000). "Clinical Cardiology: New Frontiers". In: *Circulation* 101, pp. 1465–1478.

Berg, Stuart et al. (2019). "Ilastik: Interactive Machine Learning for (Bio)Image Analysis". In: *Nature Methods* 16.12, pp. 1226–1232.

Berlot, Catherine H. (2002). "A highly effective dominant negative ??s construct containing mutations that affect distinct functions inhibits multiple Gs-coupled receptor signaling pathways". In: *Journal of Biological Chemistry* 277.23, pp. 21080–21085.

Bezzerides, Vassilios J. et al. (2019). "Gene Therapy for Catecholaminergic Polymorphic Ventricular Tachycardia by Inhibition of Ca2+/Calmodulin-Dependent Kinase II". In: *Circulation* 140.5, pp. 405–419.

Böhm, Michael, Karl Swedberg, Michel Komajda, Jeffrey S. Borer, Ian Ford, Ariane Dubost-Brama, Guy Lerebours, and Luigi Tavazzi (2010). "Heart rate as a risk factor in chronic heart failure (SHIFT): The association between heart rate and outcomes in a randomised placebo-controlled trial". In: *The Lancet* 376.9744, pp. 886–894.

Bristow, Michael R, Robert Ginsburg, Victor Umans, et al. (1986). "We used radioligand binding techniques and measurement of /3-agonist-mediated positive inotropic responses in isolated cardiac tissue to examine /3-adrenergic-receptor subpopulations in nonfailing and failing human left and right ventricular myocardium. I". In: *Circulation research* 59.3, pp. 297–309.

Bristow, Michael R., Robert Ginsburg, Wayne Minobe, Roger S. Cubicciotti, W. Scott Sageman, Keith Lurie, Margaret E. Billingham, Donald C. Harrison, and Edward B. Stinson (July 1982). "Decreased Catecholamine Sensitivity and β-Adrenergic-Receptor Density in Failing Human Hearts". In: *New England Journal of Medicine* 307.4, pp. 205–211.

Buggenthin, Felix, Carsten Marr, Michael Schwarzfischer, Philipp S. Hoppe, Oliver Hilsenbeck, Timm Schroeder, and Fabian J. Theis (2013). "An automatic method for robust and fast cell detection in bright field images from high-throughput microscopy". In: *BMC Bioinformatics* 14.1.

Bui, Anh L., Tamara B. Horwich, and Gregg C. Fonarow (2011). "Epidemiology and risk profile of heart failure". In: *Nature Reviews Cardiology* 8.1, pp. 30–41.

Burchfield, Jana S., Min Xie, and Joseph A. Hill (2013). "Pathological ventricular remodeling: Mechanisms: Part 1 of 2". In: *Circulation* 128.4, pp. 388–400.

Bustin, Stephen and Jim Huggett (2017). "qPCR primer design revisited". In: *Biomolecular Detection and Quantification* 14.November, pp. 19–28.

Chang, F. H. and H. R. Bourne (1989). "Cholera toxin induces cAMP-independent degradation of G(s)". In: *Journal of Biological Chemistry*.

Chang, Sunny C., Shuxun Ren, Christoph D. Rau, and Jessica J. Wang (2018). "Isoproterenol-Induced Heart Failure Mouse Model Using Osmotic Pump Implantation". In: *High Blood Pressure & Cardiovascular Prevention*. Vol. 26. 5, pp. 207–220.

Chen, Youfang, Jianfeng Du, Yu Tina Zhao, Ling Zhang, Guorong Lv, Shougang Zhuang, Gangjian Qin, and Ting C. Zhao (2015). "Histone deacetylase (HDAC) inhibition improves myocardial function and prevents cardiac remodeling in diabetic mice". In: *Cardiovascular Diabetology* 14.1, pp. 1–13.

Chesley, Alan, Martha S. Lundberg, Toshinobu Asai, Rui Ping Xiao, Seiji Ohtani, Edward G. Lakatta, and Michael T. Crow (2000). "The β2-adrenergic receptor delivers an antiapoptotic signal to cardiac myocytes through G(i)-dependent coupling to phosphatidylinositol 3'-kinase". In: *Circulation Research* 87.12, pp. 1172–1179.

Chidsey, Charles A., Eugene Braunwald, and Andrew G. Morrow (Sept. 1965). "Catecholamine excretion and cardiac stores of norepinephrine in congestive heart failure". In: *The American Journal of Medicine* 39.3, pp. 442–451.

Chioncel, Ovidiu et al. (2017). "Epidemiology and one-year outcomes in patients with chronic heart failure and preserved, mid-range and reduced ejection fraction: an analysis of the ESC Heart Failure Long-Term Registry". In: *European Journal of Heart Failure* 19.12, pp. 1574–1585.

Christ, Michael, Stefan Störk, Marcus Dörr, Hans J. Heppner, Christian Müller, Rolf Wachter, and Uwe Riemer (2016). "Heart failure epidemiology 2000–2013: insights from the German Federal Health Monitoring System". In: *European Journal of Heart Failure* 18.8, pp. 1009–1018.

Cohn, Jay N., Donald G. Archibald, et al. (June 1986). "Effect of Vasodilator Therapy on Mortality in Chronic Congestive Heart Failure". In: *New England Journal of Medicine* 314.24, pp. 1547–1552.

Cohn, Jay N., T. Barry Levine, Maria Teresa Olivari, Victoria Garberg, Dennis Lura, Gary S. Francis, Ada B. Simon, and Thomas Rector (Sept. 1984). "Plasma Norepinephrine as a Guide to Prognosis in Patients with Chronic Congestive Heart Failure". In: *New England Journal of Medicine* 311.13, pp. 819–823.

Colucci, W. S., A. R. Denniss, G. F. Leatherman, R. J. Quigg, P. L. Ludmer, J. D. Marsh, and D. F. Gauthier (1988). "Intracoronary infusion of dobutamine to patients with and without severe congestive heart failure. Dose-response relationships, correlation with circulating catecholamines, and effect of phosphodiesterase inhibition". In: *Journal of Clinical Investigation* 81.4.

Communal, Catherine, Krishna Singh, Douglas B. Sawyer, and Wilson S. Colucci (1999). "Opposing effects of β1- and β2-adrenergic receptors on cardiac myocyte apoptosis: Role of a pertussis toxin-sensitive G protein". In: *Circulation* 100.22, pp. 2210–2212.

De Arcangelis, Vania, Dagoberto Soto, and Yang Xiang (Nov. 2008). "Phosphodiesterase 4 and Phosphatase 2A Differentially Regulate cAMP/Protein Kinase A Signaling for Cardiac Myocyte Contraction under Stimulation of β 1 Adrenergic Receptor". In: *Molecular Pharmacology* 74.5, pp. 1453–1462.

Doehner, Wolfram et al. (2018). "Heart and brain interaction in patients with heart failure: overview and proposal for a taxonomy. A position paper from the Study Group on Heart and Brain Interaction of the Heart Failure Association". In: *European Journal of Heart Failure* 20.2, pp. 199–215.

Drews, Oliver, Osamu Tsukamoto, David Liem, John Streicher, Yibin Wang, and Peipei Ping (2010). "Differential Regulation of Proteasome Function in Isoproterenol-Induced Cardiac Hypertrophy". In: *Circulation Research* 107.9, pp. 1094–1101.

Dunlay, Shannon M., Véronique L. Roger, and Margaret M. Redfield (2017). "Epidemiology of heart failure with preserved ejection fraction". In: *Nature Reviews Cardiology* 14.10, pp. 591–602.

Engelhardt, S, L Hein, F Wiesmann, and M J Lohse (1999). "Progressive hypertrophy and heart failure in beta1-adrenergic receptor transgenic mice." In: *Proceedings of the National Academy of Sciences of the United States of America* 96.12, pp. 7059–64.

Engelhardt, Stefan, Michael Böhm, Erland Erdmann, and Martin J. Lohse (1996). "Analysis of beta-adrenergic receptor mRNA levels in human ventricular biopsy specimens by quantitative polymerase chain reactions: Progressive reduction of beta1-adrenergic receptor mRNA in heart failure". In: *Journal of the American College of Cardiology* 27.1, pp. 146–154.

Ergatoudes, Constantinos, Maria Schaufelberger, Bert Andersson, Aldina Pivodic, and Michael Fu (Sept. 2019). "Non-cardiac comorbidities and mortality in patients with heart failure with reduced vs. preserved ejection fraction: a study using the Swedish Heart Failure Registry". In: *Clinical Research in Cardiology* 108.9, pp. 1025–1033.

Eschenhagen, Thomas (2008). "β-adrenergic signaling in heart failure—adapt or die". In: *Nature medicine* 14.5, pp. 485–487.

Eschenhagen, Thomas et al. (1990). "Increased messenger RNA level of the inhibitory G protein α subunit Giα-2 in human end-stage heart failure". In: *Circulation Research* 70.4, pp. 688–696.

Ferrari, F K, T Samulski, T Shenk, and R J Samulski (1996). "Second-strand synthesis is a rate-limiting step for efficient transduction by recombinant adeno-associated virus vectors." In: *Journal of virology* 70.5, pp. 3227–3234.

Floras, John S. (2009). "Sympathetic Nervous System Activation in Human Heart Failure. Clinical Implications of an Updated Model". In: *Journal of the American College of Cardiology* 54.5, pp. 375–385.

Floras, John S. and Piotr Ponikowski (2015). "The sympathetic/parasympathetic imbalance in heart failure with reduced ejection fraction". In: *European Heart Journal* 36.30, pp. 1974–1982.

Fox, Kim, Ian Ford, Ph Gabriel Steg, Michal Tendera, Michele Robertson, and Roberto Ferrari (2009). "Relationship between ivabradine treatment and cardiovascular outcomes in patients with stable coronary artery disease and left ventricular systolic dysfunction with limiting angina: A subgroup analysis of the randomized, controlled BEAUTIFUL trial". In: *European Heart Journal* 30.19, pp. 2337–2345.

Franciosa, J. A., R. A. Jordan, M. M. Wilen, and C. L. Leddy (July 1984). "Minoxidil in patients with chronic left heart failure: contrasting hemodynamic and clinical effects in a controlled trial." In: *Circulation* 70.1, pp. 63–68.

Froese, Alexander and Viacheslav O. Nikolaev (2015). "Imaging alterations of cardiomyocyte cAMP microdomains in disease". In: *Frontiers in Pharmacology* 6.Aug, pp. 3–7.

Gao, Mei Hua, N. Chin Lai, Dimosthenis Giamouridis, Young Chul Kim, Tracy Guo, and H. Kirk Hammond (2017). "Cardiac-directed expression of a catalytically inactive adenylyl cyclase 6 protects the heart from sustained β-adrenergic stimulation". In: *PLoS ONE* 12.8, pp. 1–17.

Gaudin, C., Y. Ishikawa, D. C. Wight, V. Mahdavi, B. Nadal-Ginard, T. E. Wagner, D. E. Vatner, and C. J. Homcy (1995). "Overexpression of G(sα) protein in the hearts of transgenic mice". In: *Journal of Clinical Investigation* 95.4, pp. 1676–1683.

Gevaert, Andreas B., Jente R.A. Boen, Vincent F. Segers, and Emeline M. Van Craenenbroeck (2019). "Heart failure with preserved ejection fraction: A review of cardiac and noncardiac pathophysiology". In: *Frontiers in Physiology* 10.MAY.

Gottlieb, Stephen S., Michael L. Fisher, John Kjekshus, Prakash Deedwania, Lars Gullestad, Jiri Vitovec, and John Wikstrand (2002). "Tolerability of β-blocker initiation and titration in the Metoprolol CR/XL Randomized Intervention Trial in Congestive Heart Failure (MERIT-HF)". In: *Circulation* 105.10, pp. 1182–1188.

Grimm, Michael et al. (2015). "CaMKIIδ mediates β-adrenergic effects on RyR2 phosphorylation and SR Ca2+ leak and the pathophysiological response to chronic β-adrenergic stimulation". In: *Journal of Molecular and Cellular Cardiology* 85, pp. 282–291.

Grossman, W., D. Jones, and L. P. McLaurin (1975). "Wall stress and patterns of hypertrophy in the human left ventricle". In: *Journal of Clinical Investigation* 56.1, pp. 56–64.

Haider, Agha W., Martin G. Larson, Emelia J. Benjamin, and Daniel Levy (1998). "Increased left ventricular mass and hypertrophy are associated with increased risk for sudden death". In: *Journal of the American College of Cardiology* 32.5, pp. 1454–1459.

Hartupee, Justin and Douglas L. Mann (2016). "Neurohormonal activation in heart failure with reduced ejection fraction". In: *Nature Reviews Cardiology* 14.1, pp. 30–38.

Heckmann, M. B. et al. (2016). "AAV9-mediated gene transfer of desmin ameliorates cardiomyopathy in desmin-deficient mice". In: *Gene Therapy* 23.8-9, pp. 673–679.

Heidenreich, Paul A et al. (2013). "Forecasting the Impact of Heart Failure in the United States: A Policy Statement From the American Heart Association Council on Cardiovascular Radiology and Intervention, Council on Clinical Cardiology, Council on Epidemiology and Prevention, and Stroke C". In: *Circ Heart Fail* 6.3, pp. 606–619.

Herring, Neil, Manish Kalla, and David J. Paterson (2019). "The autonomic nervous system and cardiac arrhythmias: current concepts and emerging therapies". In: *Nature Reviews Cardiology* Mi.

Hill, Joseph A. and Eric N. Olson (2008). "Cardiac Plasticity". In: *New England Journal of Medicine* 358.13, pp. 1370–1380.

Hippe, Hans Joerg, Nadine M. Wolf, et al. (2009). "The interaction of nucleoside diphosphate kinase B with G$\beta\gamma$ dimers controls heterotrimeric G protein function". In: *Proceedings of the National Academy of Sciences of the United States of America* 106.38, pp. 16269–16274.

Hippe, Hans Jörg, Mark Lüdde, et al. (2013). "Competition for G$\beta\gamma$ dimers mediates a specific cross-talk between stimulatory and inhibitory G protein α subunits of the adenylyl cyclase in cardiomyocytes". In: *Naunyn-Schmiedeberg's Archives of Pharmacology* 386.6, pp. 459–469.

Ho, Jennifer E., Asya Lyass, Douglas S. Lee, Ramachandran S. Vasan, William B. Kannel, Martin G. Larson, and Daniel Levy (Mar. 2013). "Predictors of New-Onset Heart Failure". In: *Circulation: Heart Failure* 6.2, pp. 279–286.

Hojayev, B., B. A. Rothermel, T. G. Gillette, and J. A. Hill (2012). "FHL2 Binds Calcineurin and Represses Pathological Cardiac Growth". In: *Molecular and Cellular Biology* 32.19, pp. 4025–4034.

Holstiege, Jakob, Manas K Akmatov, Annika Steffen, and Jörg Bätzing (2018). "Prävalenz der Herzinsuffizienz-bundesweite Trends, regionale Variationen und häufige Komorbiditäten". In: *Zentralinstitut für die kassenärztliche Versorgung in Deutschland (Zi)* Versorgung.1, pp. 1–22.

Iiri, Taroh, Sean M. Bell, Thomas J. Baranski, Toshiro Fujita, and Henry R. Bourne (1999). "A Gsα mutant designed to inhibit receptor signaling through Gs". In: *Proceedings of the National Academy of Sciences of the United States of America* 96.2, pp. 499–504.

Inagaki, Katsuya, Sally Fuess, Theresa A. Storm, Gregory A. Gibson, Charles F. Mctiernan, Mark A. Kay, and Hiroyuki Nakai (July 2006). "Robust systemic transduction with AAV9 vectors in mice: efficient global cardiac gene transfer superior to that of AAV8". In: *Molecular Therapy* 14.1, pp. 45–53.

Iwase, Mitsunori, Sanford P Bishop, et al. (Apr. 1996). "Adverse effects of chronic endogenous sympathetic drive induced by cardiac GS alpha overexpression." In: *Circulation research* 78.4, pp. 517–24.

Iwase, Mitsunori, Masami Uechi, et al. (1997). "Cardiomyopathy induced by cardiac G(S)α overexpression". In: *American Journal of Physiology - Heart and Circulatory Physiology* 272.1 41-1.

Jahng, James Won Suk, Subat Turdi, Vera Kovacevic, Keith Dadson, Ren Ke Li, and Gary Sweeney (2015). "Pressure overload-induced cardiac dysfunction in aged male adiponectin knockout mice is associated with autophagy deficiency". In: *Endocrinology* 156.7, pp. 2667–2677.

Janes, Ronald D., J. Christopher Brandys, David A. Hopkins, David E. Johnstone, David A. Murphy, and J. Andrew Armour (1986). "Anatomy of human extrinsic cardiac nerves and ganglia". In: *The American Journal of Cardiology* 57.4, pp. 299–309.

Jones, Brian W., Sylvain Brunet, Merle L. Gilbert, C. Blake Nichols, Thomas Su, Ruth E. Westenbroek, John D. Scott, William A. Catterall, and G. Stanley McKnight (2012). "Cardiomyocytes from AKAP7 knockout mice respond normally to adrenergic stimulation". In: *Proceedings of the National Academy of Sciences of the United States of America* 109.42, pp. 17099–17104.

Kemp, Clinton D. and John V. Conte (2012). "The pathophysiology of heart failure". In: *Cardiovascular Pathology* 21.5, pp. 365–371.

Khera, Rohan et al. (2017). "Contemporary epidemiology of heart failure in fee-for-service medicare beneficiaries across healthcare settings". In: *Circulation: Heart Failure* 10.11.

Kieserman, Jake M., Valerie D. Myers, Praveen Dubey, Joseph Y. Cheung, and Arthur M. Feldman (2019). "Current Landscape of Heart Failure Gene Therapy". In: *Journal of the American Heart Association* 8.10, pp. 1–14.

Kim, Tae Kyung and James H. Eberwine (2010). "Mammalian cell transfection: The present and the future". In: *Analytical and Bioanalytical Chemistry* 397.8, pp. 3173–3178.

Kiriazis, H. et al. (2008). "Knockout of β 1- and β 2-adrenoceptors attenuates pressure overload-induced cardiac hypertrophy and fibrosis". In: *British Journal of Pharmacology* 153.4, pp. 684–692.

Kirshenbaum, Lorrie A., W. Robb MacLellan, Wojciech Mazur, Brent A. French, and Michael D. Schneider (1993). "Highly efficient gene transfer into adult ventricular myocytes by recombinant adenovirus". In: *Journal of Clinical Investigation* 92.1, pp. 381–387.

LAEMMLI, U. K. (Aug. 1970). "Cleavage of Structural Proteins during the Assembly of the Head of Bacteriophage T4". In: *Nature* 227.5259, pp. 680–685.

Larstorp, Anne Cecilie K., Peter M. Okin, Richard B. Devereux, Michael H. Olsen, Hans Ibsen, Björn Dahlöf, Sverre E. Kjeldsen, and Kristian Wachtell (2012). "Regression of ECG-LVH is associated with lower risk of new-onset heart failure and mortality in patients with isolated systolic hypertension; The life study". In: *American Journal of Hypertension* 25.10, pp. 1101–1109.

Lau, Edward, Quan Cao, et al. (2018). "Integrated omics dissection of proteome dynamics during cardiac remodeling". In: *Nature Communications* 9.1.

Lau, Yeh Siang, Li Xu, Yandi Gao, and Renzhi Han (2018). "Automated muscle histopathology analysis using CellProfiler". In: *Skeletal Muscle* 8.1, pp. 1–9.

Lavoie, Catherine et al. (2002). "β1/β2-adrenergic receptor heterodimerization regulates β2-adrenergic receptor internalization and ERK signaling efficacy". In: *Journal of Biological Chemistry* 277.38, pp. 35402–35410.

Leineweber, Kirsten, Thekla Wangemann, Christine Giessler, Heike Bruck, Stefan Dhein, Martin Kostelka, Friedrich Wilhelm Mohr, Rolf Edgar Silber, and Otto Erich Brodde (2002). "Age-dependent changes of cardiac neuronal noradrenaline reuptake transporter (uptake1) in the human heart". In: *Journal of the American College of Cardiology* 40.8, pp. 1459–1465.

Levis, Mark J. and Henry R. Bourne (1992). "Activation of the α subunit of Gs in intact cells alters its abundance, rate of degradation, and membrane avidity". In: *Journal of Cell Biology* 119.5, pp. 1297–1307.

Levy, Daniel (1991). "Clinical significance of left ventricular hypertrophy: Insights from the Framingham study". In: *Journal of Cardiovascular Pharmacology*. Vol. 17. SUPPL. 2, S1–S6.

Li, Xiaofeng et al. (2020). "Calcineurin Aβ-Specific Anchoring Confers Isoform-Specific Compartmentation and Function in Pathological Cardiac Myocyte Hypertrophy". In: *Circulation*, pp. 948–962.

Liang, Yan, William H. Bradford, Jing Zhang, and Farah Sheikh (2018). "Four and a half LIM domain protein signaling and cardiomyopathy". In: *Biophysical Reviews* 10.4, pp. 1073–1085.

Livak, Kenneth J. and Thomas D. Schmittgen (2001). "Analysis of relative gene expression data using real-time quantitative PCR and the 2-$\Delta\Delta$CT method". In: *Methods* 25.4, pp. 402–408.

Lohse, Martin J., Stefan Engelhardt, and Thomas Eschenhagen (Nov. 2003). "What Is the Role of β-Adrenergic Signaling in Heart Failure?" In: *Circulation Research* 93.10, pp. 896–906.

Louch, William E, Katherine A Sheehan, and Beata M Wolska (Sept. 2011). "Methods in cardiomyocyte isolation, culture, and gene transfer". In: *Journal of Molecular and Cellular Cardiology* 51.3, pp. 288–298.

Lowes, Brian D. et al. (1997). "Changes in gene expression in the intact human heart: Downregulation of α-myosin heavy chain in hypertrophied, failing ventricular myocardium". In: *Journal of Clinical Investigation* 100.9, pp. 2315–2324.

Lucia, Claudio de, Akito Eguchi, and Walter J. Koch (2018). "New insights in cardiac β-Adrenergic signaling during heart failure and aging". In: *Frontiers in Pharmacology* 9.AUG, pp. 1–14.

Lugenbiel, Patrick, Alexander Bauer, Kamilla Kelemen, Patrick A. Schweizer, Rüdiger Becker, Hugo A. Katus, and Dierk Thomas (2012). " Biological Heart Rate Reduction Through Genetic Suppression of Gα s Protein in the Sinoatrial Node ". In: *Journal of the American Heart Association* 1.2, pp. 1–9.

Luke, Garry A., Pablo de Felipe, Alexander Lukashev, Susanna E. Kallioinen, Elizabeth A. Bruno, and Martin D. Ryan (2008). "Occurrence, function and evolutionary origins of '2A-like' sequences in virus genomes". In: *Journal of General Virology* 89.4, pp. 1036–1042.

MacLennan, David H. and Evangelia G. Kranias (2003). "Phospholamban: A crucial regulator of cardiac contractility". In: *Nature Reviews Molecular Cell Biology* 4.7, pp. 566–577.

Maggioni, Aldo P. et al. (2013). "EURObservational Research Programme: Regional differences and 1-year follow-up results of the Heart Failure Pilot Survey (ESC-HF Pilot)". In: *European Journal of Heart Failure* 15.7, pp. 808–817.

Mann, Douglas L., Robert L. Kent, Bruce Parsons, and G Cooper (Feb. 1992). "Adrenergic effects on the biology of the adult mammalian cardiocyte." In: *Circulation* 85.2, pp. 790–804.

Martini, Jeffrey S. et al. (Nov. 2008). "Correction for Martini et al., Uncovering G protein-coupled receptor kinase-5 as a histone deacetylase kinase in the nucleus of cardiomyocytes". In: *Proceedings of the National Academy of Sciences* 105.44, pp. 17206–17206.

Mathew, James et al. (2001). "Reduction of cardiovascular risk by regression of electrocardiographic markers of left ventricular hypertrophy by the angiotensin-converting enzyme inhibitor ramipril". In: *Circulation* 104.14, pp. 1615–1621.

Mazza, Alberto, Valérie Tikhonoff, Edoardo Casiglia, and Achille Cesare Pessina (2005). "Predictors of Congestive Heart Failure Mortality in Elderly People From the General Population". In: *International Heart Journal* 46.3, pp. 419–431.

McCarty, D. M., H. Fu, P. E. Monahan, C. E. Toulson, P. Naik, and R. J. Samulski (2003). "Adeno-associated virus terminal repeat (TR) mutant generates self-complementary vectors to overcome the rate-limiting step to transduction in vivo". In: *Gene Therapy* 10.26, pp. 2112–2118.

McQuin, Claire et al. (July 2018). "CellProfiler 3.0: Next-generation image processing for biology". In: *PLOS Biology* 16.7. Ed. by Tom Misteli, e2005970.

Métrich, Mélanie, Alexandre Lucas, Monique Gastineau, Jane Lise Samuel, Christophe Heymes, Eric Morel, and Frank Lezoualc'h (2008). "Epac mediates β-adrenergic receptor-induced cardiomyocyte hypertrophy". In: *Circulation Research* 102.8, pp. 959–965.

Movahedi, Kiavash, Robert Wiegmann, Karen De Vlaminck, Jo A. Van Ginderachter, and Viacheslav O. Nikolaev (July 2018). "RoMo: An efficient strategy for functional mosaic analysis via stochastic Cre recombination and gene targeting in the ROSA26 locus". In: *Biotechnology and Bioengineering* 115.7, pp. 1778–1792.

Muller, James E., Peter G. Kaufmann, Russell V. Luepker, Myron L. Weisfeldt, Prakash C. Deedwania, and James T. Willerson (1997). "Mechanisms precipitating acute cardiac events: Review and recommendations of an NHLBI workshop". In: *Circulation* 96.9, pp. 3233–3239.

Myagmar, Bat-Erdene et al. (Mar. 2017). "Adrenergic Receptors in Individual Ventricular Myocytes". In: *Circulation Research* 120.7, pp. 1103–1115.

Nakamura, Michinari and Junichi Sadoshima (July 2018). "Mechanisms of physiological and pathological cardiac hypertrophy". In: *Nature Reviews Cardiology* 15.7, pp. 387–407.

Nam, Gi Byoung, Alexander Burashnikov, and Charles Antzelevitch (2005). "Cellular mechanisms underlying the development of catecholaminergic ventricular tachycardia". In: *Circulation* 111.21, pp. 2727–2733.

Naviglio, Silvio, Mario Pagano, Maria Romano, Annunziata Sorrentino, Anna Fusco, Fausto Illiano, Emilio Chiosi, Annamaria Spina, and Gennaro Illiano (2004). "Adenylate cyclase regulation via proteasome-mediated modulation of Gαs levels". In: *Cellular Signalling* 16.11, pp. 1229–1237.

Neuber, Christiane et al. (2014). "Paradoxical effects on force generation after efficient β1-adrenoceptor knockdown in reconstituted heart tissue". In: *Journal of Pharmacology and Experimental Therapeutics* 349.4, pp. 39–46.

Neumann, Joachim, Wilhelm Schmitz, Hasso Scholz, L von Meyerinck, Volker Döring, and P Kalmar (Oct. 1988). "Increase in myocardial Gi-proteins in heart failure." In: *Lancet (London, England)* 2.8617, pp. 936–7.

Neumann, Till, Janine Biermann, Anja Neumann, Jürgen Wasem, Georg Ertl, Rainer Dietz, and Raimund Erbel (2009). "Herzinsuffizienz: Häufigster grund für krankenhausaufenthalte - Medizinische und ökonomische aspekte". In: *Deutsches Arzteblatt* 106.16, pp. 269–275.

Nikolaev, V. O., A. Moshkov, et al. (Mar. 2010). "2-Adrenergic Receptor Redistribution in Heart Failure Changes cAMP Compartmentation". In: *Science* 327.5973, pp. 1653–1657.

Nikolaev, Viacheslav, Moritz Bünemann, Lutz Hein, Annette Hannawacker, and Martin J. Lohse (Sept. 2004). "Novel Single Chain cAMP Sensors for Receptor-induced Signal Propagation". In: *Journal of Biological Chemistry* 279.36, pp. 37215–37218.

Nikolaev, Viacheslav O., Moritz Bünemann, Eva Schmitteckert, Martin J. Lohse, and Stefan Engelhardt (2006). "Cyclic AMP imaging in adult cardiac myocytes reveals far-reaching β1-adrenergic but locally confined β2-adrenergic receptor-mediated signaling". In: *Circulation Research* 99.10, pp. 1084–1091.

Noma, Takahisa et al. (2007). "β-Arrestin-mediated β1-adrenergic receptor transactivation of the EGFR confers cardioprotection". In: *Journal of Clinical Investigation* 117.9, pp. 2445–2448.

Oka, Toru et al. (2007). "Genetic manipulation of periostin expression reveals a role in cardiac hypertrophy and ventricular remodeling". In: *Circulation Research* 101.3, pp. 313–321.

Okumura, Satoshi et al. (2003). "Disruption of type 5 adenylyl cyclase gene preserves cardiac function against pressure overload". In: *Proceedings of the National Academy of Sciences of the United States of America* 100.17, pp. 9986–9990.

Pachon, Ronald E., Bruce A. Scharf, Dorothy E. Vatner, and Stephen F. Vatner (2015). "Best anesthetics for assessing left ventricular systolic function by echocardiography in mice". In: *American Journal of Physiology - Heart and Circulatory Physiology* 308.12, H1525–H1529.

Packer, Milton (1992). "The neurohormonal hypothesis: A theory to explain the mechanism of disease progression in heart failure". In: *Journal of the American College of Cardiology* 20.1, pp. 248–254.

Packer, Milton, Joseph R. Carver, et al. (Nov. 1991). "Effect of Oral Milrinone on Mortality in Severe Chronic Heart Failure". In: *New England Journal of Medicine* 325.21, pp. 1468–1475.

Packer, Milton, Andrew J.S. Coats, et al. (May 2001). "Effect of Carvedilol on Survival in Severe Chronic Heart Failure". In: *New England Journal of Medicine* 344.22, pp. 1651–1658.

Packer, Milton, Michael B. Fowler, et al. (2002). "Effect of carvedilol on the morbidity of patients with severe chronic heart failure: Results of the carvedilol prospective randomized cumulative survival (COPERNICUS) study". In: *Circulation* 106.17, pp. 2194–2199.

Paulus, Walter J. and Carsten Tschöpe (2013). "A novel paradigm for heart failure with preserved ejection fraction: Comorbidities drive myocardial dysfunction and remodeling through

coronary microvascular endothelial inflammation". In: *Journal of the American College of Cardiology* 62.4, pp. 263–271.

Pertl, Cordula, Markus Eblenkamp, Anja Pertl, Stefan Pfeifer, Erich Wintermantel, Hanns Lochmüller, Maggie C. Walter, Sabine Krause, and Christian Thirion (2013). "A new web-based method for automated analysis of muscle histology." In: *BMC musculoskeletal disorders* 14.

Peter, Angela K, Maureen A Bjerke, and Leslie A Leinwand (2016). "Biology of the cardiac myocyte in heart disease." In: *Molecular biology of the cell* 27.14, pp. 2149–60.

Picard, Fabien, Francois Depret, Sergio Zanotti-Cavazzoni, and Steven Hollenberg (2014). "Effect of anesthesia level on murine cardiac function". In: *F1000Research* 3.May, p. 165.

Ponchel, Frederique et al. (2003). "Real-time PCR based on SYBR-Green I fluorescence: An alternative to the TaqMan assay for a relative quantification of gene rearrangements, gene amplifications and micro gene deletions". In: *BMC Biotechnology* 3, pp. 1–13.

Ponikowski, Piotr, Stefan D. Anker, et al. (2014). "Heart failure: preventing disease and death worldwide". In: *ESC Heart Failure* 1.1, pp. 4–25.

Ponikowski, Piotr, Adriaan A. Voors, et al. (2016). "2016 ESC Guidelines for the diagnosis and treatment of acute and chronic heart failure". In: *European Heart Journal* 37.27, pp. 2129–2200.

Port, J.D., H.D. Weinberger, J.D. Bisognano, O.A. Knudson, T.J. Bohlmeyer, A. Pende, and M.R. Bristow (1998). "Echocardiographic and histopathological characterization of young and old transgenic mice over-expressing the human β1-adrenergic receptor". In: *Journal of the American College of Cardiology* 31, p. 177.

Puhl, Sarah Lena, Kate L. Weeks, Antonella Ranieri, and Metin Avkiran (2016). "Assessing structural and functional responses of murine hearts to acute and sustained β-adrenergic stimulation in vivo". In: *Journal of Pharmacological and Toxicological Methods* 79, pp. 60–71.

Rau, Christoph D., Jessica Wang, Rozeta Avetisyan, Milagros C. Romay, Lisa Martin, Shuxun Ren, Yibin Wang, and Aldons J. Lusis (Feb. 2015). "Mapping Genetic Contributions to Cardiac Pathology Induced by Beta-Adrenergic Stimulation in Mice". In: *Circulation: Cardiovascular Genetics* 8.1, pp. 40–49.

Reece-Hoyes, John S. and Albertha J.M. Walhout (Jan. 2018). "Gateway Recombinational Cloning". In: *Cold Spring Harbor Protocols* 2018.1, pdb.top094912.

Rockman, Howard A., Walter J. Koch, and Robert J. Lefkowitz (2002). "Seven-transmembrane-spanning receptors and heart function." In: *Nature* 415.6868, pp. 206–212.

Roger, Véronique L. (Aug. 2013). "Epidemiology of Heart Failure". In: *Circulation Research* 113.6, pp. 646–659.

Rohrer, Daniel K., Kavin H. Desai, Jeffrey R. Jasper, Mary E. Stevens, Donald P. Regula, Gregfory S. Barsh, Daniel Berstein, and Brian K. Kobilka (1996). "Targeted disruption of the mouse β1-adrenergic receptor gene: Developmental and cardiovascular effects". In: *Proceedings of the National Academy of Sciences of the United States of America* 93.14, pp. 7375–7380.

Ryu, Yuhee, Li Jin, Hae Jin Kee, Zhe Hao Piao, Jae Yeong Cho, Gwi Ran Kim, Sin Young Choi, Ming Quan Lin, and Myung Ho Jeong (2016). "Gallic acid prevents isoproterenol-induced cardiac hypertrophy and fibrosis through regulation of JNK2 signaling and Smad3 binding activity". In: *Scientific Reports* 6.September, pp. 1–14.

Samak, Mostafa et al. (2016). *Cardiac Hypertrophy: An Introduction to Molecular and Cellular Basis*.

Sato, Priscila Y., J. Kurt Chuprun, Mathew Schwartz, and Walter J. Koch (2015). "The evolving impact of g protein-coupled receptor kinases in cardiac health and disease". In: *Physiological Reviews* 95.2, pp. 377–404.

Saucerman, Jeffrey J., Philip M. Tan, Kyle S. Buchholz, Andrew D. McCulloch, and Jeffrey H. Omens (2019). "Mechanical regulation of gene expression in cardiac myocytes and fibroblasts". In: *Nature Reviews Cardiology* 16.6, pp. 361–378.

Schäfer, Matthias, Karen Frischkopf, Gerhild Taimor, Hans Michael Piper, and Klaus-Dieter Schlüter (2000). "Hypertrophic effect of selective β1-adrenoceptor stimulation on ventricular cardiomyocytes from adult rat". In: *American Journal of Physiology - Cell Physiology* 279.2, pp. C495–C503.

Schinzari, Francesca, Manfredi Tesauro, Augusto Veneziani, Nadia Mores, Nicola Di Daniele, and Carmine Cardillo (Jan. 1999). "The Cardiac Insufficiency Bisoprolol Study II (CIBIS-II): a randomised trial". In: *The Lancet* 353.9146, pp. 9–13.

Schirmer, Ilona et al. (Feb. 2018). "Soluble adenylyl cyclase: A novel player in cardiac hypertrophy induced by isoprenaline or pressure overload". In: *PLOS ONE* 13.2. Ed. by Harald HHW Schmidt, e0192322.

Schmieder, Round E., Franz H. Messerli, Dawn Sturgill, Guillermo E. Garavaglia, and Boris D. Nunez (1989). "Cardiac performance after reduction of myocardial hypertrophy". In: *The American Journal of Medicine* 87.1, pp. 22–27.

Sebastian, Sonia, Richard Ang, Joel Abramowitz, Lee S. Weinstein, Min Chen, Andreas Ludwig, Lutz Birnbaumer, and Andrew Tinker (Aug. 2013). "The in vivo regulation of heart rate in the murine sinoatrial node by stimulatory and inhibitory heterotrimeric G proteins." In: *American journal of physiology. Regulatory, integrative and comparative physiology* 305.4, pp. 435–42.

Sheikh, Farah et al. (2008). "An FHL1-containing complex within the cardiomyocyte sarcomere mediates hypertrophic biomechanical stress responses in mice". In: *Journal of Clinical Investigation* 118.12, pp. 3870–3880.

Simmonds, Steven J., Ilona Cuijpers, Stephane Heymans, and Elizabeth A. V. Jones (2020). "Cellular and Molecular Differences between HFpEF and HFrEF: A Step Ahead in an Improved Pathological Understanding". In: *Cells* 9.1, p. 242.

Stathopoulou, Konstantina, Friederike Cuello, Alexandra J. Candasamy, Elizabeth M. Kemp, Elisabeth Ehler, Robert S. Haworth, and Metin Avkiran (2014). "Four-and-a-half LIM domains proteins are novel regulators of the protein kinase D pathway in cardiac myocytes". In: *Biochemical Journal* 457.3, pp. 451–461.

Störk, Stefan, Renate Handrock, Josephine Jacob, Jochen Walker, Frederico Calado, Raquel Lahoz, Stephan Hupfer, and Sven Klebs (2017). "Epidemiology of heart failure in Germany: a retrospective database study". In: *Clinical Research in Cardiology* 106.11, pp. 913–922.

Streit, Marcus R. et al. (2016). "Cardiac effects of attenuating Gsα - Dependent signaling". In: *PLoS ONE* 11.1, pp. 1–19.

Sun, Yan, Hong Yu, Dong Zheng, Qi Cao, Ya Wang, David Harris, and Yiping Wang (2011). "Sudan black B reduces autofluorescence in murine renal tissue". In: *Archives of Pathology and Laboratory Medicine* 135.10, pp. 1335–1342.

Taylor, Clare J., José M. Ordóñez-Mena, Andrea K. Roalfe, Sarah Lay-Flurrie, Nicholas R. Jones, Tom Marshall, and F. D.Richard Hobbs (2019). "Trends in survival after a diagnosis of heart failure in the United Kingdom 2000-2017: population based cohort study". In: *The BMJ* 364, pp. 1–10.

Tepper, D. (June 1999). "Effect of metoprolol CR/XL in chronic heart failure: Metoprolol CR/XL Randomised Intervention Trial in-Congestive Heart Failure (MERIT-HF)". In: *The Lancet* 353.9169, pp. 2001–2007.

Thomas, Gail D. (2011). "Neural control of the circulation". In: *American Journal of Physiology - Advances in Physiology Education* 35.1, pp. 28–32.

Thornton, Brenda and Chhandak Basu (2011). "Real-time PCR (qPCR) primer design using free online software". In: *Biochemistry and Molecular Biology Education* 39.2, pp. 145–154.

Tilley, Douglas G. (July 2011). "G Protein–Dependent and G Protein–Independent Signaling Pathways and Their Impact on Cardiac Function". In: *Circulation Research* 109.2. Ed. by Howard Rockman, pp. 217–230.

Triposkiadis, Filippos, George Karayannis, Grigorios Giamouzis, John Skoularigis, George Louridas, and Javed Butler (2009). "The Sympathetic Nervous System in Heart Failure. Physiology, Pathophysiology, and Clinical Implications". In: *Journal of the American College of Cardiology* 54.19, pp. 1747–1762.

Tsao, Connie W., Asya Lyass, Danielle Enserro, Martin G. Larson, Jennifer E. Ho, Jorge R. Kizer, John S. Gottdiener, Bruce M. Psaty, and Ramachandran S. Vasan (2018). "Temporal Trends in the Incidence of and Mortality Associated With Heart Failure With Preserved and Reduced Ejection Fraction". In: *JACC: Heart Failure* 6.8, pp. 678–685.

Ungerer, M., M. Bohm, J. S. Elce, E. Erdmann, and M. J. Lohse (1993). "Altered expression of β-adrenergic receptor kinase and β1-adrenergic receptors in the failing human heart". In: *Circulation* 87.2, pp. 454–463.

Vedin, Ola et al. (June 2017). "Significance of Ischemic Heart Disease in Patients With Heart Failure and Preserved, Midrange, and Reduced Ejection Fraction: A Nationwide Cohort Study." In: *Circulation. Heart failure* 10.6, pp. 1–9.

Vidal, Marie, Thomas Wieland, Martin J. Lohse, and Kristina Lorenz (Nov. 2012). "β-Adrenergic receptor stimulation causes cardiac hypertrophy via a G$\beta\gamma$/Erk-dependent pathway". In: *Cardiovascular Research* 96.2, pp. 255–264.

Volpe, Massimo, Marino Carnovali, and Vittoria Mastromarino (2016). "The natriuretic peptides system in the pathophysiology of heart failure: From molecular basis to treatment". In: *Clinical Science* 130.2, pp. 57–77.

Wang, Jessica Jen Chu, Christoph Rau, Rozeta Avetisyan, Shuxun Ren, Milagros C. Romay, Gabriel Stolin, Ke Wei Gong, Yibin Wang, and Aldons J. Lusis (2016). "Genetic Dissection of Cardiac Remodeling in an Isoproterenol-Induced Heart Failure Mouse Model". In: *PLoS Genetics* 12.7, pp. 1–30.

Wang, Jialu, Clarice Gareri, and Howard A. Rockman (2018). "G-protein-coupled receptors in heart disease". In: *Circulation Research* 123.6, pp. 716–735.

Wang, Z., H. I. Ma, J. Li, L. Sun, J. Zhang, and X. Xiao (2003). "Rapid and highly efficient transduction by double-stranded adeno-associated virus vectors in vitro and in vivo". In: *Gene Therapy* 10.26, pp. 2105–2111.

Webb, Ian G. et al. (2010). "Constitutive glycogen synthase kinase-3/activity protects against chronic-adrenergic remodelling of the heart". In: *Cardiovascular Research* 87.3, pp. 494–503.

Weber, Silvio, Stefanie Meyer-Roxlau, and Ali El-Armouche (2016). "Role of protein phosphatase inhibitor-1 in cardiac beta adrenergic pathway". In: *Journal of Molecular and Cellular Cardiology* 101, pp. 116–126.

Werfel, Stanislas et al. (2014). "Rapid and highly efficient inducible cardiac gene knockout in adult mice using AAV-mediated expression of Cre recombinase". In: *Cardiovascular Research* 104.1, pp. 15–23.

Wieneke, Heinrich et al. (2016). "Polymorphisms in the GNAS gene as predictors of ventricular tachyarrhythmias and sudden cardiac death: Results from the DISCOVERY Trial and

Oregon Sudden Unexpected Death Study". In: *Journal of the American Heart Association* 5.12.

Winters, J. et al. (2020). "JavaCyte, a novel open-source tool for automated quantification of key hallmarks of cardiac structural remodeling". In: *Scientific Reports* 10.1, pp. 1–15.

Wittköpper, Katrin, Dobromir Dobrev, Thomas Eschenhagen, and Ali El-Armouche (2011). "Phosphatase-1 inhibitor-1 in physiological and pathological β-adrenoceptor signalling". In: *Cardiovascular Research* 91.3, pp. 392–401.

Wittköpper, Katrin, Larissa Fabritz, et al. (2010). "Constitutively active phosphatase inhibitor-1 improves cardiac contractility in young mice but is deleterious after catecholaminergic stress and with aging". In: *Journal of Clinical Investigation* 120.2, pp. 617–626.

Woo, Anthony Yiu Ho and Rui-ping Xiao (2012). "β-Adrenergic receptor subtype signaling in heart: From bench to bedside". In: *Acta Pharmacologica Sinica* 33.3, pp. 335–341.

Wright, Peter T., Sharmane F. Tsui, Alice J. Francis, Kenneth T. MacLeod, and Steven B. Marston (2020). "Approaches to High-Throughput Analysis of Cardiomyocyte Contractility". In: *Frontiers in Physiology* 11.July, pp. 1–19.

Wu, Jianqing, Weihong Zhao, Li Zhong, Zongchao Han, Baozheng Li, Wenqin Ma, Kirsten A. Weigel-Kelley, Kenneth H. Warrington, and Arun Srivastava (2007). "Self-complementary recombinant adeno-associated viral vectors: Packaging capacity and the role of Rep proteins in vector purity". In: *Human Gene Therapy* 18.2, pp. 171–182.

Yan, Guijun et al. (2015). "Orphan Nuclear Receptor Nur77 Inhibits Cardiac Hypertrophic Response to Beta-Adrenergic Stimulation". In: *Molecular and Cellular Biology* 35.19, pp. 3312–3323.

Yoshida, Tadashi, Maho Yamashita, Chihiro Horimai, and Matsuhiko Hayashi (2014). "Kruppel-like factor 4 protein regulates isoproterenol-induced cardiac hypertrophy by modulating myocardin expression and activity". In: *Journal of Biological Chemistry* 289.38, pp. 26107–26118.

Yu, Shuhua, Dawen Yu, Eric Lee, Michael Eckhaus, Randy Lee, Zakia Corria, Domenico Accili, Heiner Westphal, and Lee S. Weinstein (1998). "Variable and tissue-specific hormone resistance in heterotrimeric Gs protein α-subunit (Gsα) knockout mice is due to tissue-specific imprinting of the Gsα gene". In: *Proceedings of the National Academy of Sciences of the United States of America* 95.15, pp. 8715–8720.

Zarrinkoub, Ramin, Björn Wettermark, Per Wändell, Märit Mejhert, Robert Szulkin, Gunnar Ljunggren, and Thomas Kahan (2013). "The epidemiology of heart failure, based on data for 2.1 million inhabitants in Sweden". In: *European Journal of Heart Failure* 15.9, pp. 995–1002.

Zhang, David Y. and Allen S. Anderson (2014). "The Sympathetic Nervous System and Heart Failure". In: *Cardiology Clinics* 32.1, pp. 33–45.

Zile, M.R, C.F Baicu, and W.H Gaasch (2004). "Diastolic heart failure-abnormalities in active relaxation and passive stiffness of the left ventricle". In: *ACC Current Journal Review* 13.6, p. 36.

Lebenslauf

— Der Lebenslauf wurde aus datenschutzrechtlichen Gründen entfernt —

Danksagung

An dieser Stelle danke ich herzlich Prof. Viacheslav Nikolaev. Insbesondere für die Gelegenheit, bei diesem spannenden Thema mit Freude mitwirken zu dürfen. Hierbei konnte ich stets auf eine ausgezeichnete Zusammenarbeit, Rückhalt und Supervision vertrauen.

Des Weiteren danke ich Prof. Lucie Carrier, Prof. Tanja Zeller und Prof. Ulrich Wenzel für die Betreuung im Rahmen des DZHK Graduiertenkollegs. Wobei Prof. Tanja Zeller als stellvertretende Betreuerin der Doktorarbeit ein besonderer Dank zukommt. Auch danke ich dem DZHK für die finanzielle Unterstützung während des Forschungsjahres.

Ein außergewöhnlicher Dank geht an alle Beteiligten der AG Nikolaev für die tatkräftige Unterstützung, das inspirierende und freundschaftliche Arbeitsklima sowie die allzeit offenen Ohren für Fragen und hilfreiche Ratschläge. In besonderer Form bedanke ich mich bei Karina Schlosser und Sophie Sprenger für die technische Unterstützung und Betreuung.

Nicht zuletzt danke ich Birgit Geertz und Kirstie De Jong für die Unterstützung bei den Tierexperimenten sowie Maksymilian Prondzynski für die inspirierende Einführung in das Feld des high-content imaging. Ferner danke ich sowohl Kristin Hartmann für die Aufarbeitung der Gewebeproben als auch Dr. Antonio Virgilio Failla und dem Team der UKE Microscopy Imaging Facility.

Ein besonderer Dank geht an den Kreis meiner Familie und Freunde. Hier hat mich insbesonder mein Cousin Leon durch seine Korrekturen und Anmerkungen motiviert, auch in herausfordernden Zeiten, mehr *Liebe* in diese Arbeit einfließen zu lassen.

Eidesstattliche Erklärung

Ich versichere ausdrücklich, dass ich die Arbeit selbständig und ohne fremde Hilfe verfasst, andere als die von mir angegebenen Quellen und Hilfsmittel nicht benutzt und die aus den benutzten Werken wörtlich oder inhaltlich entnommenen Stellen einzeln nach Ausgabe (Auflage und Jahr des Erscheinens), Band und Seite des benutzten Werkes kenntlich gemacht habe. Ferner versichere ich, dass ich die Dissertation bisher nicht einem Fachvertreter an einer anderen Hochschule zur Überprüfung vorgelegt oder mich anderweitig um Zulassung zur Promotion beworben habe. Ich erkläre mich einverstanden, dass meine Dissertation vom Dekanat der Medizinischen Fakultät mit einer gängigen Software zur Erkennung von Plagiaten überprüft werden kann.

Unterschrift: _____